Title
Inhomogeneous He II Reionization and its Implications for the Intergalactic Medium

Permalink
https://escholarship.org/uc/item/90k0k1fq

Author
Dixon, Keri L.

Publication Date
2012

Peer reviewed|Thesis/dissertation

UNIVERSITY OF CALIFORNIA

Los Angeles

Inhomogeneous He II Reionization and its Implications for the Intergalactic Medium

A dissertation submitted in partial satisfaction

of the requirements for the degree

Doctor of Philosophy in Physics

by

Keri L. Dixon

2012

Abstract of the Dissertation

Inhomogeneous He II Reionization and its Implications for the Intergalactic Medium

by

Keri L. Dixon

Doctor of Philosophy in Physics

University of California, Los Angeles, 2012

Professor Steven R. Furlanetto, Chair

Recent observations suggest that quasars fully ionize helium around redshift $z \sim 3$. Most directly, the optical depth derived from the He II Lyman-α (Lyα) forest fluctuates significantly above and near $z \sim 2.8$ and then evolves smoothly at lower redshifts. These fluctuations may be indicative of patchy He II reionization, which is expected (primarily) due to the rarity and brightness of quasars and the inhomogeneous intergalactic medium. This dissertation presents approximate methods for interpreting observations of this epoch and quantifying the magnitude of fluctuations.

From these opacity measurements, we compute, using a semi-analytic model, the evolution of the mean photoionization rate and attenuation length for helium over the redshift range $2.0 \lesssim z \lesssim 3.2$. The average effective optical depth indicates a sharp decrease in the photoionization rate and, provided the quasar emissivity evolves smoothly, in the effective attenuation length at $z \approx 2.8$. A simple model with reionization ending at $z \approx 2.7$ is most consistent with the data, although the constraints are weak thanks to sparse, uncertain data.

We further present a fast, semi-numeric procedure to approximate detailed

cosmological simulations. We produce the distribution of dark matter halos, ionization state of helium, and density field at $z = 3$ in broad agreement with recent simulations. Given our speed and flexibility, we investigate a range of source and active quasar prescriptions. We find order-of-magnitude fluctuations in the He II ionization rate in the post-reionization Universe. During reionization, the fluctuations are even stronger and develop a bimodal distribution, in contrast with semi-analytic models and the hydrogen equivalent. We also examine large-scale fluctuations in the He II Lyα forest transmission during and after He II reionization. Like previous studies, we show that the rarity of quasars and the inhomogeneous intergalactic medium induce order unity fluctuations in the mean optical depth after reionization, even when averaged over large segments ($\sim 10 - 100$ Mpc in length). During reionization, we find a broader distribution with an extended high-opacity tail. These conclusions are fairly insensitive underlying model assumptions, including quasar properties and the mean free path of photons. We compare to existing data along ~ 10 He II Lyα forest lines of sight spanning $z \approx 2 - 3.2$, demonstrating that the observed fluctuations are likely due to ongoing reionization.

The dissertation of Keri L. Dixon is approved.

Kevin D. McKeegan

Bradley M. Hansen

Matthew A. Malkan

Steven R. Furlanetto, Committee Chair

University of California, Los Angeles

2012

TABLE OF CONTENTS

LIST OF FIGURES

LIST OF TABLES

ACKNOWLEDGMENTS

Vita

2002 - 2004	Teaching Assistant Department of Physics University of Illinois at Urbana-Champaign
2004	B.S. (Physics) University of Illinois at Urbana-Champaign
2004 - 2005	Teaching Assistant Department of Physics and Astronomy Stony Brook University
2006	M.S. (Physics) Stony Brook University
2006 - 2008	Teaching Assistant Department of Physics and Astronomy University of California, Los Angeles
2008 - 2012	Graduate Student Researcher Department of Physics and Astronomy University of California, Los Angeles

Publications

Furlanetto, S. R. & Dixon, K. L., "Large-Scale Fluctuations in the He II Lyα

Forest and He II Reionization" 2010, *The Astrophysical Journal*, 714, 355

Dixon, K. L. & Furlanetto, S. R., "The Evolution of the Helium-Ionizing Back-

ground at z $\sim 2 - 3$" 2009, *The Astrophysical Journal*, 706, 970

CHAPTER 1

Introduction

In the standard history of the Universe, the varied and complex structures observed today developed from an extremely hot, dense, and homogeneous medium. After this initial state expanded and cooled, the gas became neutral and opaque to photons, leading to the cosmic "dark ages." As the (small) initial density perturbations evolved with denser regions gravitationally attracting nearby matter, bound structures began to form, eventually leading to the first stars and galaxies. These objects were the first sources capable of reionizing the neutral hydrogen and helium, the two dominant baryonic species. With this "first light" and the eventual reionization of hydrogen, the intergalactic medium (IGM) once again became transparent to photons, illuminating the rich cosmos seen today.

The study of the epoch of reionization (see Loeb & Barkana 2001 for a review) not only endeavors to explain a particularly tumultuous period in the history of the Universe, but also gives clues about the environment and properties of the ionizing sources. How and when did the first stars form? What were the sources of ionizing radiation, and how were they distributed? How clumpy was the IGM? Careful modeling of the reionization process, combined with observational data, should provide answers or hints to these (and more) questions.

According to Big Bang nucleosynthesis, the baryonic matter started out as mostly hydrogen, some helium, and a smattering of other light elements. Hydrogen was reionized first, around a redshift $z \sim 6 - 12$. Not only is the ionization

potential of hydrogen (13.6 eV) lower than helium, but hydrogen recombines $\gtrsim 5$ slower than fully ionized helium. The first stars and galaxies were, therefore, capable of ionizing hydrogen and singly ionizing helium. To fully ionize helium (with an ionization potential of 54.4 eV), an extremely energetic source was needed. Quasars, produced by gas accreting onto super-massive black holes at the centers of galaxies, fulfilled this need and could not form until later times when such massive objects were possible. As quasar activity increased, helium became completely ionized around $z \sim 3$. During these phase transitions, the IGM became mostly transparent to the relevant ionizing photons, allowing the metagalactic ionizing background to grow rapidly.

Aside from its fundamental importance as a landmark event in cosmic history, the full reionization of helium has several important consequences for the IGM. Since helium makes up $\sim 24\%$ of the baryonic matter by mass, its ionization state alters the mean free path of photons above its ionization potential. Additionally, reionizing helium should significantly increase the temperature of the IGM (e.g., Hui & Gnedin 1997; Furlanetto & Oh 2008b; McQuinn et al. 2009). This heating may also influence galaxy formation by increasing the pressure (and hence Jeans mass) of the gas, which, in turn, may affect the star formation histories of galaxies (Wyithe & Loeb 2007). Determining the timing and duration of this epoch is, therefore, important for understanding the evolution of the IGM and galaxies.

The study of helium reionization has some advantages over the hydrogen equivalent and may serve as an object lesson for our understanding of that earlier era. Unlike for the reionization of hydrogen, we have excellent data on the state of the IGM at $z \sim 3$. Furthermore, the main drivers of helium reionization (quasars) are much better understood than their counterparts that drive hydrogen reionization.

Given the rarity of the sources and the inhomogeneity of the IGM, the process of helium reionization is expected to be patchy (e.g., Furlanetto & Oh 2008a; McQuinn et al. 2009). This patchiness has important implications for the evolution of the IGM, meaning that different regions will experience different reionization histories and requiring careful modeling. Many measurements make assumptions about the UV-background radiation and the temperature-density relation the ignore the inhomogeneity and timing of He II reionization. Quantifying the expected spread in He II ionization states and the impact of this spread on observable quantities is crucial, which is the main goal of this thesis.

1.1 Observational Evidence for Helium Reionization

The strongest pieces of evidence for helium reionization occurring at $z \sim 3$ are measurements of the He II Lyα forest that have started to test this epoch. Chapter 2 explores the early data that exhibit a rapid decrease in the He II effective optical depth (τ_{eff})with cosmic time at $z \gtrsim 2.7$, which may be indicative of He II reionization, while Furlanetto & Dixon (2010) showed that the large fluctuations observed in τ_{eff} were most likely indicative of ongoing reionization at $z \sim 2.8$. Now, the Cosmic Origins Spectrograph (COS) on the *Hubble Space Telescope* is providing an even more powerful probe of the the IGM at $2.4 \lesssim z \lesssim 3.7$. The measured τ_{eff} along the explored sightlines varies significantly at $z > 2.7$ and generally increases rapidly at higher redshift (Shull et al. 2010; Worseck et al. 2011; Syphers et al. 2012). Four lines of sight also show significant variation in the He II Lyβ optical depth (Syphers et al. 2011). This set of observations – and our detailed knowledge of the source populations and IGM at $z \sim 3$ – make a detailed study of the He II reionization process very timely. Chapter 5 quantifies expected fluctuations in the He II opacity both during and post-reionization and

compares to this recent data.

Several indirect methods attempt to probe the impact of helium reionization on the the IGM. Becker et al. (2011) measure the temperature evolution of the IGM to be consistent with extended helium reionization ending around $z \sim 3$ (though see Lidz et al. 2010). Around the same time, the IGM temperature-density relation appears to become nearly isothermal, another indication of recent helium reionization (e.g., Calura et al. 2012; Garzilli et al. 2012; Rudie et al. 2012). These studies show no sudden increase in temperature but are consistent with additional heating after hydrogen reionization, likely attributable to helium reionization. However, the uncertainties remain quite large and not all studies agree.

The (average) metagalactic ionizing background should also harden as helium is reionized, because the IGM would become increasingly transparent to high-energy photons. Songaila (1998, 2005) found a break in the ratio of C IV to Si IV at $z \sim 3$, though the effect should be small (Bolton & Viel 2011). Modeling of the ionizing background from optically thin and optically thick metal line systems also shows a significant hardening at $z \sim 3$ (Vladilo et al. 2003; Agafonova et al. 2005, 2007), but other data of comparable quality show no evidence for rapid evolution (Kim et al. 2002; Aguirre et al. 2004).

Since quasars are rare, the ionizing background should exhibit significant fluctuations even after reionization is complete (Fardal et al. 1998; Bolton et al. 2006; Meiksin 2009; Furlanetto 2009a). He II Lyα forest measurements provide some direct evidence for this behavior (Furlanetto & Dixon 2010). Additional sources of fluctuations are likely – radiative transfer through the clumpy IGM (Maselli & Ferrara 2005; Tittley & Meiksin 2007) and the effects of collisional ionization (Muzahid et al. 2011). During reionization, fluctuations in the UV radiation back-

ground are even greater, because some regions receive strong ionizing radiation while others remain singly ionized with no local illumination. Chapter 4 provides a systematic study fluctuations in the helium-ionizing radiation background both during and after reionization.

1.2   Methods for Modeling Helium Reionization

During the past decade, the reionization of helium and its impact on the IGM has received increased theoretical attention through a variety of methods. Both large-scale structures (spanning ~ 1 Gpc comoving scales), given the rarity of quasars and their clustering properties, and the small scales of gas physics play a significant role in fully understanding this epoch, but accounting for both simultaneously is computationally challenging. Since this epoch is observationally constrained in a way that hydrogen reionization is not, a viable model conforms to these observations, such as the IGM density and temperature.

Several studies employ various combinations of analytic, semi-analytic, and Monte Carlo methods (e.g., Gleser et al. 2005; Furlanetto & Oh 2008a; Furlanetto 2009a) to approximate the morphology of ionized helium bubbles, heating of the IGM, helium-ionizing background, etc. None of these methods can comprehensively include all relevant physics, especially spatial information like source clustering. Many numerical simulations of this epoch focus on scales $\leq 100^3$ comoving Mpc^3 (Sokasian et al. 2002; Paschos et al. 2007; Meiksin & Tittley 2012). These simulations miss the large ionized bubbles expected during helium reionization and fail to include many sources. McQuinn et al. (2009, hereafter M09) present large (hundreds of Mpc) N-body simulations with cosmological radiative transfer as a post-processing step. Note that M09 consider two classes of quasar models and vary the timing of reionization independently.

One major modeling hurdle is the implementation of quasars. The aggregate, empirical properties of quasars are well constrained with the quasar luminosity function (QLF) measured over a range of redshifts and to low optical luminosities (see Hopkins et al. 2007). The spectral energy distribution is more uncertain and varies significantly from quasar to quasar (e.g., Telfer et al. 2002; Scott et al. 2004; Shull et al. 2012). Furthermore, the lifetime of quasars (e.g., Kirkman & Tytler 2008; Kelly et al. 2010; Furlanetto & Lidz 2011) and their relation to dark matter halos (e.g., Hopkins et al. 2006; Wyithe & Loeb 2007; Conroy & White 2012) are far from settled. The challenge is to satisfy the observed quantities while allowing for a range possibilities for the more uncertain aspects.

As a first step, we construct a semi-analytic model, outlined in Chapter 2, to infer the helium photoionization rate from the He II Lyα forest. We include the QLF, a fluctuating UV background, and an inhomogeneous IGM but no detailed spatial information. To complement this method and other previous studies, we present fast, semi-numeric methods that incorporate realistic source geometries and explore a large parameter space in Chapter 3. We adapt the established hydrogen reionization code DexM (Mesinger & Furlanetto 2007) to $z = 3$, as appropriate for helium. The code applies approximate but efficient methods to produce dark matter halo distributions. From these distributions, it generates ionization maps using analytic arguments. The advantages of this approach are speed, as compared to cosmological simulations, and reasonably accurate spatial information (like halo clustering and a detailed local density field), as compared to more analytic studies. We also investigate a large range of quasar properties. We then apply these methods to two potentially observable quantities mentioned above – the helium-ionizing background in Chapter 4 and the He II Lyα fluctuations in Chapter 5. In Chapter 6, we summarize and address future avenues for study.

1.3   Adopted Conventions

We assume a cold dark matter cosmology with $\Omega_m = 0.26, \Omega_\Lambda = 0.74, \Omega_b = 0.044, H_0 = h(100 \text{ km s}^{-1} \text{ Mpc}^{-1})$ (with $h = 0.74$), $n = 0.95$, and $\sigma_8 = 0.8$ in our calculations.

CHAPTER 2

The Evolution of the Helium-Ionizing Background at $z \sim 2$–3

Recent observations indicate that helium reionization occurs at $z \sim 3$. The strongest evidence comes from far-ultraviolet spectra of the He II Lyα forest along the lines of sight to bright quasars at $z \sim 3$. These observations of the He II Lyα transition ($\lambda_{\mathrm{rest}} = 304$ Å) are difficult, because bright quasars with sufficient far-UV flux and no intervening Lyman-limit systems are required. As of 2009, six such lines of sight have yielded opacity measurements: PKS 1935-692 (Tytler et al. 1995; Anderson et al. 1999), HS 1700+64 (Davidsen et al. 1996; Fechner et al. 2006), HE 2347-4342 (Reimers et al. 1997; Kriss et al. 2001; Smette et al. 2002; Shull et al. 2004; Zheng et al. 2004b), SDSS J2346-0016 (Zheng et al. 2004a, 2008), Q0302-003 (Jakobsen et al. 1994; Hogan et al. 1997; Heap et al. 2000; Jakobsen et al. 2003) and HS 1157-3143 (Reimers et al. 2005). The effective helium optical depth from these studies decreases rapidly at $z \approx 2.8$, then declines slowly to lower redshifts. The opacities at higher redshifts exhibit a patchy structure with alternating high and low absorption, which may indicate an inhomogeneous radiation background.

In this chapter, we focus on interpreting the He II Lyα forest and the significance of the jump in the opacity at $z \approx 2.8$. After averaging the effective optical depth over all sightlines, we calculate the expected photoionization rate

given some simple assumptions. In particular, we investigate the impact of a fluctuating radiation background, comparing it to the common uniform assumption. We interpret our results in terms of an evolving attenuation length for helium-ionizing photons R_0 as well as state-of-the-art models of inhomogeneous reionization.

We use a semi-analytic model, outlined in §2.1, to infer the helium photoionization rate from the He II Lyα forest. The helium opacity measurements in the redshift range $2.0 \lesssim z \lesssim 3.2$, which serve as the foundation for our calculations, are compiled from the literature in §2.2. First, we assume a post-reionization universe over the entire redshift span. In this regime, we find the photoionization rate and attenuation length in §2.3, given the average measured opacity. Motivated by these results, we examine some fiducial reionization histories in §2.4. We conclude in §2.5.

2.1 Semi-Analytic Model

The helium Lyα forest observed in the spectra of quasars originates from singly ionized helium gas in the IGM. Quantitative measurement of this absorption is typically quoted as the mean transmitted flux ratio $\langle F \rangle$, defined as the mean of the ratio of observed and intrinsic fluxes, or the related effective optical depth

$$\tau_{\rm eff} \equiv -\ln\langle F \rangle. \tag{2.1}$$

Note that $\tau_{\rm eff}$ is not the same as the mean optical depth, since $e^{-\tau_{\rm eff}} = \langle e^{-\tau} \rangle \neq e^{-\langle \tau \rangle}$. Here $\langle \rangle$ indicates an average over all possible lines of sight. From the current opacity measurements, we wish to infer the He II photoionization rate. This connection depends on the details of the IGM, including the temperature,

density distribution, and ionized helium fraction.

2.1.1 Fluctuating Gunn-Peterson Approximation

The Gunn-Peterson (1965) optical depth for He II Lyα photons is

$$\tau_{GP} = \frac{\pi e^2}{m_e c} f_\alpha \lambda_\alpha H^{-1}(z) n_{\text{HeII}}. \tag{2.2}$$

Here, the oscillator strength $f_\alpha = 0.416$, $\lambda_\alpha = 304$ Å, and n_{HeII} is the density of singly ionized helium in the IGM. For simplicity, we approximate the Hubble constant as $H(z) \approx H_0 \Omega_m^{1/2} (1 + z)^{3/2}$. Since the Ly$\alpha$ forest probes the low-density, ionized IGM, most of the hydrogen (mass fraction $X = 0.76$) and helium ($Y = 0.24$) are in the form of H II and He III, respectively, after reionization. Under these assumptions, photoionization equilibrium requires

$$\Gamma n_{\text{HeII}} = n_{\text{He}} n_e \alpha_B, \tag{2.3}$$

where Γ is the He II photoionization rate and the case-B recombination coefficient is $\alpha_B = 2.49 \times 10^{-12} (T/10^4 \text{ K})^{-0.7}$ cm^3 s^{-1} according to Storey & Hummer (1995). When analyzing the Lyα forest, we are looking at the low-density, highly ionized IGM; in this regime, the ionizing photons produced by recombinations (near the ionization edge) are reabsorbed in these same regions, so case-B is most appropriate. However, for our purposes, the numerical difference between case-A and case-B is relatively small, and the recombination coefficient is effectively absorbed into the normalization constant described below.

The Lyα forest, and therefore the optical depth, trace the local overdensity Δ of the IGM, where $\Delta \equiv \rho/\bar{\rho}$ and $\bar{\rho}$ is the mean mass density. Since $n_e \propto n_{\text{He}}$ in a highly ionized IGM, equation (2.3) implies that $n_{\text{HeII}} \propto n_{\text{He}}^2 \propto \Delta^2$. The

optical depth is proportional to n_{HeII} (see eq. 2.2), which introduces a Δ^2 factor. Additionally, the temperature of the IGM, which affects the recombination rate, is typically described by a power law of the form $T = T_0 \Delta^{\gamma-1}$ (Hui & Gnedin 1997), where T_0 and γ are taken as constants.[1] Including the above equations and cosmological factors,

$$
\begin{aligned}
\tau_{\text{GP}} \quad \simeq \quad & \kappa \frac{13.6}{\Gamma_{-14}} \left(\frac{T_0}{10^4 \text{ K}} \right)^{-0.7} \left(\frac{\Omega_b h^2}{0.0241} \right)^2 \left(\frac{\Omega_m h^2}{0.142} \right)^{-1/2} \\
& \times \left(\frac{1+z}{4} \right)^{9/2} \Delta^{2-0.7(\gamma-1)},
\end{aligned} \tag{2.4}
$$

where $\Gamma = 10^{-14} \Gamma_{-14} \text{ s}^{-1}$.

The fluctuating Gunn-Peterson approximation (FGPA) (e.g., Weinberg 1999), equation (2.4), relates the effective optical depth, or the continuum normalized flux, to the local overdensity Δ and the photoionization rate Γ_{-14}. This approximation shows the relationship between the opacity and the IGM, but it ignores the effects of peculiar velocities and thermal broadening on the Lyα lines. In practice, when comparing to observations an overall proportionality constant, κ, is introduced to the right hand side of equation (2.4) to compensate for these factors, as described in §2.1.3. This normalization also incorporates the uncertainties in $T_0, \Omega_b, \Omega_m,$ and h.

2.1.2   Lyα Absorption

To fully describe helium reionization and compute the detailed features of the Lyα forest, complex hydrodynamical simulations of the IGM, including radiative transfer effects and an inhomogeneous background, are required. Recent simula-

---

[1] In actuality, during and after helium reionization both T_0 and γ likely become redshift- and density-dependent. We will consider such effects in §2.1.2 and §2.3.3.

tions (Sokasian et al. 2002; Paschos et al. 2007; McQuinn et al. 2009) have made great advances to incorporate the relevant physics and to increase in scale. The simulations remain computationally intensive, and they cannot simultaneously resolve the ~ 100 Mpc scales required to adequately study inhomogeneous helium reionization and the much smaller scales required to self-consistently study the Lyα forest, necessitating some sort of semi-analytic prescription to describe baryonic matter on small scales. On the other hand, the semi-analytic approach taken here, including fluctuations in the ionizing background, should broadly reproduce the observed optical depth, especially considering the uncertainties in the measurements and the limited availability of suitable quasar lines of sight. To outline, the model has four basic inputs: the IGM density distribution $p(\Delta)$, the temperature-density relation $T(\Delta)$, the radiation background distribution $f(J)$, and the mean helium ionized fraction $\bar{x}_{\text{HeIII}}$.

Miralda-Escudé et al. (2000) suggest the volume-weighted density distribution function

$$p(\Delta) = A\Delta^{-\beta} \exp\left[-\frac{\left(\Delta^{-2/3} - C_0\right)^2}{2\left(2\delta_0/3\right)^2}\right], \tag{2.5}$$

where $\delta_0 = 7.61/(1+z)$ and β (for a few redshifts) are given in Table 1 of their paper. Intermediate β values were found using polynomial interpolation. The remaining constants, A and C_0, were calculated by normalizing the total volume and mass to unity at each redshift. The distribution matches cosmological simulations reasonably well for the redshifts of interest,[2] i.e. $z = 2 - 4$. Although this form does not incorporate all the physics of reionization and was not generated with the current cosmological parameter values, the overall behavior should be sufficient for the purposes of our model.

---

[2]More recent simulations by Pawlik et al. (2009) and Bolton & Becker (2009) basically agree with the above $p(\Delta)$ for low densities, which the Lyα forest primarily probes.

A current topic of discussion is the thermal evolution of the IGM during and after helium reionization. The temperature-density relation should vary as a function of redshift and density; notably, helium reionization should increase the overall temperature by a factor of a few (Hui & Gnedin 1997; Gleser et al. 2005; Furlanetto & Oh 2008b; McQuinn et al. 2009), which may have been observed (Schaye et al. 2000; Ricotti et al. 2000; Becker et al. 2011). As mentioned in §2.1.1, the temperature is assumed to follow a power law $T = T_0 \Delta^{\gamma-1}$ in the FGPA. Generally, $T_0 \sim 1 - 2 \times 10^4$ K and $1 \leq \gamma \leq 1.6$ should broadly describe the post-reionization IGM (e.g., Hui & Gnedin 1997), but the exact values are a matter of debate. Unless otherwise noted, we use $T_0 = 2 \times 10^4$ K and $\gamma = 1$ throughout our calculations. The isothermal assumption also suppresses the temperature, and therefore density, dependence of the recombination coefficient α_B.

A uniform radiation background has been a common assumption in previous studies, but the sources (quasars) for these photons are rare and bright. Therefore, random variations in the quasar distribution create substantial variations in the high-frequency radiation background (Furlanetto & Oh 2008a; McQuinn et al. 2009; Meiksin 2009). Furthermore, the $1/r^2$ intensity profiles of these sources induce strong small-scale fluctuations (Furlanetto 2009b), which may in turn significantly affect the overall optical depth of the Lyα forest. For the probability distribution $f(J)$ of the angle-averaged specific intensity of the radiation background J, we follow the model presented in Furlanetto (2009a). In the post-reionization limit, the probability distribution can be computed exactly for a given quasar luminosity function and attenuation length, assuming that the sources are randomly distributed (following Poisson statistics). This distribution can be derived either via Markov's method (Zuo 1992) or via the method of characteristic functions (Meiksin & White 2003).

During reionization, the local He III bubble radius, i.e. the horizon within which ionizing sources are visible, varies across the IGM and so becomes another important parameter. Due to the rarity of sources, with typically only a few visible per He III region, a Monte Carlo treatment best serves this regime (Furlanetto 2009a). For a given bubble of a specified size, we randomly choose the number of quasars inside each bubble according to a Poisson distribution. Each quasar is then randomly assigned a location within the bubble as well as a luminosity (via the measured luminosity function). Next, we sum the specific intensity from each quasar. After 10^6 Monte Carlo trials, this procedure provides $f(J)$ for a given bubble size; the solution converges to the post-reionization scenario for an infinite bubble radius. The final ingredient is the size distribution of discrete ionized bubbles, which is found using the excursion set approach of Furlanetto & Oh (2008a) (based on the hydrogen reionization equivalent from Furlanetto et al. 2004). After integrating over all possible bubble sizes, $f(J)$ depends on the parameters z, R_0, and $\bar{x}_{\mathrm{HeIII}}$, in addition to the specified luminosity function. Here, R_0 is the distance from a quasar where a system that is sufficiently neutral to absorb the helium-ionizing photons is typically located, i.e. where the optical depth for these photons reaches unity.

In the following calculations, we scale J (which is evaluated at a single frequency) to Γ (which integrates over all frequencies) simply using the ratio of the mean photoionization rate to the mean radiation background. This is not strictly correct, because higher frequency photons have larger attenuation lengths and so more uniform backgrounds; however, it is a reasonable prescription because the ionization cross section falls rapidly with photon frequency. However, it does mean that, for now, we ignore the large range in spectral indices of the ionizing sources (see below), which modulates the shape of the local ionizing background and leads to an additional source of fluctuations in Γ relative to J that we do not
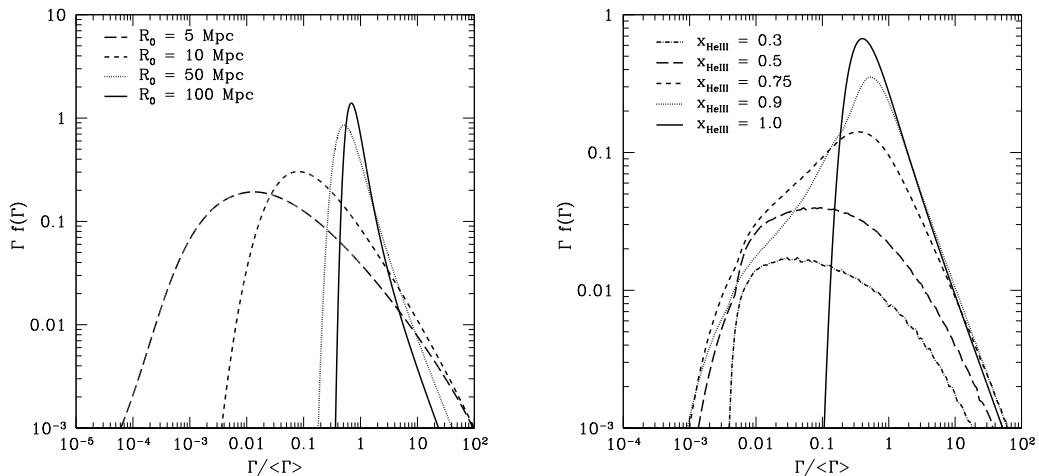
Figure 2.1 Distribution of the photoionization rate Γ relative to its mean value in a fully ionized IGM, $\langle\Gamma\rangle$, at redshift $z = 2.5$. *Left panel:* The curves assume $R_0 = 5, 10, 50$, and 100 Mpc, from widest to narrowest, in a post-reionization universe. *Right panel:* The curves take $\bar{x}_{\rm HeIII} = 0.3, 0.5, 0.75, 0.9$, and 1.0, from lowest to highest at peak, for $R_0 = 35$ Mpc.

model. The largest problem occurs during helium reionization, when the highest energy photons can travel *between* He III regions (a process we ignore); however, they have small ionization cross sections and so do not significantly change our results, except very near the end of that process (Furlanetto 2009a). We allow for this frequency dependence in the attenuation length and calculate Γ directly from sources in later chapters, addressing these issues.

For the majority of this chapter, we consider the IGM to be fully ionized, i.e. $\bar{x}_{\rm HeIII} = 1.0$. In this post-reionization regime, R_0 determines the shape of $f(\Gamma)$, given the redshift and other model assumptions. We show several example distributions in the left panel of Figure 2.1. From widest to narrowest, the curves correspond to $R_0 = 5, 10, 50$, and 100 Mpc ($z = 2.5$). Smaller attenuation lengths yield a greater spread in Γ. Qualitatively, more sources contribute to ionizing a given patch of the IGM for higher R_0, making the peak photoionization rate more likely, i.e., the curve is narrower. A uniform background corresponds to

15

$R_0 \to \infty$. Although low Γ values are more likely for low R_0, the high-Γ tail is nearly independent of R_0. This is because a large Γ occurs within the "proximity zone" of a single quasar, making it relatively independent of contributions from much larger scales (unless R_0 is much smaller than the proximity zone itself). During reionization, as in §2.4, the ionized fraction *and* the mean free path affect the distribution function, as shown in the right panel of Figure 2.1. Here, we take $z = 2.5$, $R_0 = 35$ Mpc, and $\bar{x}_{\mathrm{HeIII}} = 0.3, 0.5, 0.75, 0.9,$ and 1.0 (from lowest to highest at the peak). A broader distribution of photoionization rates is expected, because the large spread in He III bubble sizes restricts the source horizon inhomogeneously across the Universe.

To estimate τ_{eff} (or F), we integrate over all densities and photoionization rates:

$$F = e^{-\tau_{\mathrm{eff}}} = \int_0^\infty d\Gamma f(\Gamma) \int_0^\infty d\Delta e^{-\tau(\Delta|\Gamma)} p(\Delta). \qquad (2.6)$$

This integral is valid if Γ and Δ are uncorrelated. Since relatively rare quasars ionize He II, random fluctuations in the number of sources (as opposed to their spatial clustering) dominate the ionization morphology (McQuinn et al. 2009), justifying our assumption of uncorrelated IGM densities and photoionization rates.

2.1.3   The UV Background from Quasars

Since quasars ionize the He II in the IGM, the UV metagalactic background can, in principle, be calculated directly from distribution and intrinsic properties of quasars. Currently, these details, i.e. the quasar luminosity function and attenuation length, are uncertain. The following method for estimating Γ is used

as a reference for the semi-analytic model. The He II ionization rate is

$$\Gamma = 4\pi \int_{\nu_{\text{HeII}}}^{\infty} \frac{J_\nu}{h\nu} \sigma_\nu d\nu, \tag{2.7}$$

where $\sigma_\nu = 1.91 \times 10^{-18} (\nu/\nu_{\text{HeII}})^{-3}$ cm^2 is the photoionization cross section for He II and ν_{HeII} is the photon frequency needed to fully ionize helium. For the radiation background at frequency ν, J_ν, we assume a simplified form, the absorption-limited case in Meiksin & White (2003):

$$J_\nu = \frac{1}{4\pi} \epsilon_\nu(z) R_0(z), \tag{2.8}$$

where ϵ_ν is the quasar emissivity and R_0 is the attenuation length.

We begin with the B-band emissivity ϵ_B, derived from the quasar luminosity function (QLF) in Hopkins et al. (2007, hereafter HRH07). To convert this to the extreme-UV (EUV) frequencies of interest, we follow a broken power-law spectral energy distribution (Madau et al. 1999):

$$L(\nu) \propto \begin{cases} \nu^{-0.3} & 2500 < \lambda < 4600 \text{ Å} \\ \nu^{-0.8} & 1050 < \lambda < 2500 \text{ Å} \\ \nu^{-\alpha} & \lambda < 1050 \text{ Å}. \end{cases} \tag{2.9}$$

The EUV spectral index α is a source of debate and is not the same for all quasars. Telfer et al. (2002) find a wide range of values for individual quasars, e.g., $\alpha = $ -0.56 for HE 2347-4342 and 5.29 for TON 34. Most quasars lie closer to the mean, but HE 2347-4342 is a He II Lyα line of sight in §2.2. Unless otherwise noted, we use the mean value $\langle\alpha\rangle \approx 1.6$ from Telfer et al. (2002), ignoring the variations in α. Zheng et al. (1997) found $\langle\alpha\rangle \approx 1.8$, which serves as a comparison. The uncertainty in the spectral index α affects the amplitude, not the shape, of the Γ

curve derived from the QLF (see Fig. 2.2). Since our semi-analytic calculations are normalized to a single point on the Γ curve, this uncertainty translates into an amplitude shift in our results, i.e. changes κ.

The next ingredient for J_ν is the attenuation length of helium-ionizing photons R_0. As described above, R_0 depends on the photon frequency; for example, high-energy photons can propagate larger distances. For simplicity, we use a single, frequency-averaged attenuation length and focus only on the redshift evolution (in any case, the absolute amplitude can be subsumed into our normalization factor κ below). For concreteness, we apply the *comoving* form found in Bolton et al. (2006):

$$R_0 = 30 \left(\frac{1+z}{4} \right)^{-3} \text{ Mpc,} \tag{2.10}$$

which assumes the number of Lyman limit systems per unit redshift is proportional to $(1+z)^{1.5}$ (Storrie-Lombardi et al. 1994) and uses the normalization based on the model of Miralda-Escudé et al. (2000). This simple assumption is revisited in later chapters, where we allow frequency dependence. An alternate approach, probably more appropriate during reionization itself, is to estimate the attenuation length around individual quasars, as in Furlanetto & Oh (2008a). This method gives a similar value at $z = 3$ but with a *slower* redshift evolution, which would only strengthen our conclusions. This empirical equation for the mean free path (with the above quasar emissivity) provides the photoionization rate Γ, shown in Figure 2.2. The photoionization rate from the Madau et al. (1999) QLF (with $\alpha = 1.6$ and 1.8) is also included in the figure to illustrate the effect of uncertainties in the quasar properties. The spectral index has a greater effect on the amplitude than the differing QLFs.

As noted in §2.1.1, comparing our FGPA treatment to the real Lyα forest data requires an uncertain correction to the $\tau - \Delta$ relation in equation 2.4. For this
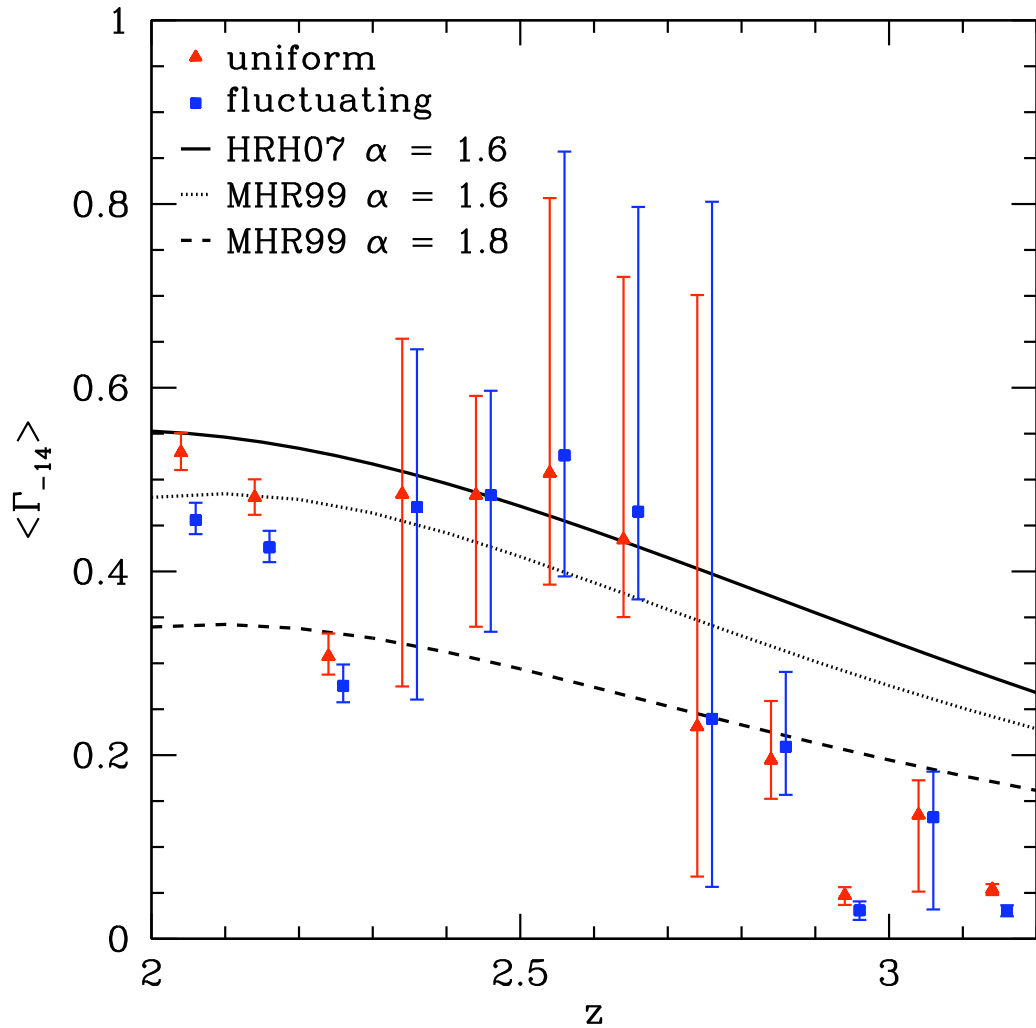
Figure 2.2 Evolution of the mean photoionization rate (in units of 10^{-14} s^{-1}) with redshift. The solid curve represents the inferred ionization rate from the HRH07 quasar luminosity function with $\alpha = 1.6$. The dotted (dashed) curve follows Madau et al. (1999) with extreme-UV spectral index $\alpha = 1.6$ (1.8). All take the attenuation length from eq. (2.10). The points (with a slight redshift offset) show the reconstructed photoionization rate given the measured effective optical depth, assuming a uniform (triangles) and fluctuating (squares) radiation background. The results are fixed to the solid curve at $z = 2.45$.

purpose, we assume the above emissivity and attenuation length to be accurate. Then, the semi-analytic model is adjusted so that the predicted τ_{eff} matches the measured value at a particular redshift. To do so, we insert a prefactor, κ, to the right hand side of equation (2.4). This factor compensates for line blending and other detailed physics ignored by the FGPA, but it also includes any uncertainties in the underlying cosmological or IGM parameters (such as T_0). A suitable normalization redshift should be after reionization and have data from more than one line of sight (see the right panel of Fig. 2.3). Throughout this work, we take $z = 2.45$ as our fiducial point.

If κ is a constant with redshift, our choice of reference point mainly affects the overall amplitude of the photoionization rate or attenuation length, not the redshift evolution. However, since κ depends on the IGM properties, it may change with redshift, density, and/or temperature. For example, an increase in temperature broadens the widths of the absorption lines in the Lyα forest, decreasing the importance of saturation but increasing the likelihood of line blending. Reionization, a drastic change to the IGM, should also affect κ. Here, we take κ to be independent of z. The precise value lies somewhere between 0.2 and 0.7, depending on the specific model. Furlanetto & Oh (2009) find $\kappa = 0.3$ for the post-reionization hydrogen Lyα effective optical depth, which is similar to our values. In any case, we emphasize that our method *cannot* be used to estimate the absolute value of the ionizing background – for which detailed simulations are necessary – but we hope that it can address the redshift evolution of Γ.

2.2 Evolution of the He II Effective Optical Depth

Measurements of the He II effective optical depth are challenging. Suitable lines of sight require a bright quasar with sufficient far-UV flux and no intervening
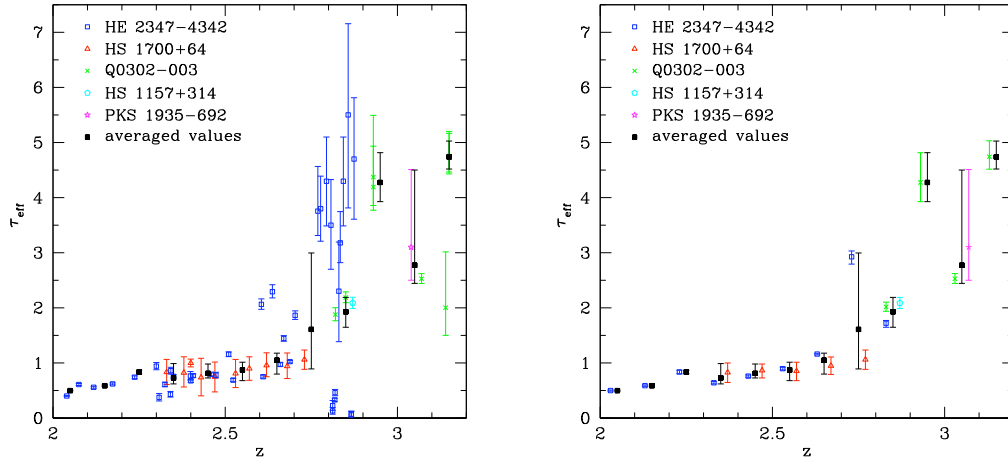
Figure 2.3 Evolution of the He II effective optical depth based on the observations of the Lyα forest for five quasar spectra: HE 2347-4342, HS 1700+64, Q0302-003, HS 1157+314, and PKS 1935-692. The squares are the opacity measurements averaged over redshift bins $\Delta z = 0.1$ with suggestive uncertainties. *Left panel:* Data and uncertainties as quoted in the literature are plotted. *Right panel:* The average values for each line of sight are displayed, elucidating the origin of the uncertainties in the average opacities used throughout the chapter. The small redshift offsets within each bin are for illustrative purposes only.

Lyman-limit systems. As of 2009, only five quasar spectra have provided He II opacity measurements appropriate for our analysis, displayed in the left panel of Figure 2.3 with the averaged values. Zheng et al. (2004a) measure a lower limit on the optical depth at $z \sim 3.5$ from a sixth sightline, SDSS J2346-0016; we do not include any lower limits in any subsequent calculations, but we reference this measurement in §2.4. Due to the limited scope of the data, the observed opacities may not be representative of the IGM as a whole.

HE 2347-4342: This quasar ($z_{\mathrm{em}} = 2.885$) is especially bright; therefore, this line of sight has been extensively analyzed. Zheng et al. (2004b) completed the most comprehensive investigation in the pre-COS era, covering the redshift range $2.0 < z < 2.9$, including Lyα and Lyβ. Zheng et al. (2004b) and Shull et al. (2004) ($2.3 < z < 2.9$ and Lyα only) utilized high-resolution spectra from the Far Ultra-

violet Spectroscopic Explorer (FUSE; $R \sim 20,000$) and the Very Large Telescope (VLT; $R \sim 45,000$). An older and lower resolution study, Kriss et al. (2001), covered $2.3 < z < 2.7$ with FUSE. Below redshift $z = 2.7$, the effective helium optical depth evolves smoothly. At higher redshifts, the opacity exhibits a patchy structure with very low and very high absorption, often described respectively as voids and filaments in the literature.

HS 1700+64: The Lyα forest of this quasar ($z_{\mathrm{em}} = 2.72$) has been resolved with FUSE over the redshift range $2.29 \lesssim z \lesssim 2.75$ (Fechner et al. 2006). An older study using the Hopkins Ultraviolet Telescope (HUT) is consistent with the newer, higher resolution results (Davidsen et al. 1996). The helium opacity evolves smoothly and exhibits no indication of reionization.

Q0302-003: The spectrum of this quasar ($z_{\mathrm{em}} = 3.286$) was observed with the Space Telescope Imaging Spectrograph (STIS) aboard the Hubble Space Telescope (HST) at 1.8 Å resolution (Heap et al. 2000). The effective optical depth generally increases with increasing redshift over $2.77 \lesssim z \lesssim 3.22$, but the reported data exclude a void at $z \sim 3.05$ due to a nearby ionizing source (Bajtlik et al. 1988; Zheng & Davidsen 1995; Giroux et al. 1995). The data were averaged over redshift bins of $\Delta z \simeq 0.1$. Hogan et al. (1997) presented an analysis using the Goddard High Resolution Spectrograph (GHRS) which generally agrees with the later study but quoted a noticeably lower He II optical depth near $z \sim 3.15$. Additionally, we have included data (with $\Delta z \simeq 0.1$ bins) from the Worseck & Wisotzki (2006) re-analysis of the Heap et al. (2000) data; note that they include all uncontaminated regions of the spectrum, particularly the transmission region at $z \sim 3.05$.

HS 1157+314: Reimers et al. (2005) obtained low resolution HST/STIS spectra of the He II Lyα forest toward this quasar ($z_{\mathrm{em}} \sim 3$). Over the redshift range

($2.75 \leq z \leq 2.97$) of the study a patchy structure, similar to HE 2347-4342, is present. The given optical depth was averaged over a redshift bin of $\Delta z \simeq 0.1$.

PKS 1935-692: The HST/STIS spectrum for this quasar ($z_{em} = 3.18$) was analyzed by Anderson et al. (1999). Only one optical depth was quoted, but the spectrum exhibited the usual fluctuations.

To merge these data sets, we initially binned them in redshift intervals of 0.1, starting with $z = 2.0$. Each bin was assigned the median redshift value, e.g. $z = 2.35$ for $2.3 \leq z < 2.4$. To objectively combine the data, the transmission flux ratios for each data set were averaged (weighted by redshift coverage) in the redshift bins. Then, the values for each quasar were averaged, since multiple data sets may cover the same line of sight. Finally, if more than one line of sight contributes to a bin, the fluxes are averaged once again. The process translates the left panel to the right panel of Figure 2.3. The uncertainties along each line of sight in the right panel are simply the errors from each separate point in the literature, added in quadrature, without regard to systematic errors; our averaged values then take errors equal to the range spanned by these separate lines of sight. For the remainder of the chapter, the error bars result from assuming $F \pm dF$ for each redshift bin, where F are the squares and $\pm dF$ are the upper/lower error bars on the squares in the figure. The small number of well-studied lines of sight limits the amount of truly quantitative statements that can be made.

2.3   Results

2.3.1   Mean He II Photionization Rate

We now apply our semi-analytic model to the observed He II opacity found in the right panel of Figure 2.3. For each redshift bin, the photoionization rate

is calculated by iteratively solving equation (2.6), i.e. varying $\langle\Gamma\rangle$ (the mean photoionization rate for a fully ionized IGM) until F matches the measurements. As noted in §2.1.2, a mean free path (eq. 2.10) is needed to determine $f(\Gamma)$ for the fluctuating background, but the uniform case has no such requirement except insofar as it affects $\langle\Gamma\rangle$.

First, to provide some intuition, we fix κ to be the same for both cases (here, $\kappa = 0.408$) and plot the resulting effective optical depth in Figure 2.4, given the emissivity and mean free path from §2.1.3. The figure shows the redshift evolution of this optical depth for uniform (solid) and fluctuating (dashed) radiation backgrounds. Interestingly, τ_{eff} is significantly smaller for a uniform background, especially at higher redshifts (probably due to the shrinking attenuation length assumed in the fluctuating model). This is because most points in the IGM have $\Gamma < \langle\Gamma\rangle$ for the fluctuating background, so most of the IGM has a *higher* opacity; the "proximity zones" around each quasar are not sufficient to compensate for this effect. The measured opacities are included in the figure for reference, showing that the shapes of both (normalized) models are consistent with observations for $z < 2.8$ but deviate significantly at higher redshifts.

In practice, τ_{eff} is the measured quantity, from which we try to infer Γ. We find that, for the fiducial attenuation lengths, including a realistic fluctuating background increases the required $\langle\Gamma\rangle$ by about a factor of two – a nontrivial effect that is important for reconciling quasar observations with the forest. The magnitude of the required adjustment is comparable to that found by Bolton et al. (2006), who used numerical simulations. However, as we have emphasized above, we cannot use our model to estimate the absolute value of the ionizing background because the FGPA does not fully describe the Lyα forest; instead we need a renormalization factor κ. For the remainder of this chapter, we therefore

fix the photoionization rate at the $z = 2.45$ HRH07 value (together with our fiducial R_0), as described in §2.1.3. This procedure gives $\kappa = 0.641$ and 0.408 for the uniform and fluctuating background, respectively. We strongly caution the reader that the remainder of our quoted results will therefore mask the overall amplitude disparity between these two cases, and we will focus on the redshift evolution of Γ instead.

Figure 2.2 displays the mean photoionization rate for a uniform (triangles) and fluctuating (squares) UV background (normalized to the fiducial point). The curves represent the photoionization rate inferred from various quasar luminosity functions, as described in §2.1.3. Since the $z = 2.45$ reference point was chosen arbitrarily, the overall amplitude should not be considered reliable, which is emphasized by the spread in the QLF curves. The difference between the fluctuating and uniform UV background is small and certainly within the uncertainties. The effect of including fluctuations on the photoionization rate is not straightforward. Generally, at lower z, the fluctuating Γ is smaller than the uniform result, and the opposite is true for higher redshift. The redshift of the crossover between the two behaviors depends on the amplitude of the measured transmission ratio; a higher F decreases this crossover redshift.

We therefore attribute this effect to changing the characteristic overdensity of regions with high transmission, which is larger at lower redshifts because of the Universe's expansion. In this regime, where the underlying density field itself has a relatively broad distribution, the fluctuating ionizing field makes less of a difference to the required $\langle \Gamma \rangle$. Remember, however, that these relatively small changes are always swamped by the differing κ's, and a fluctuating background always requires a larger $\langle \Gamma \rangle$ than the uniform case.

For $z < 2.7$, the normalized points lie near the HRH07 curve. The averaged
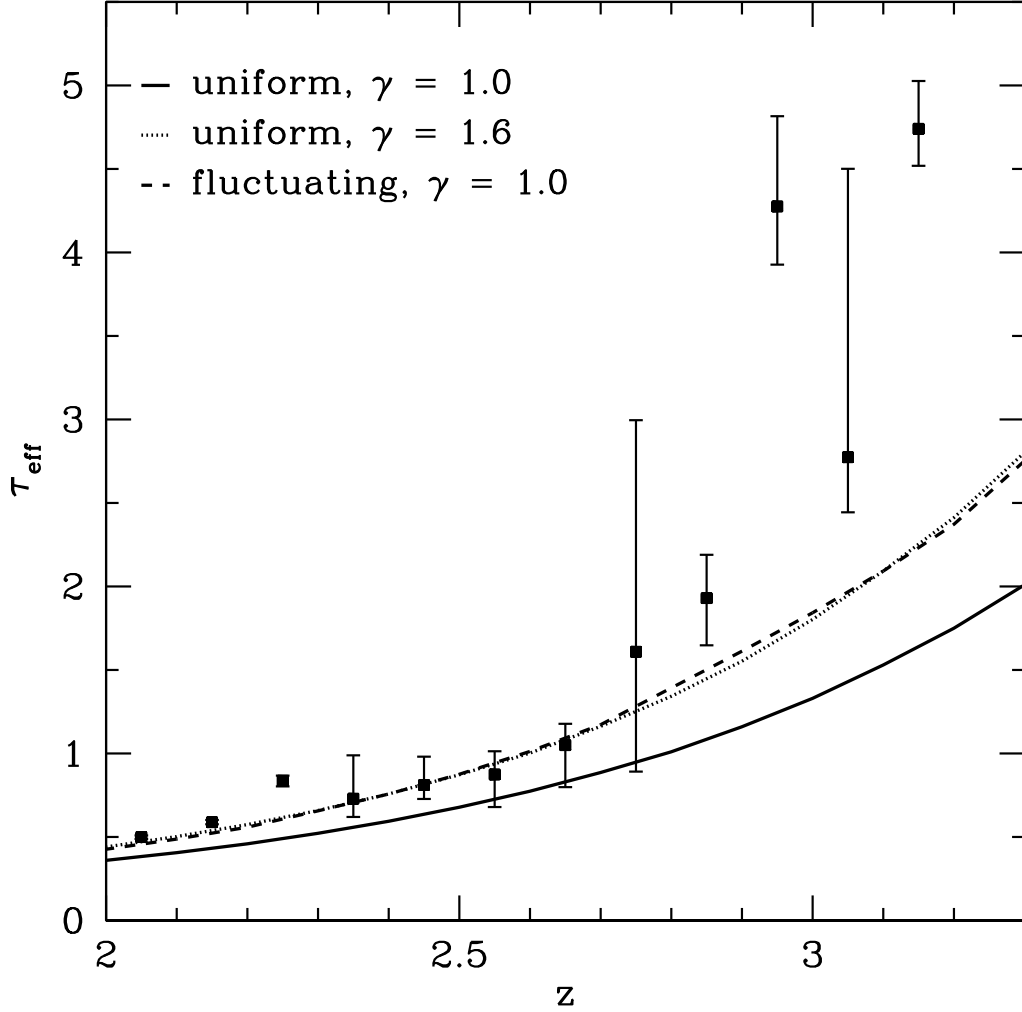
Figure 2.4 The He II effective optical depth, assuming the HRH07 QLF and eq. (2.10), as a function of redshift. The normalization for all curves is constant, $\kappa = 0.408$. The solid (dotted) curve is based on a uniform radiation background, with $\gamma = 1.0$ (1.6). The dashed curve represents a fluctuating background with an isothermal temperature-density relation. The average measured opacities are shown for reference.

opacity at $z = 2.25$, which is significantly higher, relies on a single line of sight, HE 2347-4342, and differs significantly from the trend seen in Figure 2.3. As expected, the inferred Γ fluctuates considerably over this redshift range. In part, these variations are due to the limited amount of data, both in the number and redshift coverage of usable quasar sightlines. But the UV background fluctuates considerably, especially during reionization (see the $f(\Gamma)$ discussion in §2.1.2). For $z > 2.8$, the calculated photoionization rate consistently undershoots the model prediction, possibly indicating the end of helium reionization around that time: there is much more He II than can be accommodated by a smoothly varying emissivity or attenuation length.

2.3.2 Evolution of the Attenuation Length

Because the measured quasar emissivity evolves smoothly with redshift, the most natural interpretation of this discontinuity is in terms of the attenuation length, which intuitively evolves rapidly at the end of reionization when He III regions merge together and sharply increase the horizon to which ionizing sources are visible. Following the prescription for the UV background in §2.1.3, we calculate the mean free path R_0, given the HRH07 QLF and the Γ_{-14} from the previous section. This procedure amounts to varying the solid curve, via R_0, to match the points in Figure 2.2. The redshift evolution of the attenuation length for uniform (triangles) and fluctuating (squares) radiation backgrounds is plotted in Figure 2.5, with equation (2.10) as a reference. The normalization remains the same as the previous section, i.e. $z = 2.45$ is the fiducial point.

Similarly to the inferred photoionization rate, the points vary about the reference curve for $z < 2.7$ and depart from it for $z > 2.8$. The uncertainties, which are shown only for the uniform UV background (but are comparable for the other
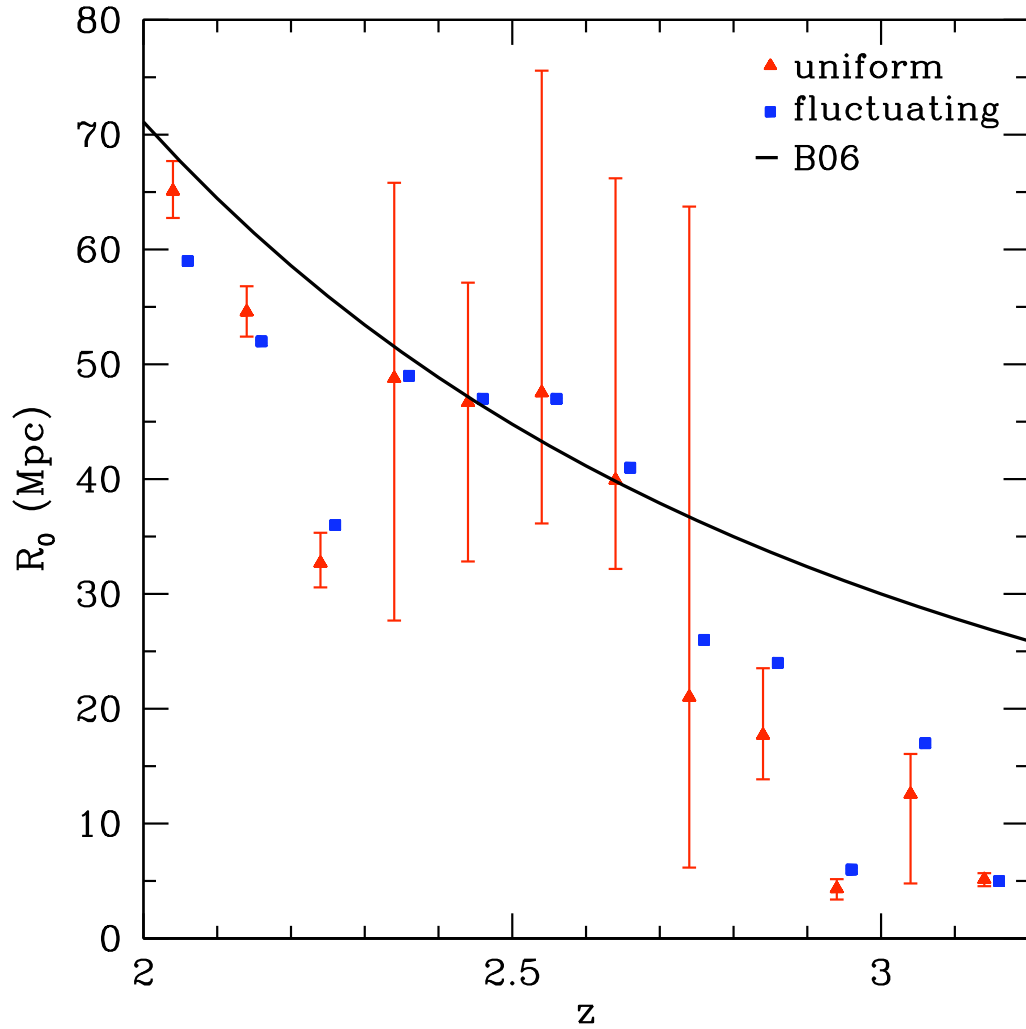
Figure 2.5 Evolution of the helium-ionizing attenuation length with redshift. The calculated mean free path generally increases with a discontinuity around $z = 2.8$. The fluctuating (squares) background appears to smooth the evolution as compared to the uniform (triangles) background. The results are matched to the Bolton et al. (2006) attenuation length (solid curve) at $z = 2.45$. The estimated uncertainties are shown only for the uniform case but are similar for both.

case), are again quite large. Incorporating fluctuations reduces the severity of, but does not eliminate, the jump in the evolution of the attenuation length. Once again the results lie consistently below the curve for higher redshifts. From the viewpoint of Γ or R_0, there appears to be a systematic change in behavior above $z \approx 2.8$. The marked decrease in R_0 that is required, by at least a factor of two from the fiducial model, indicates an important change in the state of the IGM. However, as we have described above, a single attenuation length is no longer appropriate during reionization, so in §2.4 we will turn to models of inhomogeneous reionization.

2.3.3 The IGM Temperature-Density Relation

As discussed in §2.1.2, the temperature-density relation of the IGM is a complicated question and an important component of the semi-analytic model. For the majority of the chapter, we assume an isothermal model, i.e. $\gamma = 1$ in $T = T_0 \Delta^{\gamma - 1}$. In reality, the temperature may depend on the density of the IGM. A further complication arises during (and shortly after) helium reionization when the IGM is inhomogeneously reheated and subsequently relaxes to a power law (Gleser et al. 2005; Furlanetto & Oh 2008b; McQuinn et al. 2009).

To partially address the former issue, we repeat the calculation of Γ for a homogeneous radiation background, but now with $\gamma = 1.6$, shown in Figure 2.6. The difference between the two cases is $\lesssim 30\%$. Overall, the steeper temperature-density relation slightly smoothes the jump in Γ_{-14} near redshift $z \approx 2.8$ but is insufficient to fully explain the observed discontinuity. As expected, the normalization differs between the two equations of state: $\kappa_{\gamma=1.0} = 0.641$ and $\kappa_{\gamma=1.6} = 0.409$ (see Fig. 2.4). In other words, a model with a higher γ requires a higher $\langle \Gamma \rangle$ to achieve the same optical depth. This is because a steeper temperature-density

relation makes the low-density IGM, which dominates the transmission, colder and hence *more* neutral. Overall, then, the temperature-density relation and fluctuating ionizing background lead to a systematic uncertainty of nearly a factor of four in the mean photoionization rate inferred from the He II forest.

2.4   Models for He II Reionization

We have seen that the observations appear to require a genuine discontinuity in the properties of the IGM at $z \approx 2.8$, although large statistical errors stemming from the small number of lines of sight prevent any strong conclusions. This change is often attributed to reionization; here we investigate this claim quantitatively with several "toy" models for the evolution of the helium ionized fraction $\bar{x}_{\text{HeIII}}$. This fraction determines $f(\Gamma)$ as described in §2.1.2. Assuming the HRH07 QLF and the attenuation length given by equation (2.10),[3] we calculate the effective optical depth via equation (2.6). The fiducial point for normalizing κ remains at $z = 2.45$.

Figure 2.7 shows the effective optical depth τ_{eff} and ionized fraction $\bar{x}_{\text{HeIII}}$ as a function of redshift for five reionization models. Each scenario is characterized by the redshift, z_{He}, at which $\bar{x}_{\text{HeIII}}$ reaches 1.0. From left to right in the figure, the curves correspond to $z_{\text{He}} = 2.4, 2.5, 2.7, 3.1$ and $z_{\text{He}} > 3.8$, i.e. post-reionization for the entire redshift range in question. The rate of ionization varies slightly between the models.[4] The measured opacities are plotted for reference, including

---

[3]Again, we note that during helium reionization the attenuation length should be evaluated with reference to individual quasars and independent of the general background; in that case, it does not evolve strongly with redshift, because typically a given point only sees one quasar (Furlanetto & Oh 2008a). A slower redshift evolution in R_0 would only strengthen our conclusion that a significant change is occurring in the IGM around $z \approx 2.8$.

[4]The unevenness in the curves arises because generating our Monte Carlo distributions is relatively expensive computationally, so we only generated a limited number at $\bar{x}_{\text{HeIII}} = (0.3, 0.5, 0.75, 0.9, \text{and } 1.0)$ for each redshift.
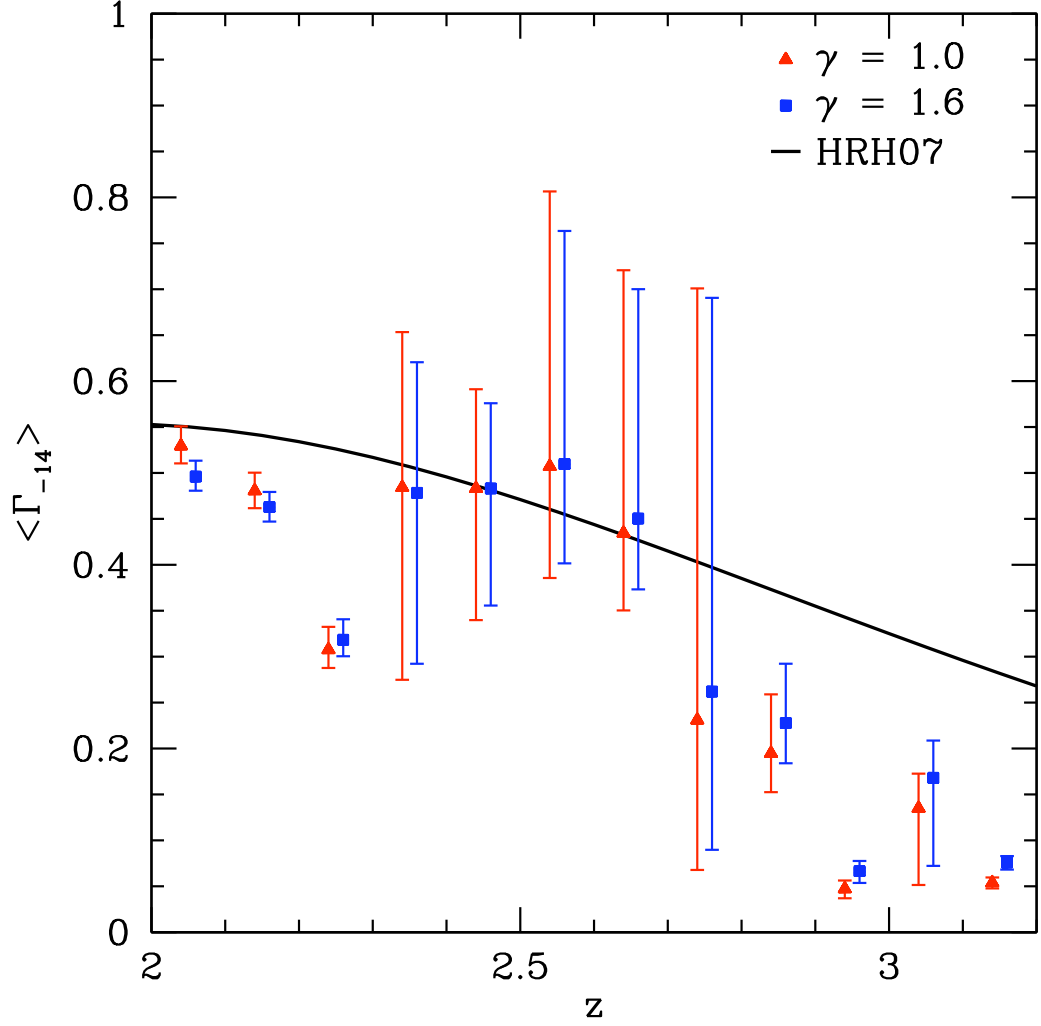
Figure 2.6 Comparison of the inferred photoionization rate (in units of 10^{-14} s^{-1}) for two temperature-density relations, given a homogeneous radiation background. The triangular points are derived using an isothermal model. The square points assume a steeper temperature-density relation, $\gamma = 1.6$. The points have a small redshift offset for illustrative purposes. The photoionization rate computed from the HRH07 quasar luminosity function is plotted for reference. Both models are normalized to the observations at $z = 2.45$.

the recently discovered SDSS J2346-0016 at $z = 3.45$ (Zheng et al. 2004a, 2008). Note that we do not estimate any cosmic variance uncertainty.

The effective optical depth evolves smoothly in the post-reionization regime, which seems compatible with the data below $z \approx 2.8$. The $z_{\mathrm{He}} = 2.7$ model seems to fit the data best, but a range of values for the reionization redshift would be consistent with the existing data. Note that models with $z_{\mathrm{He}} > 3$ seem to evolve too smoothly; however, none of the curves displays enough of a discontinuity to match the data completely. Obviously, more lines of sight at $z \gtrsim 3$ are needed to reduce the wide cosmic variance.

2.5   Discussion

We have applied a semi-analyic model to the interpretation of the He II Lyα forest, one of the few direct observational probes of the epoch of helium reionization. Using simple assumptions about the IGM, the ionization background, and our empirical knowledge of quasars, we have inferred the evolution of the helium phoionization rate and the attenuation length from the He II effective optical depth. We averaged the opacity measurements over 5 sightlines, which show an overall decrease in τ_{eff} with decreasing redshift and a sharp jump at $z \approx 2.8$ with the alternating low and high absorption at higher reshifts. After proper normalization, our model provides good agreement to the lower redshift data, but – assuming smooth evolution in the quasar emissivity and attenuation length – consistently overpredicts $\langle \Gamma \rangle$ above $z \approx 2.8$. Although the uncertainties are large, these results suggest a rapid change in the IGM around that time.

Our semi-analytic model is based on the quasar luminosity function and the helium-ionizing photon attenuation length, which are determined empirically.
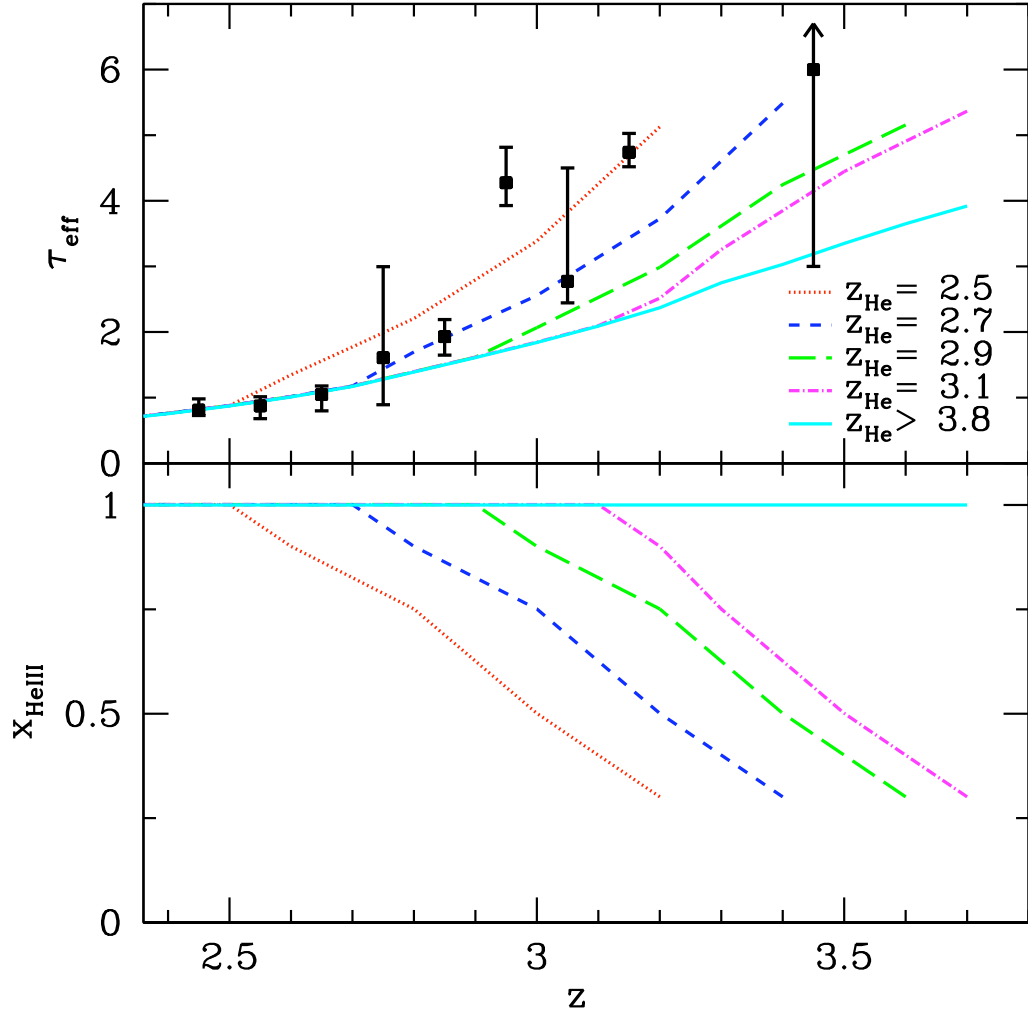
Figure 2.7 The effective helium optical depth and He III fraction for five toy reionization models. From left to right, the curves correspond to helium fully ionized by $z_{He} = 2.5, 2.7, 2.9, 3.1$ and post-reionization (or $z_{He} > 3.8$). The He III fraction evolution is varied slightly between models. The measured opacities are included for reference, including the lower limit at $z = 3.45$ from SDSS J2346-0016 (Zheng et al. 2004a).

The uncertainty in these quantities significantly affects our results. In particular, the plausible range of the mean EUV spectral index, $1.6 \lesssim \alpha \lesssim 1.8$, shifts the amplitude of our results by a factor of about two. Our model takes only the mean value and does not account for the variation in α from different quasars. Furthermore, our treatment of the attenuation length ignores any frequency dependence. However, these factors likely only affect the amplitude, not the evolution, of the inferred photoionization rate, especially the the jump at $z \approx 2.8$. A steeper redshift evolution for the attenuation length would decrease the severity of the feature around $z \approx 2.8$, but a simple power law cannot eliminate it, given our method.

In calculating Γ and R_0, we compared uniform and fluctuating backgrounds. Although helium reionization is thought to be inhomogeneous (see Furlanetto & Oh 2008a), the assumption of a uniform background has been common. We found that the uniform case produces an effective optical depth approximately a factor of two smaller for a fixed $\langle \Gamma \rangle$. Thus, properly incorporating the fluctuating background is crucial for interpreting the He II forest in terms of the ionizing sources. Furthermore, we find that the inclusion of background variations slightly smoothes, but does not remove, the jump in the attenuation length at $z \approx 2.8$. A clear change in the IGM does appear to occur around this redshift.

The discontinuous behavior in Γ and R_0 led us to include helium reionization in our model through the distribution $f(\Gamma)$. During reionization, the ionized helium fraction determines this distribution, and we studied several toy models for the redshift evolution of $\bar{x}_{\mathrm{HeIII}}$. These models suggest $z_{\mathrm{He}} \approx 2.7$ as the best fit to the data, but the statistical uncertainties in τ_{eff} are large. We do not account for cosmic variance and only consider the mean effective optical depth. Our method also makes assumptions that are not valid during reionization, e.g. a power-law

temperature-density relation, but this does not appear to affect the discontinuity significantly. In subsequent chapters, we generate realistic source and density fields to address cosmic variance and the significant fluctuations about the mean.

In fact, the most important caveat to our model is the use of the fluctuating Gunn-Peterson approximation, which is a simplified treatment of the Lyα absorption. The approach ignores the wings of absorption lines, peculiar velocities, and line blending; overall, these effects require us to add an unknown renormalization factor (of order ~ 0.2–0.7) when translating from Γ to optical depth and compromises attempts to measure the absolute value of $\langle \Gamma \rangle$. One danger is the possible redshift evolution of this factor: we have assumed that it does not evolve, but in reality the line structure and temperature of the forest do evolve, especially at the end of reionization. More detailed numerical simulations that incorporate both the baryonic physics of the Lyα forest and the large-scale inhomogeneities of helium reionization are required to explore this fully.

Interestingly, if our interpretation is correct then it appears that helium reionization completes at $z_{\mathrm{He}} \lesssim 3$. This places it several hundred million years *after* the epoch suggested by indirect probes of the H II Lyα forest. Specifically, some measurements of the temperature evolution of the forest show a sharp jump at $z \approx 3.2$ and a shift toward isothermality (Schaye et al. 2000; Ricotti et al. 2000), which has been interpreted as evidence for helium reionization (Furlanetto & Oh 2008b; McQuinn et al. 2009). It is not clear whether this time lag can be made consistent; it probably depends on the details of the line selection in the observations (see the discussion in Furlanetto & Oh 2008b). Moreover, late helium reionization would present further difficulties for an explanation of the $z \approx 3.2$ feature in the H II Lyα forest opacity in terms of helium reionization (see also Bolton et al. 2009). Another indirect constraint is consistent, however, with our

picture: reconstruction of the ionizing background from optically thin metal systems finds an effective optical depth in He II Lyα photons slightly higher than the direct measurements, but with a similar redshift evolution (Agafonova et al. 2005, 2007).

The most significant limitation in the data is the relatively small number of lines of sight, producing large variations in the measured transmission, especially at $z \gtrsim 3$ where the cosmic variance is large. Fortunately, a number of new lines of sight have been found (Zheng et al. 2008; Syphers et al. 2009), and the recent installation of the Cosmic Origins Spectrograph (COS) on the *Hubble Space Telescope* adds a new instrument to our arsenal. Although the nominal wavelength range of COS limits it to $z \gtrsim 2.8$, this is precisely the most interesting range for studying reionization. Our models show that $\tau_{\mathrm{eff}} \lesssim 5$ so long as $x_{\mathrm{HeIII}} \gtrsim 0.3$ (see Fig. 2.7), so there should be a relatively wide redshift range with measurable transmission – especially when considering the wide variations in the ionizing background expected during and after helium reionization (see Fig. 2.1 and Furlanetto 2009a).

Finally, these prospects point out one important difference between He III and H II reionization: the near-uniformity of the ionizing background at the end of H II reionization means that very little residual transmission can be expected at $z \gtrsim 6$ for that event, making the Lyα forest relatively useless for studying reionization. In contrast, the large variance intrinsic to the He II-ionizing background produces much stronger fluctuations and makes the epoch of reionization itself accessible with the He II Lyα forest.

Another interesting difference between helium and hydrogen is the effect of including fluctuations on the photoionization rate inferred from the Lyα forest. We find that assuming a uniform ionizing background *underestimates* Γ by up

to a factor of two, while during hydrogen reionization the effect is much smaller – only a few percent (Bolton & Haehnelt 2007; Mesinger & Furlanetto 2009). During and after helium reionization, the fluctuations are much more pronounced than the hydrogen equivalent, leading to a much broader $f(J)$, so that more of the Universe lies significantly below the mean. For hydrogen reionization, the distributions are much narrower, favoring Γ near the mean. In addition, after hydrogen reionization the density distribution is much wider than $f(\Gamma)$, so that the latter provides only a small perturbation; the opposite is true in our case.

Our general approach is very similar to Fan et al. (2002) and Fan et al. (2006), who also interpreted the H II Lyα forest data at $z \sim 6$ using a uniform ionizing background and the same IGM density model as we have (although in their case that model required extrapolation to the relevant redshifts). They also found a discontinuity in the optical depth (at $z \sim 6.1$), which is often taken as evidence for H II reionization. But during this earlier epoch, that inference is less clear because of the near saturation of the forest and the unknown attenuation length (whose evolution really determines the overall ionizing background, but which may evolve rapidly even after reionization; Furlanetto & Mesinger 2009). Nevertheless, we hope that understanding this discontinuity in the He II forest properties will shed light on the problem of hydrogen reionization.

CHAPTER 3

Semi-Numeric Simulations of He II Reionization

We present fast, semi-numeric methods that incorporate realistic source geometries to explore a large parameter space. We adapt the established hydrogen reionization code DEXM (Mesinger & Furlanetto 2007) to the $z = 3$ Universe. The code applies approximate but efficient methods to produce dark matter halo distributions. From them, it generates ionization maps using analytic arguments. The advantages of this approach are speed, as compared to cosmological simulations, and reasonably accurate spatial information (like halo clustering and a detailed, local density field), as compared to more analytic studies.

These simulations are well-suited to study many features of the helium reionization epoch, including interpreting the Lyα forest and estimating the He-ionizing background. In this chapter, we consider the spatial morphology of He II reionization during and after reionization. Given our ability to span a large parameter space, we aim to pinpoint the assumptions that most strongly impact the results.

We use semi-numeric methods, outlined in §3.1, to approximate the ionization morphology, density field, and sources of ionizing photons at $z = 3$. As a second layer, we place empirically determined active quasars in dark matter halos, following several prescriptions in §3.2. In §3.3, we compare our results and methods with those for hydrogen reionization. We conclude in §3.4.

3.1 Methods

To fully describe helium reionization and compute the detailed features of the Lyα forest, complex hydrodynamical simulations of the IGM, including radiative transfer effects and an inhomogeneous background, are required. Recent N-body simulations (e.g., M09) have advanced both in scale and in the inclusion of relevant physical processes. However, the major limitation is the enormous dynamic range, balancing large ionized regions with small-scale physics, required to model reionization. Generally, this problem is solved in two ways. First, most codes follow only the dark matter, assuming that the baryonic component traces it according to some simplified prescription. They then perform radiative transfer on the dark matter field (perhaps with some modifications to reflect baryonic smoothing). Second, these codes add in the ionizing sources through post-processing, rather than through a self-consistent treatment of galaxy and black hole formation, which is not substantially better than simple analytic models. Also importantly, large simulations remain computationally intensive, limiting the range of parameter space that can be explored in a reasonable amount of time.

We adapt the semi-numeric code DExM[1] (Mesinger & Furlanetto 2007), originally designed to model hydrogen reionization at $z \gtrsim 6$, for lower redshifts and for helium reionization. This code provides a relatively fast semi-numeric approximation to more complicated treatments but remains fairly accurate on moderate and large scales. For full details, see Mesinger & Furlanetto (2007). In brief, we create a box with length $L = 250$ Mpc on each side, populated with dark matter halos determined by the density field. Given these halos, we generate a two-phase ionization field, where the He III fraction is fixed by some efficiency parameter

---

[1]http://homepage.sns.it/mesinger/Sim.html

using a photon-counting method. For our high-level calculations, we additionally adjust the local density field to match recent hydrodynamical simulations.

There are drawbacks to our approach, of course. For one, this semi-numeric method does not follow the progression of He II reionization through a single realization of that process. In order to ensure accurate redshift evolution, photon conservation requires a sharp k-space filter, whereas we use a real-space, top-hat filter, applied to the linear density field (see the appendix of Zahn et al. 2007; Zahn et al. 2011). This filtering can result in "ringing" artifacts from the wings of the filter response, in the limit of a rare source population (as is the case in He II reionization). Moreover, during He III reionization, the relevant ionized sources are short-lived quasars. When a source shuts off, the surrounding regions can begin to recombine in a complex fashion (Furlanetto et al. 2008). Our method does not explicitly follow these recombinations, as we will discuss below. As a consequence, we perform all of our calculations at $z = 3$, near the expected midpoint of the He III reionization according to current measurements. We expect our results to change only modestly throughout the redshift range $z \sim 2.5 - 3.5$, because the source density does not change significantly over this range and the density field evolution is similarly limited.

Our primary concern in adapting DEXM to this period, as compared to the higher redshift regime for which it has been carefully tested, is the increasing nonlinearity of the density field. There are two possible problems. First, the dramatically larger halo abundance may lead to overlap issues with the halo-finding algorithm. Second, the IGM density field will have modest nonlinearities representing the cosmic web. We will address this problem in detail in §3.1.4.

3.1.1 Dark Matter Halos

The backbone of our method is the dark matter halo distribution. In a similar way to N-body codes, we generate a 3D Monte-Carlo realization of a linear density field on a box with $N = 2000^3$ grid cells ($L = 250$ Mpc). This density field is evolved using the standard Zel'dovich approximation (Zel'Dovich 1970). Dark matter halos are identified from the evolved density field using the standard excursion set procedure. Starting on the largest scale (the box size) and then decreasing, the density field is smoothed using a real-space top hat filter at each point. Once the smoothed density exceeds some mass-dependent critical value, the point is associated with a halo of the corresponding mass. Each point is assigned to the most massive halo possible, and halos cannot overlap. We choose our critical overdensity to match the halo mass function found in the Jenkins et al. (2001) simulations at $z = 3$, following the fitting procedure of Sheth & Tormen (1999). The final halo locations are shifted from their initial (Lagrangian) positions to their evolved (Eulerian) positions using first-order perturbation theory (Zel'Dovich 1970). To optimize memory use, we resolve the velocity field used in this approximation onto a lower-resolution, 500^3 grid.

The left panel of Figure 3.1 displays the resultant mass function as points, where the dashed line is the Sheth-Tormen (Sheth & Tormen 1999) result with Jenkins et al. (2001) parameters and the dotted line is the Press-Schechter analytic solution for the mass function (Press & Schechter 1974). We successfully reproduce the former mass function and, therefore, match large numerical simulations reasonably well. The right panel shows our halo power spectrum, defined as $\Delta_{\mathrm{hh}}^2(k, z) = k^3/(2\pi^2 V)\langle|\delta_{\mathrm{hh}}(\mathbf{k}, z)|^2\rangle_k$. Here, $\delta_{\mathrm{hh}}(\mathbf{x}, z) \equiv M_{\mathrm{coll}}(\mathbf{x}, z)/\langle M_{\mathrm{coll}}(z)\rangle - 1$ is the collapsed mass field, and the volume $V = L^3$. Also shown is the prediction from the halo model, which is a semi-analytic method for describing nonlinear
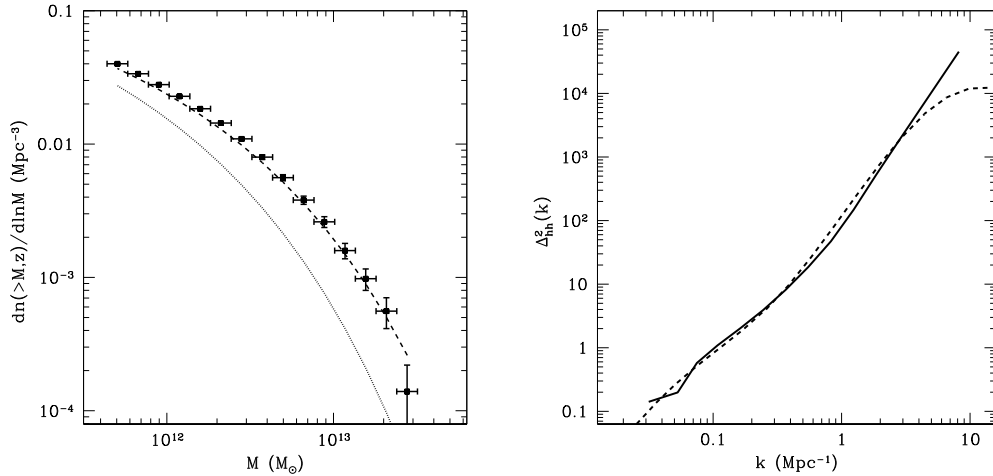
Figure 3.1 *Left panel:* The calculated halo mass function shown as points. The dotted curve is the Press-Schecter analytic mass function. The dashed curve denotes Sheth-Tormen mass function, which agrees with our results by construction. *Right panel:* Halo power spectra. The solid line represents the halo power spectrum measured from our standard ($L = 250$ Mpc) box, and the dashed line is the halo model analytic equivalent.

gravitational clustering. This model matches many statistical properties of large simulations (see Cooray & Sheth 2002). Specifically, all dark matter is assumed to be bound in halos of varying sizes; then, given prescriptions for the distribution of dark matter within halos and the number and spatial distribution of halos, many large-scale statistical properties of dark matter can be calculated, including the halo power spectrum. At small scales, the measured power spectrum diverges from the halo-model equivalent, most likely because we do not include halo density profiles that would dominate at these scales.

Note that the halos with which we are concerned are the most massive at $z = 3$, containing only a few percent of the total mass. This means that overlap between mass filters is not very important, as it might be at lower masses: when a large fraction of the mass is contained inside collapsed objects, the halo filters could then overlap, in which case the ordering at which the cells were examined

would affect the halo distribution and bias our results (Bond & Myers 1996). Fortunately, because we are concerned with quasars inside very massive dark matter halos, this is not a concern for us. This focus on large halos also accounts for the large difference between the Sheth-Tormen and Press-Schechter mass functions in Figure 3.1.

3.1.2 Ionizing Sources

Because we focus on helium reionization, quasars are the only relevant ionizing source.[2] Empirically, quasar properties are reasonably well constrained: the quasar luminosity function (QLF) has been measured to low optical luminosities over a range of redshifts (see the compilation in Hopkins et al. 2007). However, the spectral energy distribution – and hence the transformation of this observed luminosity function to the energies of interest to us – is more uncertain. Furthermore, the relation between quasars and their host dark matter halos is not settled (e.g., Hopkins et al. 2006; Wyithe & Loeb 2007; Conroy & White 2012). These details affect the ionization maps, the photoionization rate, and pertinent range of the halo mass function via the minimum mass. Given these factors, there is no standard approach to the inclusion of quasars in numeric and analytic models. To address this uncertainty, we considered a wide range of models that encompass the spectrum of popular theories.

Given the distribution of dark matter halos found in the previous section, only the halos that host or have hosted quasars contribute to the ionization field. We begin by assuming that each halo above a minimum mass M_{min} is eligible to host a quasar and that a fraction $f_{\mathrm{host}} \leq 1$ actually have hosted one (at either the present time or at some time in the past). Thus, these are the

---

[2]Although stars can produce He II-ionizing photons, their contribution to reionization is most likely extremely small (Furlanetto & Oh 2008a).

relevant sources for the ionization field calculation. As a fiducial value, we take $M_{\mathrm{min}} = 5 \times 10^{11}\ M_\odot$. Next, we assume that these hosts produce ζf_q He II-ionizing photons per helium atom, where we have split this quantity into two factors for conceptional convenience. The first (ζ) is the *average* number of ionizing photons (minus recombinations, see below) across the entire source population, while we will use the latter (f_q) to describe how these photons are distributed amongst the hosts (i.e., it may vary with halo mass). If we then consider a region in which all the ionizing photons are produced by interior sources (and inside of which all of those photons are absorbed), the ionized fraction x_{HeIII} is then

$$\zeta f_{\mathrm{host}} = x_{\mathrm{HeIII}}, \tag{3.1}$$

where the f_q factor has vanished because we are only considering the *total* population (summed over all masses, so that the ionizing efficiency is simply the average value ζ).

The efficiency parameter ζ can be estimated from first principles given a model for quasars (see, e.g., Furlanetto & Oh 2008a). One could compute the average number of He II ionizations per baryon inside of quasars (N_{ion}), estimate the efficiency with which baryons are incorporated into the source black holes (f_{BH}), and estimate the fraction of these photons that escape their host (f_{esc}); then $\zeta \sim f_{\mathrm{BH}} f_{\mathrm{esc}} N_{\mathrm{ion}}$, with additional corrections for the composition of the IGM and the number of photons "wasted" through recombinations. However, we note that ζ *cannot* be inferred directly from the observed luminosity function, because it depends on the total number of ionizing photons emitted by a halo rather than the current luminosity. At minimum, we would require knowledge of the lifetime of the luminous phase of the quasar emission. Conversely, this implies that our choices for M_{min} and f_{host} enforce a quasar lifetime, which we will consider in

§3.2.

This ζ also depends on the recombination history of the IGM, as (to the extent that they are uniform) such recombinations essentially cancel out some of the earlier ionizations (Furlanetto et al. 2004). In practice, recombinations are inhomogeneous and so much more complex to incorporate (Furlanetto & Oh 2005), especially because the small number of quasar sources can allow some regions to recombine substantially before being ionized again by a new quasar (Furlanetto et al. 2008). Our f_{host} parameter can approximately account for the latter effect (if one thinks of some of the "off" halos as having hosted quasars so long in the past that their bubbles have recombined). We also expect that inhomogeneous recombinations are relatively unimportant for the quasar case, at least until the late stages of reionization (Furlanetto & Oh 2008a; Davies & Furlanetto 2012).

Because we lack a strong motivation for a particular value of ζ, we will generally use it as a normalization constant. That is, we will specify x_{HeIII} and a model for the host properties (M_{min} and f_{host}), and then choose ζ to make equation (3.1) true. As described above, any such choice can be made consistent with the luminosity function if we allow the quasar lifetime to vary.

Throughout most of this and subsequent chapters, we consider two basic source models. Neither is meant to be a detailed representation of reality: instead, they take crude, but contrasting, physical pictures meant to bracket the real possibilities. In the first, our *fiducial method*, we imagine that some quasars existed long enough ago that any He III ions they created have since recombined, so only a fraction of the halos (which recently hosted quasars) contribute to the ionization field. We therefore assume that during reionization (1) only a fraction f_{host} of halos above $M_{\mathrm{min}} = 5 \times 10^{11} \ M_{\odot}$ have hosted sources that contribute to

the ionization field at the specified redshift, and that (2) each halo with a source, regardless of its mass, produces the same total number of ionizing photons. The latter assumption effectively fixes our f_q parameter, which must vary inversely with mass.

We are left with two free parameters, f_{host} and ζ. For the first, we set $f_{\text{host}} = x_{\text{HeIII}}/Q_{\text{ion}}$ as the fraction of halos that contain sources, where Q_{ion} is the *total* number of ionizing photons produced per helium atom (integrated over all past times). Physically, this means that at the moment the universe becomes fully ionized we would have $f_{\text{host}} = 1/Q_{\text{ion}}$. In this case, the other halos would have had ionizing sources so far in the past that their He III regions have recombined since formation.

We then set ζ so as to produce the correct x_{HeIII} given the source density from above. This efficiency effectively determines the size of each ionized bubble: thus their number density and size together fix the net ionized fraction.

Our second source model (which we will refer to as the *abundant-source method*) is chosen primarily as a contrast to this fiducial one. We assume that (1) all halos above $M_{\text{min}} = 5 \times 10^{11}\ M_\odot$ have hosted sources, even when the global x_{HeIII} is small, and that (2) the ionizing efficiency of each halo is proportional to its mass (which demands that $f_q = 1$). This means that (when averaged over large scales) the quantity $\zeta f_{\text{host}} f_q$ in equation (3.1) reduces to the simple form ζf_{coll} (the same form typically used for hydrogen reionization; Furlanetto et al. 2004). We then choose ζ to satisfy equation (3.1) for a specified x_{HeIII}.

Neither of these approaches is entirely satisfactory, but they bracket the range of plausible models reasonably well and so provide a useful gauge of the robustness of our predictions. Our fiducial model fails to match naive expectations in two ways. First, it assumes that only a fraction of massive halos host black holes

that have ionized their surroundings. One possible interpretation is that some of these sources appeared long ago, so that their ionized bubbles have recombined. However, in most cases the required number of recombinations would be much larger than expected (Furlanetto et al. 2008). A simpler interpretation is that many of these halos simply lack black holes. While this fails to match observations in the local universe (see, e.g., Gültekin et al. 2009 and references therein), the situation at $z \sim 3$ is less clear, and it is possible that many massive halos have not yet formed their black holes.

On the other hand, this procedure does allow our calculations to crudely describe the evolution of the He III field with redshift, even though the calculations are all performed at $z = 3$. The primary difference between our density field and one at, say $z = 4$, is the decreased halo abundance in the latter. Assuming that $f_{\mathrm{host}} < 1$ therefore roughly approximates the halo field at this higher redshift (though, of course, it does not properly reproduce their spatial correlations, etc.).

A second problem with our fiducial model is that, by assuming that each halo produces the *same* number of ionizing photons, the resulting black holes will likely not reproduce the well-known M–σ relation between halo and black hole properties (Gültekin et al. 2009). Our choice is motivated by two factors. First, any scatter in the high-redshift black hole mass-halo mass relation (as is likely if these halos are still assembling rapidly) may dominate the steep halo mass distribution. Second, some models predict a characteristic halo mass for quasar activity (Hopkins et al. 2006). In practice, this inconsistency is probably not an enormous problem, because our high mass threshold (and the resulting steep mass function shown in Figure 3.1) means that only a fairly narrow range of halos contribute substantially.

The abundant-source method at least qualitatively reproduces the relation

between halo mass and black hole mass (and the expected ubiquity of quasars), but it leads to some other unexpected features. Most importantly, it demands that the ionized bubbles around many quasars be quite small when $x_{\mathrm{HeIII}} < 1$, as we will show later. Partly, this is because we work at $z = 3$, where the number of massive halos is rather large. At higher redshift, an identical prescription would find fewer sources, which would allow for larger individual bubbles. Moreover, the characteristic luminosity of quasars does not vary dramatically throughout the helium reionization epoch, so we naturally expect that the average bubble size will also remain roughly constant (M09).

Instead, in our calculations within this model, the assumed efficiency parameter ζ varies with x_{HeIII} while the source distribution remains fixed. Thus our sequence of ionized fractions should *not* be viewed as a sequence over time in the abundant-source model, as we do not allow the halo field to evolve. One could view the small sizes of the bubbles when $x_{\mathrm{HeIII}} < 1$ as a result of strong "internal absorption" within the bubbles, which would keep them compact, but that does not seem a likely scenario (Furlanetto & Oh 2008a).

Nevertheless, it is useful to consider a contrasting case from our fiducial model, in which reionization proceeds not by generating more He III regions but by growing those that do exist. Our abundant-source model provides just such a contrast and so is useful as a qualitative guide to the importance of the source prescription.

3.1.3   Ionization Field

With the ionizing source model and the dark matter halo distribution in hand, we determined which areas of our box are fully ionized and which are not. To find the He III field, DexM uses a filtering procedure similar to that outlined

§3.1.1. In particular, He III regions are associated with large-scale overdensities. However, instead of comparing the evolved IGM density to some critical value as in §3.1.1, we consider the density of our sources (or, equivalently, of dark matter halos). In the fiducial model, we let $N_{\text{host}}(\mathbf{x}, R)$ be the total number of halos that have hosted sources inside a region of radius R and mass M centered at a point $\mathbf{x}$. Then, this region is fully ionized if (Furlanetto et al. 2004)

$$\zeta \langle M_h \rangle N_{\text{host}}(\mathbf{x}, R) \geq M(\mathbf{x}, R), \tag{3.2}$$

where $\langle M_h \rangle$ is the average mass of halos containing sources.

First, the source field is smoothed to a lower resolution ($N_{\text{HeIII}} = 500^3$ grid cells) to speed up the ionized bubble search procedure, which takes considerable time at high ionized fractions relative to the other components of the code. We then filter this source field using a real-space, top-hat filter, starting at a (mostly irrelevant) large scale R_{max} and decreasing down to the cell size. Every region satisfying equation (3.2) at each filtering scale is flagged as a He III bubble, regardless of overlap (unlike the halo-finding case). The result is a two-phase map of the ionization field, dependent on the number density of halos hosting ionizing sources.

The assumption of two phases with sharp edges is clearly a simplification. One-dimensional radiative transfer codes show that the "transition region," or distance between fully ionized and singly ionized helium zones, is typically a few Mpc thick – more precisely, the radius over which the He III fraction falls from ~ 0.9 to ~ 0.1 is $\lesssim 20\%$ of the size of the fully ionized zone (F. Davies, private communication; see also Fig. 19 of M09). The relatively late timing of He II reionization, the rarity of the ionizing sources, and the hard spectra of quasars are responsible for widening this region. In many applications, especially

those involving the IGM temperature, this transition region is very important. However, for other applications – such as the He II Lyα forest – the two-phase approximation is adequate, because even a small He II fraction renders a gas parcel nearly opaque. Fortunately, most He III regions are very large (many tens of Mpc across), where many are built through the overlap of bubbles from individual sources, so the relatively narrow transition regions do not dominate the ionization topology. Nevertheless, we must bear in mind this important simplification when applying our semi-numeric simulations to observables.

In the ionization field slices shown in Figure 3.2, we see increasing ionized fraction through a static Universe for the fiducial method. Displayed in the figure are $x_{\mathrm{HeIII}} = 0.20, 0.50, 0.80$, and 0.90, corresponding to $f_{\mathrm{host}} = 0.049, 0.167, 0.400$, and 0.560. The map is fairly bubbly in nature with noticeable clustering. The fact that a pixel residing in a bubble has an increased likelihood of being near another bubble has important consequences for our later calculations. Even at the highest x_{HeIII} displayed, there are large "neutral" sections. Note the periodic boundary conditions.
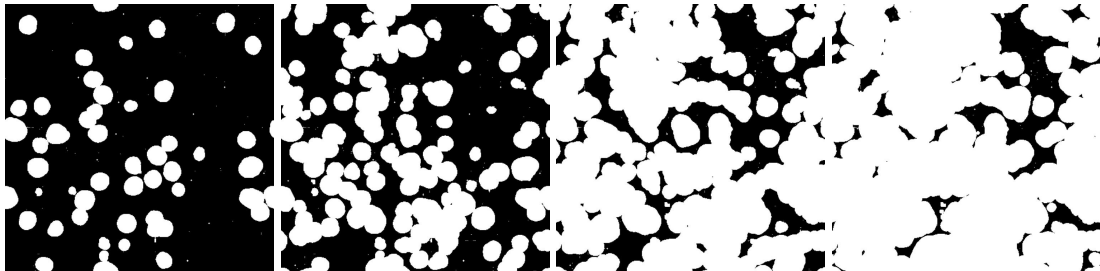
Figure 3.2 Slices from the ionization field at $x_{\mathrm{HeIII}} = 0.20$, 0.50, 0.80, and 0.90 (from left to right) for the fiducial model. All slices are 250 Mpc on a side and 0.5 Mpc deep. White (black) indicates He III (He II) regions.

A similar procedure works for our abundant-source model, except the mass-weighting of the ionization efficiency per halo means that the relevant quantity is the total collapse fraction ($f_{\mathrm{coll}}(\mathbf{x}, R)$). In this case, the ionization criterion

becomes very simple:

$$f_{\text{coll}}(\mathbf{x}, R) \geq \zeta^{-1}. \tag{3.3}$$

As mentioned in the previous section, this model results in small ionized bubbles that increase in size as x_{HeIII} increases, with the highest fractions exhibiting very similar morphology to the fiducial model. Note that most large-scale applications should be fairly insensitive to the presence of small bubbles, since the radiation background is dominated by the brightest quasars within fully ionized regions.
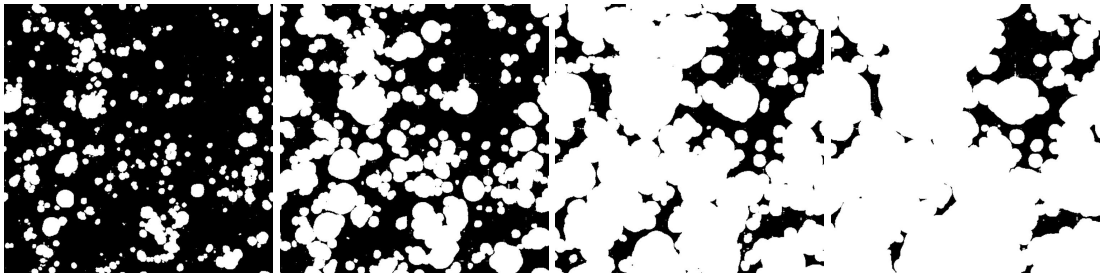
Figure 3.3 Slices from the ionization field at $x_{\text{HeIII}} = 0.21$, 0.50, 0.80, and 0.90 (from left to right) for the abundant-source model. All slices are 250 Mpc on a side and 0.5 Mpc deep. White (black) indicates He III (He II) regions.

Beyond our two main methods, we consider some additional parameter choices, shown in Figure 3.4. In the left three panels, we explore a range of minimum halo mass (effectively changing the quasar lifetime) for the abundant-source method. From left to right, $M_{\text{min}} = (0.5, 5, 10) \times 10^{11} \ M_\odot$ at $x_{\text{HeIII}} \approx 0.80$. As M_{min} is decreased, the number of sources increases, which implies that the quasar is "turned on" for a shorter period of time, ionizing a smaller region given a fixed x_{HeIII}. Similarly, a higher minimum mass means fewer sources and larger, rarer ionized bubbles, which is more pronounced at lower x_{HeIII}. The rightmost panel of Figure 3.4 shows the result for the fiducial method with $f_{\text{host}} = 1$ and $x_{\text{HeIII}} \sim 0.80$. Importantly, the second panel (abundant-source model with $M_{\text{min}} = 5 \times 10^{11} \ M_\odot$) and this panel are very similar visually, indicating the exact ionization criterion

is unimportant.
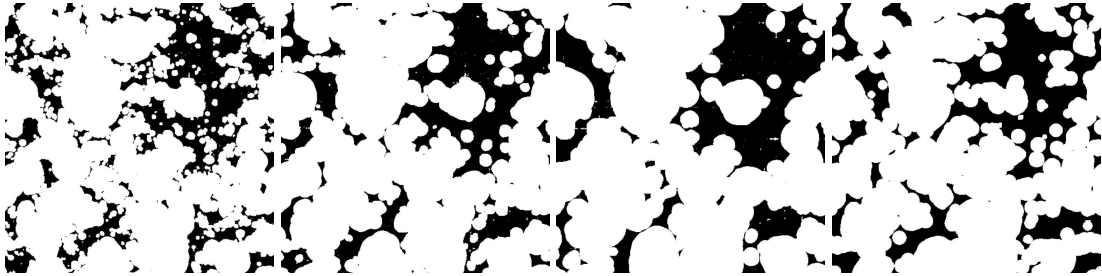
Figure 3.4 Slices from the ionization field for variations on the abundant-source model at $x_{\mathrm{HeIII}} \approx 0.80$. From left to right, $M_{\min} = (0.5, 5, 10) \times 10^{11} \ M_{\odot}$. The rightmost panel shows the fiducial model with $f_{\mathrm{host}} = 1$ at $M_{\min} = 5 \times 10^{11} \ M_{\odot}$.

To quantify the statistical properties of our ionizing field, we calculate the dimensionless ionized power spectrum $\Delta^2_{x_{\mathrm{HeIII}}}(k) = k^3/(2\pi^2 V)\langle |\delta_{x_{\mathrm{HeIII}}}(\mathbf{k})|^2 \rangle_k$, where $\delta_{x_{\mathrm{HeIII}}}(\mathbf{x}) \equiv x_{\mathrm{HeIII}}(\mathbf{x})/\bar{x}_{\mathrm{HeIII}} - 1$. The results for the fiducial model at $x_{\mathrm{HeIII}} = 0.20$, 0.50, 0.80, and 0.90 are shown by the dot-dashed, long-dashed, short-dashed, and solid, respectively, in the left panel of Figure 3.5. These curves are qualitatively similar to M09 results (except for the lowest x_{HeIII}, which we expect to differ the most), with a large-scale peak and small-scale trough. Differences in the underlying quasar models affect the exact position of the peak, but our results are comparable: ~ 30 Mpc scales compared to ~ 60 Mpc in M09. Note that the position of the peaks and troughs do not vary with the He III fraction, which is consistent with M09. Since, in this fiducial model, we are only changing the number of halos that contribute to the ionization at different x_{HeIII}, the size of the ionized bubbles remain constant, leading to the lack of evolution in the peak scale with x_{HeIII}. A similar phenomenon occurs in M09 because the typical luminosity of quasars remains roughly constant with redshift (as does the effective lifetime in their model), so the size of a typical ionized bubble remains the same throughout reionization.

The right panel of Figure 3.5 shows the results for the abundant-source model
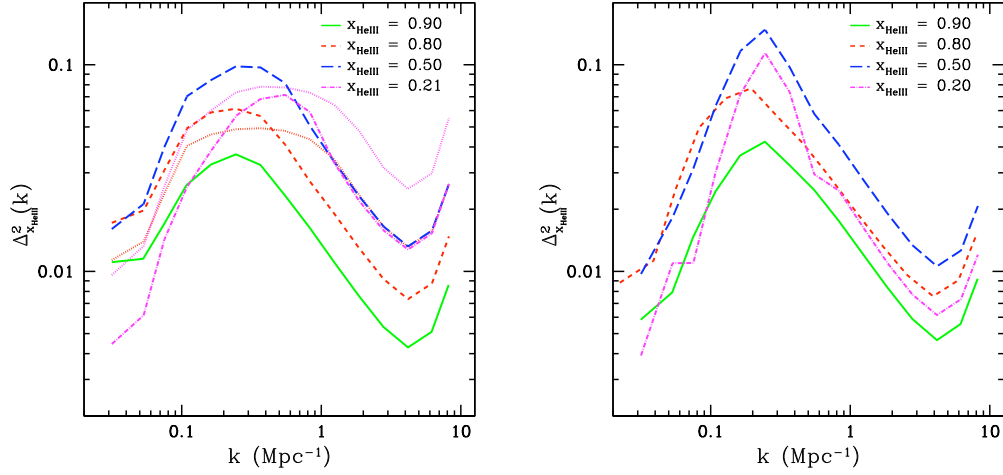
Figure 3.5 The power spectrum of x_{HeIII} at various ionized fractions. *Left panel:* Shown are $x_{HeIII} = 0.20$ (dot-dashed), 0.50 (long-dashed), 0.80 (short-dashed), and 0.90 (solid) for the fiducial model. *Right panel:* The abundant-source method for $x_{HeIII} = 0.21$ (dot-dashed), 0.50 (long-dashed), 0.80 (short-dashed), and 0.90 (solid) is plotted. The dotted lines represent the inclusion of even more sources ($M_{min} = 0.5 \times 10^{11} \ M_{\odot}$) for $x_{HeIII} = 0.50$ and 0.80.

with $x_{HeIII} = 0.21$, 0.50, 0.80, and 0.90 (dot-dashed lines, long-dashed, short-dashed, and solid, respectively). The peaks are wider and evolve to smaller scales as x_{HeIII} decreases, since the lower ionization states are dominated by smaller and smaller bubbles. As expected from the ionization morphologies, the lower x_{HeIII} exhibit the largest differences from the fiducial model. The dotted lines assume the lowest minimum halo mass $M_{min} = 0.5 \times 10^{11} \ M_{\odot}$ at $x_{HeIII} = 0.50$ and 0.80, as shown in the leftmost panel of Figure 3.4. Since each ionized bubble is smaller than the $M_{min} = 5 \times 10^{11} \ M_{\odot}$ case, the peak in the spectrum is shifted to the right and generally smoother. Omitted from this panel, the power spectra of the other variations outlined in Figure 3.4 are nearly indistinguishable.

3.1.4 Density Field

We use the IGM density field not just to find dark matter halos and ionized regions but also to track photon transfer through the IGM. Specifically, when calculating the photoionization rate for He II in the next chapter, we wish to follow the penetration of hard photons into neutral regions. This task requires a reasonably accurate small-scale density field appropriate for baryons. This density field is also crucial to investigating other observable quantities, such as the He II Lyα forest as in Chapter 5. In this section, we describe our procedure for generating that distribution. Figure 3.6 illustrates each step.

As mentioned above, the density field in DexM is generated by evolving an initial, linear density field using first-order perturbation theory to approximate gravitational collapse. This perturbation theory approach underpredicts large overdensities and overpredicts underdensities, as seen in the dotted line of Figure 3.6. Moreover, this density distribution has substantial artifacts, so it is not suitable for later calculations. We therefore smooth the density field by applying a real-space, top-hat filter over 0.75 Mpc (or 1.5 pixel lengths). Strictly speaking, since baryonic physics is not considered, this density field describes dark matter as opposed to gas. Note, however, that the Jeans length in ionized gas at the mean density with an IGM temperature of $\sim 10^4$ K is ~ 1 Mpc (near our smoothing size of 0.75 Mpc), meaning the baryons should trace the dark matter fairly well.

Generally, smoothing the density field reduces both the underdensities and overdensities, as shown in the short-dashed curve of the figure. To create a more realistic density field that matches recent simulations of the gas density distribution, we map our smoothed density field onto the Bolton & Becker (2009, hereafter BB09) distribution, using the respective cumulative probably distri-
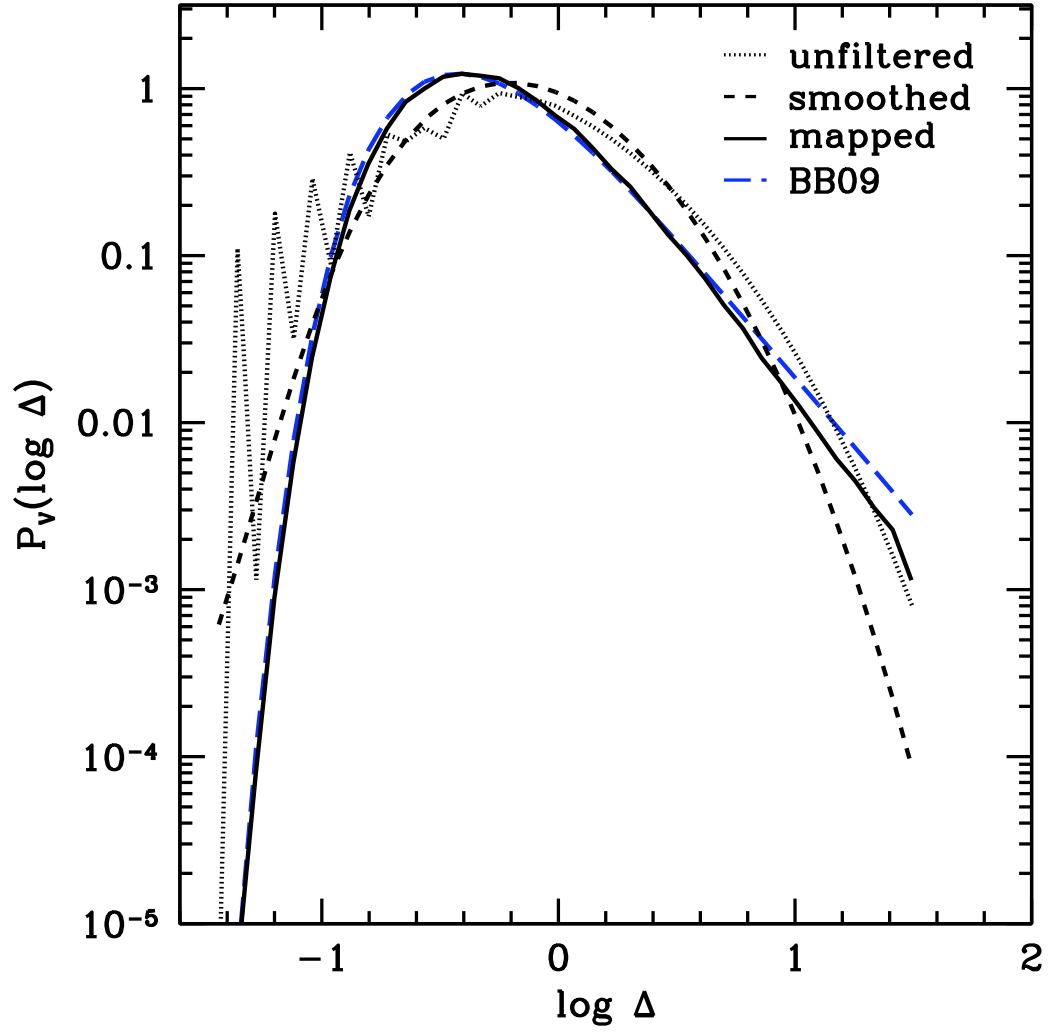
Figure 3.6 The volume-weighted density distribution before, during, and after our mapping procedure with a reference curve. The dotted (short-dashed) line is the evolved (then smoothed) density distribution. The solid line shows the distribution used for subsequent calculations, which is mapped onto the BB09 fit, shown as the long-dashed line.

butions $p_{DF}(< \Delta)$ from our calculation and $p_{BB}(< \Delta)$, the fit from BB09. The long-dashed curve in Figure 3.6 is the BB09 fit. For each cell's overdensity Δ_i, we assign a new overdensity Δ_j such that $p_{DF}(< \Delta_i) = p_{BB}(< \Delta_j)$. In this way, we preserve the ordering of our underlying matter distribution, but we also achieve a result closer to the gas distribution, which is more appropriate for computing observables.

The final, mapped density distribution is the solid curve in the figure. The discreteness visible in the dotted line and a lack of very large overdensities render the matching procedure imperfect. The choice of filter scale has minimal effect on our later calculations. Compared to the smoothed field without mapping, the mapped distribution slightly narrows the photoionization curves in §4.1, since higher density regions effectively absorb more photons.

3.2 Quasar Models

We are interested not only in how the source field affects the morphology of ionized gas but also in how it affects the metagalactic radiation background. This background directly affects the Lyα forest and also indirectly affects several interesting observables, like the temperature of the IGM and ionization states of metal line absorbers. Although obviously intertwined with the determination of the ionization field, we must take an additional step to determine this background, which depends on the *instantaneous* luminosities of the sources. Conversely, the ionization maps depend on the *history* of ionizing photons. We follow an empirical approach to determine the number and intrinsic properties of the "active" quasars, using an observationally determined quasar luminosity function (QLF). Then, we compare three basic models for placing these quasars in dark matter halos.

The Hopkins et al. (2007) QLF, $\Phi(L, z)$, serves as the starting point for all three models. First, we determine the number density of quasars at the redshift in question

$$n_q = \int_{L_{\min}}^{L_{\max}} \Phi(L, z) \, dL, \qquad (3.4)$$

where we take $L_{\min} = 10^{9.36} \, L_\odot$ and $L_{\max} = 10^{17.05} \, L_\odot$ in the B-band (4400 Å). Our conclusions are extremely insensitive to these imposed cuts. At $z = 3$, the comoving quasar density is then $n_q = 2.566 \times 10^{-5}$ Mpc^{-3}. Therefore, 400 quasars (N_q) reside in our volume. This quantity, together with the total number of halos (N_{halo}), f_{host}, and the Hubble time at $z = 3$ imply a quasar lifetime

$$t_{\mathrm{QSO}} = \frac{N_q}{f_{\mathrm{host}} N_{\mathrm{halo}}} \times H^{-1}(z). \qquad (3.5)$$

The t_{QSO} ranges from approximately 1–10 Myr for our suite of models, consistent with recent estimates (e.g., Kirkman & Tytler 2008; Kelly et al. 2010; Furlanetto & Lidz 2011). Note how a smaller f_{host} increases the typical lifetime: if the observed quasars are generated by a smaller set of black holes (because fewer halos host them), each one must live for longer.

We assign each quasar a B-band luminosity L_B, defined as νL_ν evaluated at 4400 Å, randomly sampled from the QLF. Note that since we are concerned with helium-ionizing radiation, this B-band luminosity must be converted to much higher frequencies. We assume a broken power-law spectral energy distribution (Madau et al. 1999):

$$L_\nu \propto \begin{cases} \nu^{-0.3} & 2500 < \lambda < 4600 \text{ Å} \\ \nu^{-0.8} & 1050 < \lambda < 2500 \text{ Å} \\ \nu^{-\alpha} & \lambda < 1050 \text{ Å}. \end{cases} \qquad (3.6)$$

57

A large spread exists in the measured extreme-UV spectral index α values for individual quasars. To replicate the Telfer et al. (2002) distribution for quasars, we model α as a gaussian distribution with mean value $\langle\alpha\rangle = 1.5$ and a variance of unity, constrained by $\alpha \in (0.5, 3.5)$. Each quasar is, therefore, given a random value for α within this distribution.

Now that each quasar has a designated specific luminosity, L_ν (given by L_B and α), the three quasar models differ in the method for placing them inside halos. Note that the two prescriptions for the ionization morphology only determine which host halos have "turned on" by $z = 3$ via f_{host} (and M_{min}), so active quasars are always placed in ionized bubbles.

QSO1: Halos are randomly populated with no preference to host mass. This method is inspired by the Hopkins et al. (2006). In this picture, the distribution of quasar luminosities is due primarily to evolution in the light curve of individual black holes rather than differences in the black holes themselves: as quasar feedback clears out the host halo's gas, less of the light is obscured, rapidly increasing the flux reaching the IGM (Hopkins et al. 2005; Hopkins et al. 2005). This scenario is consistent with quasars residing in halos of a characteristic size; by choosing random halos, we preferentially populate the lowest halo mass, or $5 \times 10^{11}\ M_\odot$.

QSO2: In the second model, we assign the brightest quasars to the most massive halos, which is more consistent with the well-known M–σ relation. Loosely, we are supposing that the luminosity of quasars increases with the halo mass, without fixing the exact form. This picture essentially assumes that the quasar's luminosity is proportional to its black hole's mass, and that the black hole mass increases monotonically with halo mass (see, e.g., Wyithe & Loeb 2002). Any other factors – such as the light curve of each quasar – are subdominant in setting

the relationship.

QSO3: The last model assigns quasars to completely random positions within our box, irrespective of halo positions or ionized regions. This model does not include any clustering and serves mainly as an illustration.

3.3   Comparison with H I Reionization

It is useful to consider the similarities and differences between our work here and similar studies of H I reionization, especially given that we are adapting a hydrogen reionization code. In this section, we will identify the major points of divergence between these two epochs.

Our semi-numeric approach was originally designed for calculations of H I reionization, to which it is undoubtedly better suited. Most importantly, the two-phase approximation (fully ionized or fully neutral) is very accurate for H I reionization, because the soft stellar sources most likely responsible for H I reionization have very short mean free paths ($\lesssim$ a few kpc). The "photon-counting" arguments inherent to the method are therefore almost exactly accurate for that case, whereas the transition region between He II and He III fills a non-negligible fraction of the volume. Our ionization maps must therefore be taken as approximate, although they are still useful for many purposes (such as calculations of the He II Lyα optical depth, which is nearly opaque even in the transition region).

Another key difference between the ionization fields in H I and He II reionization is the source abundance. We typically assume that any dark matter halo able to form stars will also produce ionizing photons during the earlier era, making those sources many times more common than luminous quasar hosts at $z \sim 3$. During H I reionization, ionized bubbles typically have thousands of sources even

early in the process (Furlanetto et al. 2004), but we have found that, for He II reionization, even a single source can generate a large bubble. The "morphology" of reionization (i.e., the distribution of ionized bubble sizes) is often taken as a key observable of the H I process, because the huge number of sources closely connects it to the underlying dark matter field. In the He II case, however, the small numbers of sources make that connection mostly uninteresting: Poisson fluctuations instead play a key role (Furlanetto & Oh 2008a), and the distribution of bubbles relative to halos is much more likely to tell us about the details of the black hole-host relation than it is the fundamentals of the reionization process. Quantitatively, there is little evolution in the shape of the power spectrum of the ionized fraction throughout helium reionization.

Additionally, because there are so many sources inside each H II region, the ionizing background remains large at all times, preventing these bubbles from recombining substantially. When only one or two (short-lived) sources occupy each bubble, however, recombinations can substantially increase the He II fraction inside even regions that are nominally fully ionized (Furlanetto et al. 2008). Fortunately, we will show in the next chapter (see Figure 4.4) that most such regions will be illuminated, at least late in the process. But this will, for example, increase the opacity of some He III bubbles in the Lyα forest (and to ionizing photons). We have crudely modeled this effect through our source prescriptions (one can regard turning some halos "off" as instead allowing their ionized bubbles to recombine fully).

Our approach to describing the ionizing sources themselves is also rather different. The lack of data on high-redshift galaxies so far implies that naive prescriptions (with a constant ionizing efficiency per halo, or at most a systematic variation with halo mass) are more than adequate. On the other hand, the tight

observational constraints on the quasar luminosity function at $z \sim 3$ require that it be directly incorporated into the calculation. Including the QLF is easy to do for the instantaneous ionization rate but much harder for the cumulative number of ionizing photons, because the relationship between the visible sources and their dark matter halo hosts and the light curves of individual quasars remain uncertain. We will show in subsequent chapters that the details of this association do not strongly affect many properties of reionization (such as the distribution of Γ), but they will show up in other observables. For example, one could imagine searching for massive halos inside of large He III regions in order to identify the descendants of bright quasar hosts.

A final key difference is the source spectrum, which is unimportant for stellar sources but crucial for the quasars responsible for He II reionization. Although we have ignored the resulting partially ionized transition zones, we have included these spectra explicitly in evaluating the ionizing background. We are thus able to track the growth of a hard background in He II regions, an effect likely to be much less important during H I reionization (Mesinger & Furlanetto 2009).

3.4 Discussion

We have introduced a novel, semi-numeric method for efficiently generating dark matter halo distributions and ionization maps relevant to the full reionization of helium. Specifically, we adapted an existing hydrogen reionization code (DexM) to identify halos at lower redshift and changed the method for determining the ionization state to suit quasars as sources. The speed of our algorithm allows exploration of a wide range of possible quasar models not only for active quasars, but in the realization of the ionization map as well.

Our results broadly match previous simulations of related quantities, at least statistically speaking. We generated accurate halo mass functions as compared to N-body simulations. This congruence is important for determining the effect of quasar clustering. We also reproduced the He III morphology, especially at high x_{HeIII}, as demonstrated by the ionized power spectra, which compare favorably with M09 (modulo our different source prescriptions). We demonstrated that this method can easily produce simulation volumes hundreds of Mpc across to accurately capture the large-scale features of helium reionization. We also constructed a density field that matches (by design) the smoothed particle hydrodynamics simulations of BB09. A realistic density field is crucial to capturing at least some of the small-scale fluctuations in the observable quantities, which is lacking in semi-analytic models.

There are some important caveats to our methods:

(1) We assume a two-phase medium. In principle, our ionized bubble edges should not be abrupt, especially since helium recombines so quickly, but instead, transition smoothly from fully ionized to singly ionized. This effect is less important during the late stages of reionization as the bubbles increasingly overlap (so that the ratio of their volume to their surface area decreases).

(2) We do not fully account for recombinations. In particular, we do not compensate for ionizing photons being "wasted" on reionizing this gas when generating our ionization maps. This effect is less important during the late stages of reionization, as each ionized bubble will multiple and sequential sources.

(3) Our simulations assume that quasars emit radiation isotropically. Many theoretical models pertaining to quasar behavior predict otherwise. Although this effect is important during the early stages of reionization, once each ionized bubble contains (or has contained) multiple, randomly oriented quasars, beaming

is no longer important.

CHAPTER 4

Fluctuations in the Helium-Ionizing Background

Recent theoretical and observational studies have demonstrated that the high-energy radiation background fluctuates strongly both during and after helium reionization, due largely to the rarity of the bright quasars providing the ionizing photons (see Fardal et al. 1998; Maselli & Ferrara 2005; Bolton et al. 2006; Meiksin 2009; Tittley & Meiksin 2007; Furlanetto 2009a for theoretical work and Shull et al. 2004; Fechner et al. 2006; Fechner & Reimers 2007; Shull et al. 2010; Worseck et al. 2011 for observations). As a first application of our method developed in the previous chapter, we wish to quantify the expected variations in the helium-ionizing background. Crucially, we include a realistic quasar population and local density information, capturing both large- and small-scale fluctuations. We examine both the post-reionization limit and the behavior during reionization §4.1. By spanning our parameter space, we determine which model inputs are most important. We conclude in §4.2.

4.1 Photoionization Rate

With the quasar configuration, ionization map, and density distribution, we can calculate the He II photoionization rate Γ at any point in our box, even during reionization. Although the mean rate $\langle \Gamma \rangle$ determines the average behavior of many observable quantities, we are particularly interested in the magnitude of

fluctuations about this mean, which have important effects for scatter in observables and even for the evolution of the mean (Davies & Furlanetto 2012). In brief, we add up the contribution to Γ from all sources within our box, taking into account the local density and the ionization state.

4.1.1 Post-Reionization

First, we will examine the post-reionization regime, where the ionization maps are immaterial, and the variations in Γ only depend on the distribution and intrinsic qualities of the active quasars. The specific intensity at a given frequency (in units of ergs/s/cm^2/Hz/sr) is

$$J_\nu \quad = \quad \sum_i \frac{L_{\nu,i}}{(4\pi r_i)^2} e^{-r_i/\lambda_{\mathrm{mfp}}}, \tag{4.1}$$

where $L_{\nu,i}$ is the ith quasar's specific luminosity (converted using our assumed spectrum and including the dispersion in α), r_i is the distance between this quasar and the point of interest, and λ_{mfp} is the mean free path of the ionizing photons. Put simply, we add up the contribution of each quasar to the specific intensity at the point of interest.

The mean free path is both uncertain and varies rapidly over the era of interest, with values ranging from 15 to 150 Mpc at the ionization edge. We choose a fiducial value at this edge, $\lambda_0 = 60$ Mpc, to match more detailed calculations of λ_{mfp} that are consistent with recent calculations incorporating more sophisticated treatments of the Lyα forest (Davies & Furlanetto 2012). However, it is worth noting that the mean free path varies quite rapidly with redshift over the $z \approx 2.5$–3.5 range and is subject to substantial uncertainties in the source population. We allow a range of $\lambda_0 = 15, 35, 60, 80$ Mpc in this work to evaluate

the impact.

At higher frequencies, we fix the comoving mean free path as a power law in frequency,

$$\lambda_{\mathrm{mfp}} = \lambda_0 \left(\frac{\nu}{\nu_{\mathrm{HeII}}} \right)^{1.5}, \tag{4.2}$$

where ν_{HeII} is the frequency corresponding to the ionization edge of He II. In a simple toy model for which the distribution of He II absorbers $f(N_{\mathrm{HeII}}) \propto N_{\mathrm{HeII}}^{-\beta}$, we would have $\lambda_{\mathrm{mfp}} \propto \nu^{3(\beta-1)}$ (Faucher-Giguère et al. 2009). Within the context of such a model, our slope corresponds to $\beta = 1.5$, which is close to the canonical value for H I absorbers (Petitjean et al. 1993; Kim et al. 2002). Recent work shows that the H I Lyα forest column density distribution may be much more complex than such a toy model (Rudie et al. 2012; O'Meara et al. 2012; Prochaska et al. 2010), but detailed calculations of the ionizing background show that this frequency dependence is nevertheless accurate, at least relatively close to the ionization threshold (Davies & Furlanetto 2012). We also explore a model in which the mean free path remains constant with frequency.

In detail, our assumption of a spatially constant mean free path is incorrect: since the ionization structure of the IGM absorbers is set by the (fluctuating) metagalactic radiation field, the amount of absorption – and hence the mean free path – fluctuates as well. We ignore this possibility here, but it has been approximately included in analytic models (Davies & Furlanetto 2012).

The photoionization rate follows simply from J_ν:

$$\Gamma = 4\pi \int_{\nu_{\mathrm{min}}}^{\infty} d\nu \frac{J_\nu}{h\nu} \sigma_{\mathrm{HeII}}(\nu), \tag{4.3}$$

where h is Planck's constant and $\sigma_{\mathrm{HeII}}(\nu) = \sigma_0 (\nu/\nu_{\mathrm{HeII}})^{-3}$ ($\sigma_0 = 1.91 \times 10^{-18}$ cm^2) is an approximation to the photoionization cross-section. In the post-reionization

case, $\nu_{\min}$ is merely the photon frequency required to fully ionize helium. The probability distribution of Γ is shown in the left panel of Figure 4.1, scaled to the average value for each scenario in a post-reionization universe. The difference between the three quasar models (*QSO1* black, *QSO2* blue, and *QSO3* red) is fairly negligible in this regime.

Since the results for *QSO1* and *QSO3* are nearly identical, randomly placing quasars approximates quasars populating random halos, demonstrating that clustering of sources is unimportant. Predictably, the *QSO2* result is wider, since clustering is more pronounced in this scenario. The largest dark matter halos tend to be found near other large dark matter halos, so the brightest quasars will tend to cluster. As noted in Furlanetto (2009a), these brightest quasars dominate the distribution. The $\langle \Gamma \rangle$ are identical to within a few percent for the three quasar models.

The left panel of Figure 4.1 also compares frequency-dependent (solid) and frequency-independent (dashed) attenuation lengths. The differences between quasar models are similar in both cases, but the curves are generally wider for a frequency-independent value. Photons at the highest energies can travel farther in the frequency-varying model providing a higher minimum ionizing background, although the difference is small in the post-reionization regime. Along similar lines, the right panel of Figure 4.1 shows the impact of varying the mean free path normalization with $\lambda_0 = 15$, 35, 60, and 80 Mpc (widest to thinnest curves). As before, larger mean free paths narrow the distribution. The larger λ_0 results are very similar, indicating that the quasars dominating the distribution are within ~ 60 Mpc of each other; beyond that point, the intrinsic spread in luminosities dominates the distribution.

The analytic model of Furlanetto (2009a), based on Poisson distributed sources
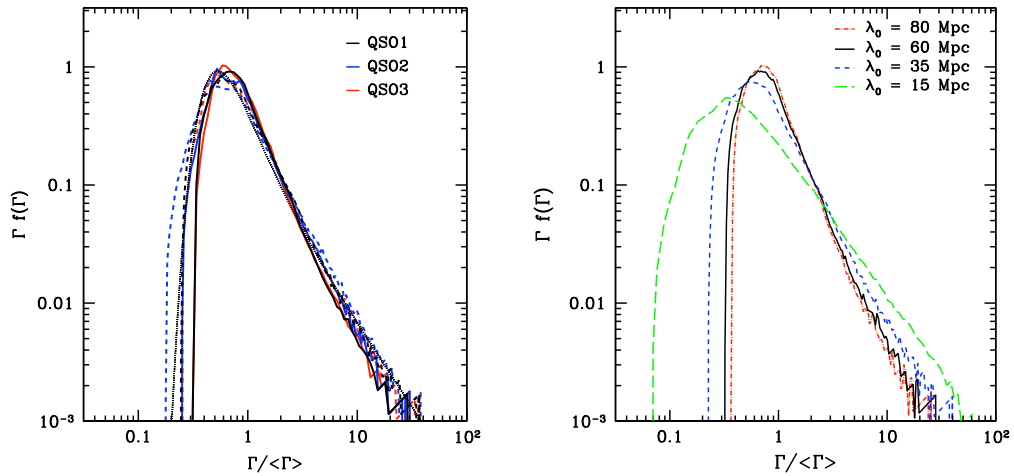
Figure 4.1 Distribution of Γ (scaled to the mean) in the post-ionization regime. *Left panel:* Three models are shown: quasars placed in random halos (black), most luminous quasars situated in most massive halos (blue), and quasars placed randomly throughout the box (red). The dashed curves result from a fixed attenuation length, $\lambda_{\mathrm{mfp}} = 60$ Mpc. The post-reionization analytic result is represented by the dotted line. *Right panel:* From widest to narrowest curves, $\lambda_0 = 15$, 35, 60, and 80 Mpc.

($\lambda_{\mathrm{mfp}} = 60$ Mpc) and represented by the dotted line, is remarkably close to the semi-numeric result. Since it does not include frequency dependence in λ_{mfp}, the analytic result unsurprisingly matches the fixed λ_{mfp} model best. The congruence of the analytic and semi-numeric distributions further indicates that the rarity of quasars dominates the distribution of the photoionization rate, not clustering.

Even in this post-reionization regime, Γ varies substantially about the mean, with very little dependence on the underlying details. The width of this distribution is essentially set by the QLF (constant for all models in this work) and the attenuation length, where smaller values broaden the curve. In all cases, the high-Γ tail is especially robust. This segment of the distribution corresponds to regions near bright sources, or proximity zones, so model details, like the attenuation length or exact quasar placement, are inconsequential.

4.1.2 During Reionization

Next, we approximate the evolution of Γ during reionization (by varying x_{HeIII}). High-energy photons can propagate through the He II regions present in this era, because the optical depth experienced by photons decreases with frequency. Unlike previous analytic models, we can explicitly compute the ionizing background generated by these high-energy photons. In particular, with our density field and ionization map, we estimate the He II column density N_{HeII} for a given photon ray and, thereby, estimate the absorption.

Suppose we wish to calculate Γ at a particular point $\mathbf{r}$. Beginning there, we take a step of length $dx_p = \frac{1}{2}\Delta x_p$, where Δx_p is the proper width of a pixel in our simulation. If the pixel contains He II, the step's contribution to the intervening column density is $\Delta N_{\mathrm{HeII}} = \Delta \times n_{\mathrm{He}} \times dx_p$, where $\Delta = \rho/\bar{\rho}$ is the pixel's overdensity and n_{He} is the (proper) number density of helium atoms. Otherwise,

there is no contribution to N_{HeII}. If the ionization state changes during a step, we use the x_{HeIII} present at the midpoint for the entire segment.

Given this column density, we can estimate the minimum photon frequency for light from a particular quasar i to reach our point, $\nu^i_{\min}$, using the opacity condition $\sigma_{\mathrm{HeII}}(\nu^i_{\min})N^i_{\mathrm{HeII}} = 1$, where N^i_{HeII} is the total column density between the point and the quasar. Then, we demand

$$\nu^i_{\min} = (\sigma_0 N^i_{\mathrm{HeII}} \nu^3_{\mathrm{HeII}})^{1/3}. \tag{4.4}$$

Of course, we require that $\nu_{\min} \geq \nu_{\mathrm{HeII}}$, irrespective of this equation. We then use this threshold frequency in equation (4.3) to calculate the total ionizing background, Γ. In this way, we approximate the opacity due the He II regions in a local, density-dependent manner.

Figure 4.2 displays the distribution of Γ for several x_{HeIII}. In the left panel, *QSO1* (solid) and *QSO2* (dashed) for the fiducial model are shown for $x_{\mathrm{HeIII}} = 0.20, 0.50, 0.80, 0.90$ and post-reionization (from widest to thinnest, respectively). A bimodal distribution develops at small ionized fractions due to the low-level background from hard photons escaping into the He II regions. Because He II reionization causes substantial IGM heating, whose amplitude is determined by the shape of the local ionizing background, this bimodality may have important consequences for this heating process (M09, Furlanetto & Oh 2008a; Bolton et al. 2009). Even with $x_{\mathrm{HeIII}} = 0.9$, this hard background is still substantial. Interestingly, Mesinger & Furlanetto (2009) calculated the UV background using DexM during the H I reionization era. At that time, the background does not exhibit this behavior. This difference is due to our inclusion of hard photons, which are more important for helium reionization (as the H I ionizing sources are expected to have had very soft spectra).
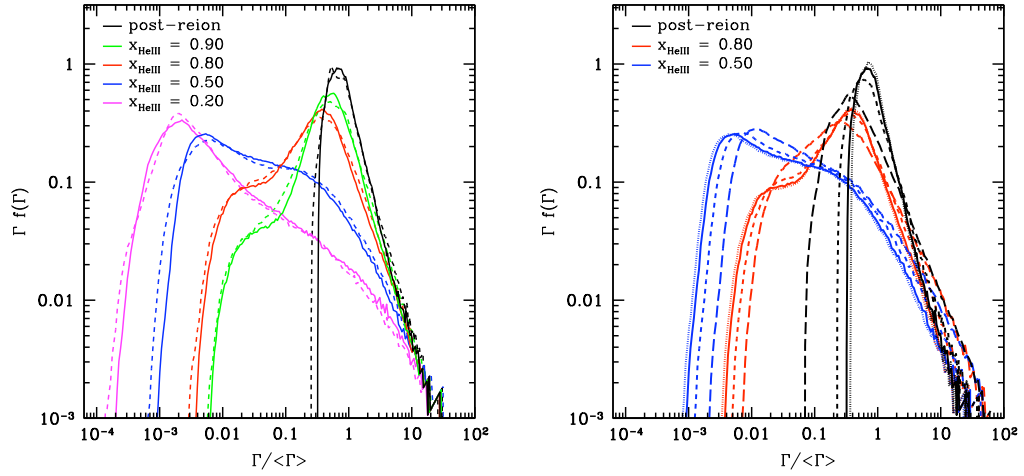
Figure 4.2 Distribution of Γ (scaled to the mean fiducial value post-reionization) for several x_{HeIII} and varying λ_0. *Left panel:* From lowest to highest at $\langle \Gamma \rangle$, $x_{\mathrm{HeIII}} = 0.20,\ 0.50,\ 0.80,\ 0.90$ and post-reionization are shown for the fiducial model (solid) and *QSO2* variation (dashed). *Right panel:* The fiducial model for $x_{\mathrm{HeIII}} = 0.50,\ 0.80$, and post-reionization is displayed with varied mean free path normalizations, $\lambda_0 = 15,\ 35,\ 60$, and 80 Mpc as long-dashed, short-dashed, solid, and dotted, respectively. Note that $\lambda_0 = 60$ Mpc (solid) is the fiducial value.

The choice of quasar model has only a minimal impact on the distributions, but it preferentially affects the high-end tail, which becomes increasingly important as x_{HeIII} decreases. Put another way, the high-Γ peak is shifted to the right for *QSO2* for $x_{\mathrm{HeIII}} < 1$, while the low-Γ peak is unaffected. Since *QSO2* clusters more bright sources together, this shift indicates that proximity to quasars trumps the radiation from more distant sources. This behavior implies that detailed observations of He II Lyα absorption inside of large ionized bubbles *during* reionization may help determine how quasars are distributed inside of dark matter halos.

The right panel of Figure 4.2 illustrates the effect of changing λ_0 on the distribution of Γ, where $\lambda_0 = 15, 35, 60,$ and 80 Mpc as long-dashed, short-dashed, solid, and dotted, respectively, for $x_{\mathrm{HeIII}} = 0.50, 0.80,$ and post-reionization. Note that the distribution is scaled to the post-reionization $\langle\Gamma\rangle$ for each λ_0. In the post-reionization regime, the general trend is that larger mean free paths translate into narrower distributions, as previously demonstrated. Similarly to post-reionization, the high-Γ tail is steeper for larger λ_0 during reionization. In contrast, the low-Γ peak does not shift to lower values for smaller λ_0, nor do the curves become significantly narrower. Since more photons can penetrate the He II regions with larger mean free paths, the $\langle\Gamma\rangle$ of these regions (a proxy for the low-Γ peak) is higher. To roughly summarize, the low peak and steepness of the high-Γ tail are determined by how far photons can travel, and the high peak is shaped by the position of quasars.

The left panel of Figure 4.3 contrasts the abundant-source and fiducial methods. Here, $x_{\mathrm{HeIII}} = 0.21, 0.50, 0.80, 0.90,$ and post-reionization (from widest to thinnest curves) with *QSO1* (solid) and *QSO2* (short-dashed). In the abundant-source case, the difference between *QSO1* and *QSO2* is even less pronounced than

in the fiducial framework. With smaller ionized bubbles, fewer pixels reside in an ionized region with an active quasar, except when overlap dominates (higher x_{HeIII}). Comparing the fiducial method with *QSO1* (long-dashed curves), the abundant-source model are very similar for higher x_{HeIII}. For the lowest ionization fraction, the high-Γ tail is substantially higher in the fiducial model, but the low-Γ peak remains quite similar. The decrease at high intensities occurs for two reasons. First, the abundant-source method enforces smaller ionized bubbles, so the proximity zones are smaller and less space is filled by the near regions (outside the He III region, of course, the opacity rapidly increases). Second, the abundant-source method has many more empty He III regions – that is, regions that have been ionized in the past but no longer host an active source. Because more of the IGM is inside of isolated bubbles, there is less chance for a nearby quasar to illuminate such a region. Overall, the difference between the two methods is surprisingly small, especially during the late stages of reionization.

The right panel of Figure 4.3 shows the impact of including more sources via the minimum halo mass $M_{\mathrm{min}} = (0.5, 5, 10) \times 10^{11} \ M_{\odot}$ as the short-dashed, solid, and long-dashed curves, respectively. Note that these are variations on the abundant-source model, where the representative ionization map slices are shown in Figure 3.4. The widest to thinnest curves are $x_{\mathrm{HeIII}} = 0.5$, 0.8, and post-reionization. In the post-reionization regime, the results are nearly identical, meaning the exact placement of active quasars is relatively unimportant. With smaller ionized bubbles (i.e., lower M_{min}), the distributions are shifted toward lower Γ. Decreasing M_{min} reduces source clustering. Essentially, fewer regions are within an ionized bubble *and* close to a quasar.

Figures 4.2 and 4.3 span a wide range of quasar model possibilities. Importantly, the density distribution (as noted in §3.1.4), the exact ionization map, and
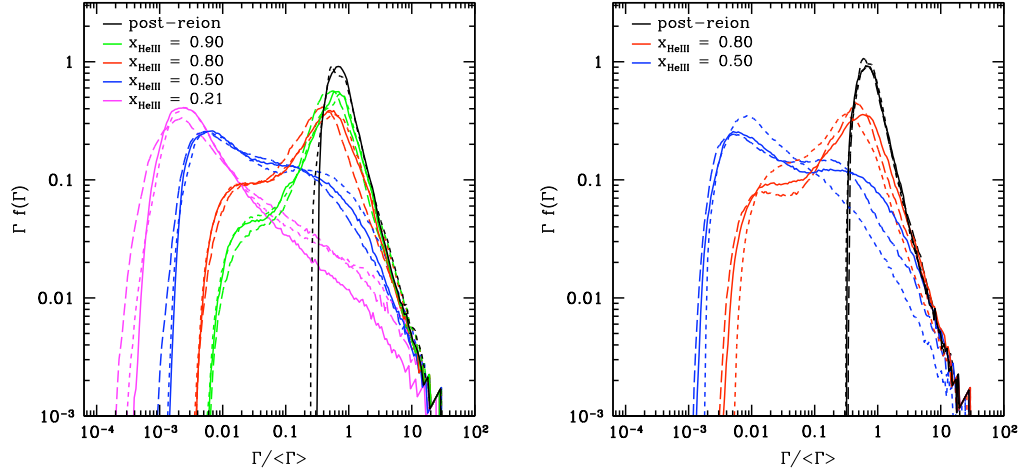
Figure 4.3 Distribution of Γ (scaled to the mean value post-reionization) for the abundant-source method. *Left panel:* From lowest to highest at $\langle\Gamma\rangle$, $x_{\mathrm{HeIII}} = 0.21$, 0.50, 0.80, 0.90, and post-reionization, where *QSO1* (solid) and *QSO2* (short-dashed). For comparison, the long-dashed curves are the fiducial model with *QSO1*. *Right panel:* Here, the minimum halo mass is varied with *QSO1*, and $M_{\mathrm{min}} = (0.5, 5, 10) \times 10^{11}\ M_\odot$ are the short-dashed, solid, and long-dashed curves, respectively. For clarity, only $x_{\mathrm{HeIII}} = 0.50$, 0.80, and post-reionization (from widest to narrowest) are shown.

even the basic quasar model do not greatly affect the photoionization rate distributions. Not only does this minimize the dependence on our fiducial choices, it emphasizes the robustness of our general conclusions and the relative importance of uncertain quantities relating to quasars.

To tease out the cause of the bimodal nature of Γ, we contrast the distribution of Γ inside fully ionized bubbles with that outside them in Figure 4.4 (short and long-dashed curves, respectively). As expected, ionized areas around active quasars contain the highest Γ. The origin of the small-Γ distribution is less straightforward. The ionizing radiation that penetrates the singly ionized helium comprises the majority of this low-end segment. This radiation is mainly due to high-frequency photons that can travel longer distances before absorption. Ionized bubbles that do not host *active* quasars also make up a non-negligible fraction of this low-Γ tail (and especially in the transition region from one peak to the other). This contribution is more relevant early in reionization (when overlap of the bubbles is less significant, meaning neighboring sources cannot illuminate such empty regions). We caution the reader that such empty regions are unlikely to be fully ionized, since the recombination time is relatively short (Furlanetto et al. 2008). Therefore, we likely overestimate the ionizing background here.

Furlanetto (2009a) explores the related $f(J)$ through a combination of analytic calculations and a Monte Carlo model for the number of sources within a distribution of bubble sizes (see Figure 2.1 based on this model). The results during reionization show large fluctuations, but do not exhibit the bimodal behavior found in this work. The difference is due to our inclusion of local density effects and the improved treatment of hard photons via ν_{min} and a frequency-dependent mean free path.
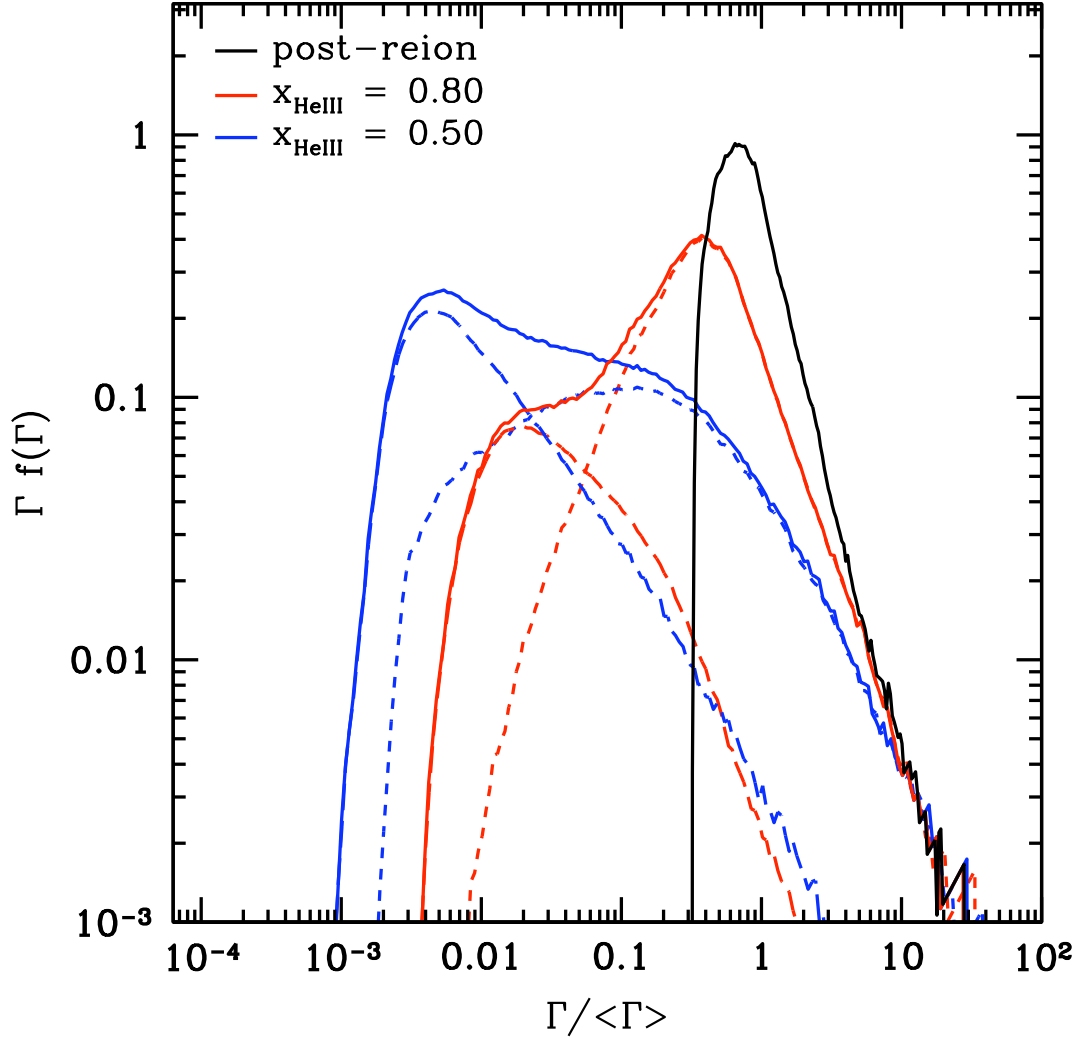
Figure 4.4 The distribution of Γ within and without ionized regions. The solid, short-dashed, and long-dashed lines are the distributions of the entire box, He III regions, and He II regions, respectively. The widest to thinnest curves are $x_{\mathrm{HeIII}} = 0.50$, 0.80, and post-reionization. The high-end Γ is determined almost exclusively by regions around quasars, which are necessarily inside ionized bubbles. The ionizing photons that escape the He III dominate the low-end Γ, although ionized bubbles without an enclosed source also contribute.

4.2 Discussion

We have presented the first systematic study of fluctuations in the ionizing background during reionization. Our $f(\Gamma)$ exhibit significant variation even post-reionization, in excellent agreement with analytic calculations (Furlanetto 2009a). Furthermore, we calculate the more relevant $f(\Gamma)$ as opposed to $f(J)$ in the analytic case. We demonstrated that complications like a frequency-dependent mean free path and quasar clustering do not significantly affect the result in this regime.

We also find that a broader and bimodal distribution develops during reionization. This distribution differs from that during the hydrogen reionization era (Mesinger & Furlanetto 2009) and from analytic predictions for the He III era (Furlanetto 2009a). These fluctuations have important consequences, which we can quantify, for many observables, including the quasar spectra metal lines and IGM heating. In the next chapter, we will study the impact of these fluctuations on the He II Lyα forest. The most important conclusion is that not every part of the IGM experienced the same reionization history or receives the same background radiation.

We included a frequency-varying mean free path, another crucial improvement on semi-analytic models. This frequency-dependent spectrum gives rise to the bimodal nature of $f(\Gamma)$ we find during reionization. Specifically, hard photons can travel farther and escape into the He II regions, creating a low-level background there. This frequency-dependence is important for studies of the He II Lyα forest, metal lines, and IGM heating. This assumption ignores an detailed radiative transfer effects and is important both during and after reionization. In particular, we *prescribe* the normalization of this mean free path, rather than allowing it to vary with the local radiation field (Davies & Furlanetto 2012).

Our conclusions are mostly insensitive to our underlying assumptions for active quasars and ionizing sources. For our wide range of explored models, the resultant $f(\Gamma)$ varied minimally, except for possibly λ_0. In particular, quasar clustering is a secondary effect, and a few rare, bright quasars dominate the spectrum. Although this makes our predictions robust, distinguishing between our models using observational data dependent on the ionizing background would be difficult if not impossible.

CHAPTER 5

Fluctuations in the He II Lyα Forest

We continue applying our models outlined in Chapter 3 to potentially observable quantities. Here, we study the variability in the He II Lyα forest data and its consequences for reionization. In the previous chapter, we examined the distribution of ionizing background intensities in the post-reionization limit (see also Zuo 1992; Meiksin & White 2003; Meiksin 2009; Furlanetto 2009b). This model (and others) predicts substantial line-of-sight variations in the He II photoionization rate Γ even on large scales. To measure the state of the IGM (as opposed to probing individual absorbers), He II Lyα opacity measurements are averaged over tens of Mpc. These observations have important features not captured by a flux distribution or power spectrum of ionizing intensity : (1) real quasar absorption spectra allow only a finite dynamic range to measure transmission, (2) observations are binned with sharp filters in real space, and (3) observations are sensitive to the *local* density field and temperature of the IGM in addition to the radiation background.

We explore many of the same quantities, including Γ fluctuations along lines of sight and the probability distribution of the He II effective optical depth during and after reionization, presented in Furlanetto & Dixon (2010). In their paper, a simple Monte Carlo model for the quasar distribution (also based on Hopkins et al. 2007) generated the radiation field. To approximate the effective optical

depth,

$$\tau_{\mathrm{eff}} \propto \left(\frac{\langle \Gamma \rangle}{\Gamma} \right)^{\beta - 1} , \tag{5.1}$$

where $\langle \Gamma \rangle$ is the mean He II photoionization rate and $\beta = 1.5$ for the He II column density distribution $\propto N_{\mathrm{HI}}^{-\beta}$ (Fardal et al. 1998, and references therein). To mimic reionization, the fraction x_{dark} of pixels that are opaque to ionizing photons was fixed, chosen to correspond to the smallest Γ in the post-reionization limit. In other words, for $x_{\mathrm{dark}} = 0.20$, the 20% of pixels with the lowest radiation background were set to $\Gamma = 0$. Note that x_{dark} is not x_{HeII}, since some regions will remain ionized from previous generations of quasars.

Furlanetto & Dixon (2010) found fluctuations in the effective optical depth of order its mean value in the post-reionization regime, with increasing x_{dark} widening the distribution. A high-τ tail also developed during reionization. The observed τ_{eff} in many sightlines that were detailed in Chapter 2 were found to be too high to be accommodated by a smoothly evolving opacity in a post-reionization universe, leading to the conclusion that helium reionization ended $z \lesssim 2.9$. Not only do we have improved and expanded data, but we follow a more sophisticated model. Importantly even post-reionization, we directly include an inhomogeneous density field and allow the mean free path to vary with frequency. Furthermore, our active quasar and ionizing source models provide more realistic source geometries and ionization maps.

For this chapter, we rely on the methods presented in Chapters 3 and 4. To address variations along a line of sight, we start with our 250 Mpc³ box, where each pixel contains the local density, ionization state, and photoionization rate information, that includes a realistic population of quasars. (Note that all distances are comoving unless otherwise stated.) To ensure that our segments can stretch for many hundreds of Mpc, we enforce periodic boundary conditions,

essentially tiling nine boxes together. Each quasar contributes only once – and with the shortest distance – to Γ at each point along a segment[1]. We compute the ionizing intensity along 800 lines of sight 400 Mpc in length, keeping track of the density at each pixel-sized step (0.5 Mpc). Each skewer originates at an "active" quasar, and we exclude the first 50 Mpc to remove most of the "proximity" zone, where the source quasar radiation dominates the background. We then use this information to calculate τ_{eff} along these skewers. Throughout this chapter, we follow the fiducial ionizing-source method with the *QSO1* active quasar model, with exceptions and comparisons when noted.

5.1 Post-Reionization Limit

5.1.1 The He II Photoionization Rate

Although we already know the mean He II photoionization rate $\langle \Gamma \rangle$ and the magnitude of fluctuations about this mean, we are interested in behavior along typical lines of sight. In this way, we can look for common features and the spatial extent of the fluctuations. For these calculations, we choose a fiducial value $\lambda_0 = 35$ Mpc and allow a range of normalizations for the λ_{mfp} (see equation 4.2). We choose a smaller mean free path normalization (as compared to $\lambda_0 = 60$ Mpc in the previous chapter) to strengthen our conclusions in §5.3: a smaller mean free path increases the fluctuations, making extreme measurements of the optical depth more likely.

The lower section of the left panel of Figure 5.1 shows Γ scaled to its mean value $\langle \Gamma \rangle$, calculated at $dr = 0.5$ Mpc intervals, along three sample lines of

---

[1]In detail, we use the closest position of each quasar in a periodic tiling of the box, so that we effectively include all sources within 250 Mpc of every point. This scale is much larger than the assumed attenuation length, so more distant sources can safely be ignored.

sight. These examples illustrate several important aspects of the signal (see also Furlanetto 2009b; Furlanetto & Dixon 2010): (1) the correlations can extend over extremely large scales, as in the long trough at ~ 200–350 Mpc in the dashed curve; (2) rare, small-scale "fluctuations" are present, because of the $1/r^2$ profiles around individual sources; (3) the median of Γ is a few times smaller than the mean; and (4) fluctuations far above the median level are relatively common, but the ionization rate never falls significantly below that level. This floor is due to the accumulated contributions of the many quasars at distances larger than λ_{mfp}, a crucial point for the later results.
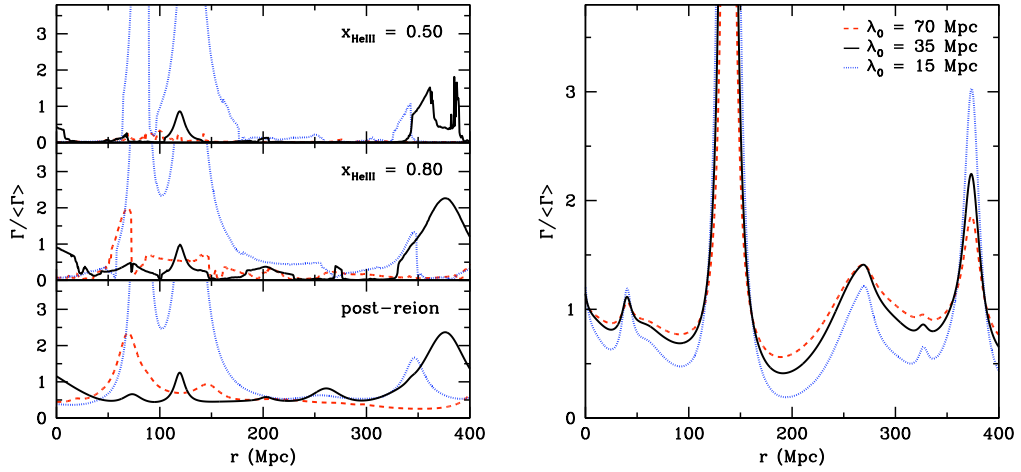
Figure 5.1 *Left panel:* The photoionization rate, relative to the mean, is plotted along the same three sample lines of sight for $x_{\mathrm{HeIII}} = 1$ (lower), 0.80 (middle), and 0.50 (upper). Note the Γ floor present in the post-reionization case and the presence of both large- and small-scale features. Large, "dark" segments appear by 80% ionized. *Right panel:* In the post-reionization regime, Γ along a single line of sight with $\lambda_0 = 15, 35$, and 70 Mpc (dotted, solid, and dashed, respectively). Note that each curve is scaled to its mean individually. The differences are even less pronounced with lower ionization states, which are not shown.

In this figure, we also see the some of the effects of quasar clustering. In the line of sight represented by the dotted curve, two bright quasars are close together, producing a large double peak. Although not many lines of sight contain these

pairs, these rare regions are very illuminated and contribute significantly to the overall $\langle \Gamma \rangle$. Observationally, disentangling these pairs could be difficult.

The right panel of Figure 5.1 shows the effect of changing the mean free path, where $\lambda_0 = 15, 35$, and 70 Mpc (dotted, solid, and dashed, respectively), on the scaled $\Gamma(r)$. As calculated in Chapter 4, a smaller mean free path generally produces a lower $\langle \Gamma \rangle$. The fluctuations are more pronounced as well, but the overall behavior remains the same.

5.1.2   From the Ionizing Background to τ_{eff}

Observations do not directly measure Γ but the transmission in quasar spectra. We now transform our results to the equivalent He II Lyα optical depth. To investigate the expected spatial fluctuations, we average the observed transmission F over large segments, parameterizing it in terms of the effective optical depth τ_{eff},

$$\tau_{\text{eff}} = -\ln \bar{F}. \tag{5.2}$$

Here $\bar{F}$ denotes the average transmission over a single contiguous segment.

Next, we need to relate Γ to the local forest transmission. In the simplest case of a uniform IGM, the relation would be trivial: in ionization equilibrium, the He II fraction obeys $x_{\text{HeII}} \propto \Gamma^{-1}$, so $\tau \propto \Gamma^{-1}$ as well. However, in the real IGM, a forest of discrete clouds provides most of the absorption. The Lyα forest, and therefore the optical depth, trace the local overdensity Δ of the IGM. Similar to Chapter 2, we assume ionization equilibrium

$$\Gamma n_{\text{HeII}} = n_{\text{He}} n_e \alpha, \tag{5.3}$$

where n_{HeII} is the number density of He II, n_{He} is the number density of all helium,

n_e is the number density of electrons, and α is the recombination coefficient. Since $n_e \propto n_{\mathrm{He}}$ in a highly ionized IGM, equation (5.3) implies that $n_{\mathrm{HeII}} \propto n_{\mathrm{He}}^2 \propto \Delta^2$. The optical depth is proportional to n_{HeII} (see eq. 2.2), which introduces a Δ^2 factor.

As also outlined in Chapter 2, this fluctuating Gunn-Peterson approximation requires a normalization factor to match observations. To estimate τ_{eff} (sidestepping this normalization), we use a proportionality:

$$\tau_{\mathrm{eff}} \quad \propto \quad \frac{\Delta^2}{\Gamma}. \tag{5.4}$$

Then, we fix the mean effective optical depth $\langle \tau_{\mathrm{eff}} \rangle$ separately. Note that we assume a constant IGM temperature T, which is a reasonable approximation at the end of reionization (Furlanetto & Oh 2009). Furthermore, any temperature fluctuations are expected to be subdominant to Δ and Γ fluctuations (Furlanetto & Dixon 2010).

To assign a (nonphysical) normalization, we enforce a $\langle \tau_{\mathrm{eff}} \rangle$ by averaging the transmission over *all* lines of sight. Unless otherwise noted, $\langle \tau_{\mathrm{eff}} \rangle = 2$, but we tailor this value to compare to observations. Each "measurement" is the average transmission over large, continuous distances (typically ~ 30–100 Mpc) achieved by averaging over all the pixels within each such region. Generally, we choose $\Delta r = 40$ Mpc segments to reflect the binning methods of the Worseck et al. (2011) observations, although we explore the impact of varying this length.

Figure 5.2 shows the resultant distributions for τ_{eff}, where the right panel shows the cumulative distribution functions. In this post-reionization limit, the distributions (in the bottom left panel) contain substantial variations, with a full width at half maximum (FWHM) comparable to the mean value. In agreement

with Fardal et al. (1998) and Furlanetto & Dixon (2010), we find that the scaled distributions are relatively insensitive to $\langle\tau_{\mathrm{eff}}\rangle$, which is not shown. The variance we find in $p(\tau_{\mathrm{eff}})$ is also comparable to the earlier studies, though underlying model differences have some effect. Generally, our distributions are wider, likely due our inclusion of local density variations and a frequency-dependent mean free path. As is clear from the cumulative distribution, regions with $\tau_{\mathrm{eff}}/\langle\tau_{\mathrm{eff}}\rangle \gtrsim 2$ are uncommon, and $\tau_{\mathrm{eff}}/\langle\tau_{\mathrm{eff}}\rangle \gtrsim 3$ is vanishingly unlikely.
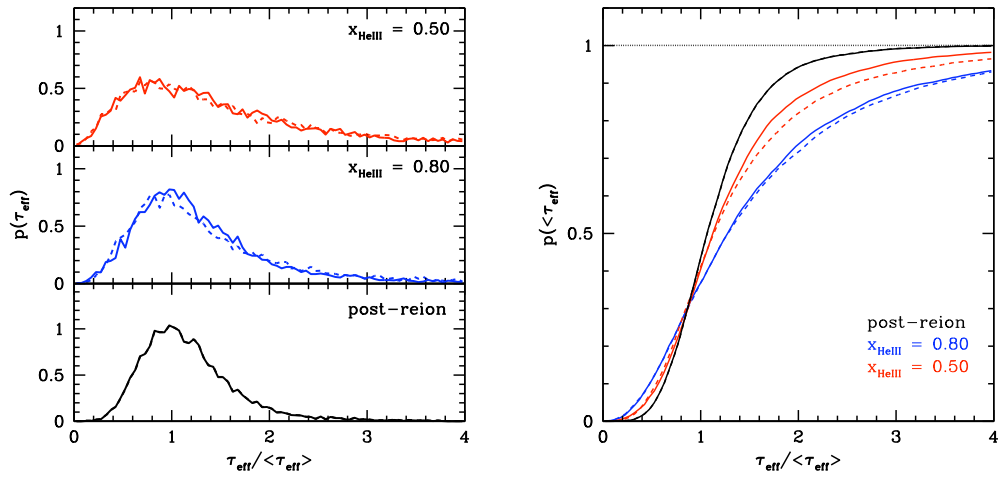

Figure 5.2 The probability and cumulative distribution of the He II optical depth relative to the fixed $\langle\tau_{\mathrm{eff}}\rangle = 2$ for post-reionization and $x_{\mathrm{HeIII}} = 0.80$ and 0.50. The solid (dashed) lines are the fiducial (abundant-source) ionizing models. The transmission is averaged over 40 Mpc segments. *Left panel:* The probability distribution of τ_{eff} for post-reionization (lower) and $x_{\mathrm{HeIII}} = 0.80$ (middle) and 0.50 (upper). *Right panel:* The cumulative probability distribution of τ_{eff}. From the highest to lowest curves at $\tau_{\mathrm{eff}} = \langle\tau_{\mathrm{eff}}\rangle$ for post-reionization and $x_{\mathrm{HeIII}} = 0.80$ and 0.50.

As a note, for higher choices of $\langle\tau_{\mathrm{eff}}\rangle$, the peak of $p(\tau_{\mathrm{eff}})$ is shifted to higher τ_{eff} and the high-end tail increases. A higher mean opacity means more long IGM segments can lie entirely at low Γ, shifting the distribution rightward. This behavior generically implies that since higher $\langle\tau_{\mathrm{eff}}\rangle$ is expected at higher redshift (in part due to the evolution of absorbers), higher measured opacities are
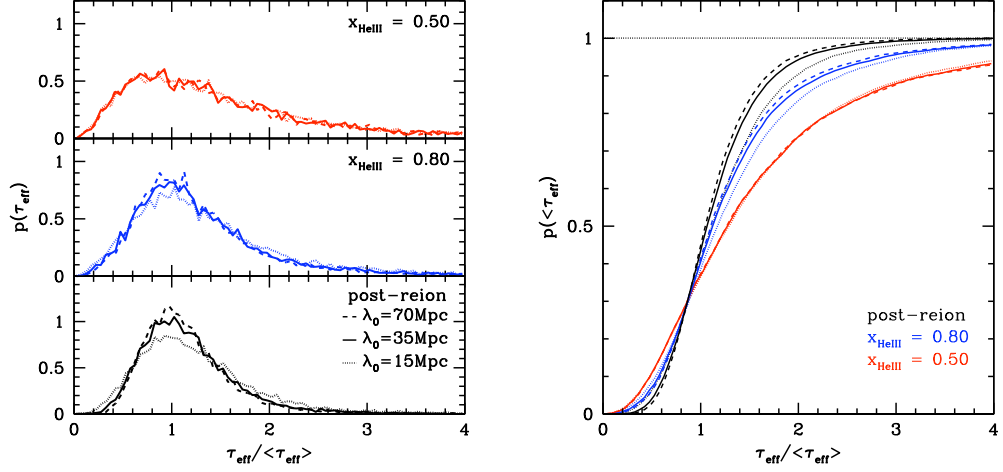
increasingly likely.

Figure 5.3 The probability (left) and cumulative (right) distributions of the scaled He II optical depth comparing λ_{mfp}. The post-reionization (black) and $x_{\mathrm{HeIII}} = 0.80$ (blue) and 0.50 (red) results are shown, with $\lambda_0 = 15, 35$, and 70 Mpc (dotted, solid, and dashed, respectively). Here, $\langle\tau_{\mathrm{eff}}\rangle = 2$ and the transmission is averaged over 40 Mpc segments.

Another choice that affects these distributions is mean free path of ionizing photons. Figure 5.3 shows the scaled optical depth probability distributions for $\lambda_0 = 15, 35$, and 70 Mpc (dotted, solid, and dashed, respectively). A lower λ_0 widens the curves and vice versa. Intuitively, a longer mean free path means a higher and more uniform ionizing background, which therefore decreases the overall fluctuations. The effect is minimal with only the smallest λ_0 exhibiting an appreciable difference.

We find the parameter that has the most impact is the length of the segment. Figure 5.4 shows the distributions of τ_{eff} (scaled to $\langle\tau_{\mathrm{eff}}\rangle$) for $\Delta r = 20, 40$, and 100 Mpc, as the dotted, solid, and dashed curves, respectively. (Note that the $x_{\mathrm{HeIII}} = 0.80$ solid curve obscures the $\Delta r = 20$ Mpc result.) Since longer segments average over more fluctuations, the distribution narrows significantly.
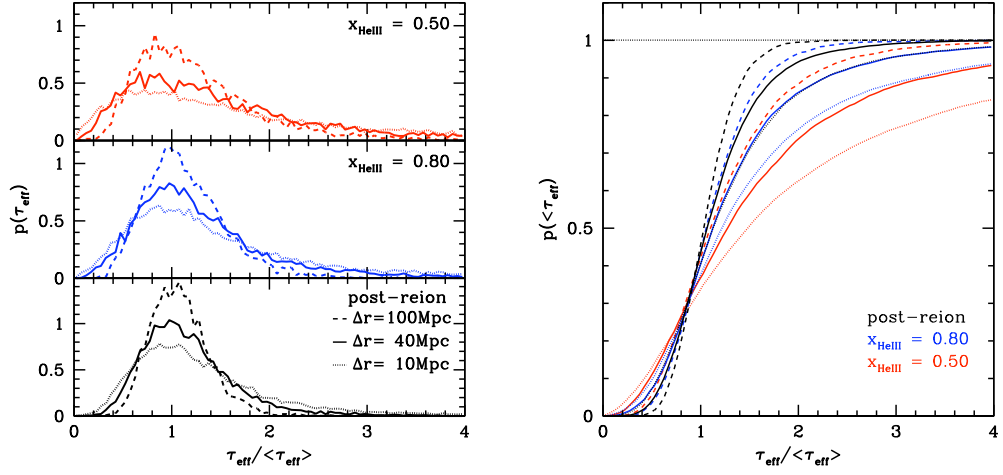
Figure 5.4 The probability (left) and cumulative (right) distributions of the scaled He II optical depth comparing λ_{mfp}. The post-reionization (black) and $x_{\mathrm{HeIII}} = 0.80$ (blue) and 0.50 (red) results are shown, with $\Delta r = 20, 40,$ and 100 Mpc (dotted, solid, and dashed, respectively). Here, $\langle \tau_{\mathrm{eff}} \rangle = 2$ and $\lambda_0 = 35$ Mpc.

When interpreting observations of the He II opacity, these effects are important to keep in mind. When presented with data averaged over a small redshift range, say $dz = 0.05$ a $z = 3$, the measured optical depth gives little insight to average opacity that is indicative of the state of the IGM. Furthermore, as is clear from Figure 5.4, $\tau_{\mathrm{eff}} / \langle \tau_{\mathrm{eff}} \rangle \gtrsim 2$ would be a fairly common occurrence even in the post-reionization regime at such small scales. In short, interpreting He II Lyα forest measurements is no easy task, and strong conclusions require careful analysis that includes the fluctuations presented here and the references throughout this work.

5.2   During the Epoch of Reionization

Up to this point, we have assumed that helium is highly ionized everywhere, so that the only opacity source for high-energy photons is λ_{mfp}. During reion-

ization, however, large swathes of the IGM contain primarily He II, increasing the expected fluctuation amplitude. As outlined in the previous chapter, we include a frequency-varying λ_{mfp} that accounts for the intervening column density of He II between the point of interest and the contributing quasar via ν_{min}. This model also allows hard photons to penetrate the singly ionized regions, providing a low-level background radiation.

Next, we approximate the evolution of fluctuations in Γ and τ_{eff} during reionization (by varying x_{HeIII}). We now need the ionization maps and active quasar distributions from Chapter 3, and we compare the fiducial and abundant-source models. What is important is that we evaluate the opacity in a local manner, including not only the Δ and Γ at the point of interest, but the ionization state as well.

5.2.1   Evolution of the Photoionization Rate Fluctuations

First, we look at the He II photoionization rate along our skewers. The upper panels of Figure 5.1 show Γ (scaled to the mean post-reionization value) for $x_{\mathrm{HeIII}} = 0.80$ and 0.50. For illustrative purposes, we used the abundant-source method to generate these curves. For this method, all dark matter halos above the minimum threshold contribute to the ionization map, which means the *active* quasars remain in the same halos for all x_{HeIII}. Although not our preferred model, the impact of He II regions is more apparent.

The left panel of Figure 5.1 displays the evolution of the same three skewers throughout reionization, where $x_{\mathrm{HeIII}} = 0.80$ and 0.50 in the middle and upper panels, respectively. Several important trends emerge. Specifically, the "floor" Γ in the post-reionization regime is no longer present. Segments of zero transmission that are tens of Mpc long emerge even at $x_{\mathrm{HeIII}} = 0.80$. The brightest

features remain, but these zones begin to end sharply. The inhomogeneous IGM induces small-scale variations along the line of sight and even dampens some of the brightest features significantly, which is important since quasars tend to reside in overdense regions. These effects will all enhance the fluctuations in τ_{eff}.

5.2.2 Effective Optical Depth Distributions

Next, we turn to the fluctuations expected in the He II Lyα forest. The left panel in Figure 5.2 shows the scaled τ_{eff} distributions for $x_{\mathrm{HeIII}} = 0.80$ and 0.50 in the middle and top panels, respectively. The fiducial (abundant-source) ionization model is the solid (dashed) curve. Note that in the post-reionization limit, the two models converge as all dark matter halos above the minimum mass threshold may host an "active" quasar. With significant amounts of He II, a long tail toward high opacity develops; the cumulative distribution in the right panel shows that $\sim 2\%$ and 8% of the 40 Mpc skewers are completely dark for $x_{\mathrm{HeIII}} = 0.80$ and 0.50, respectively. These percentages are actually lower than the Furlanetto & Dixon (2010) results. This decrease in completely "dark" segments is likely due to some combination of the the high-energy photons (from the frequency-dependent λ_{mfp}) that travel further and the inclusion of local density variations. This conclusion is slight complicated by the differing segment length and mean free path normalization. Additionally, we find that the ionizing-source model matters very little, as seen in the similarity between dashed and solid lines.

The scaled τ_{eff} probability (left) and cumulative (right) distributions shown in Figure 5.3 show the effect of varying the mean free path of photons for $x_{\mathrm{HeIII}} = 0.80$ (blue) and 0.50 (red). The dotted, solid, and dashed curves represent $\lambda_0 = 15, 35$, and 70 Mpc , respectively. As in the post-reionization regime, a smaller λ_{mfp} widens the distribution. The effect, however, diminishes at lower x_{HeIII}.

With enough singly ionized material, the precise λ_0 becomes irrelevant, since the size of ionized bubbles – not the mean free path of photons – determines the opacity, and the difference in negligible by $x_{\text{HeIII}} = 0.50$.

In contrast, varying the segment length $\Delta r = 10, 40$ and 100 Mpc (dotted, solid, and dashed, respectively), as in Figure 5.4, dramatically changes the scaled probability (left) and cumulative (right) distributions. Also, unlike in the previous figure, decreasing x_{HeIII} increases the effect of changing the segment length. In addition to the Δ and Γ variations present post-reionization, including ionized bubble morphology adds another source of fluctuations that matter on tens of Mpc scales, affecting the average transmission.

Figure 5.5 directly demonstrates the decrease in τ_{eff} fluctuations as reionization ends. The solid line is the median τ_{eff}. The dashed and dotted curves show the range of τ_{eff} that encompasses 68% and 95%, respectively, of possible values. Note that $\langle \tau_{\text{eff}} \rangle = 2$. In particular, the asymmetric nature of the τ_{eff} distributions is apparent in this context. High opacity measurements are much more likely than lower values, which is increasingly true for higher x_{HeII}. Overall, as compared to the mean, higher *and* lower measurements are more likely earlier in reionization, making fluctuations more dramatic. In the post-reionization regime, the floor in Γ prevents such strong variations.

5.3   Comparison to Data

Although (to date) only ~ 10 lines of sight have detailed He II Lyα forest spectra, the data still contain substantial fluctuations to which we can compare our model. The left panel of Figure 5.6 shows the (averaged) τ_{eff} measurements at $z < 3.2$ from the literature as outlined in Chapter 2 along with the more recent data
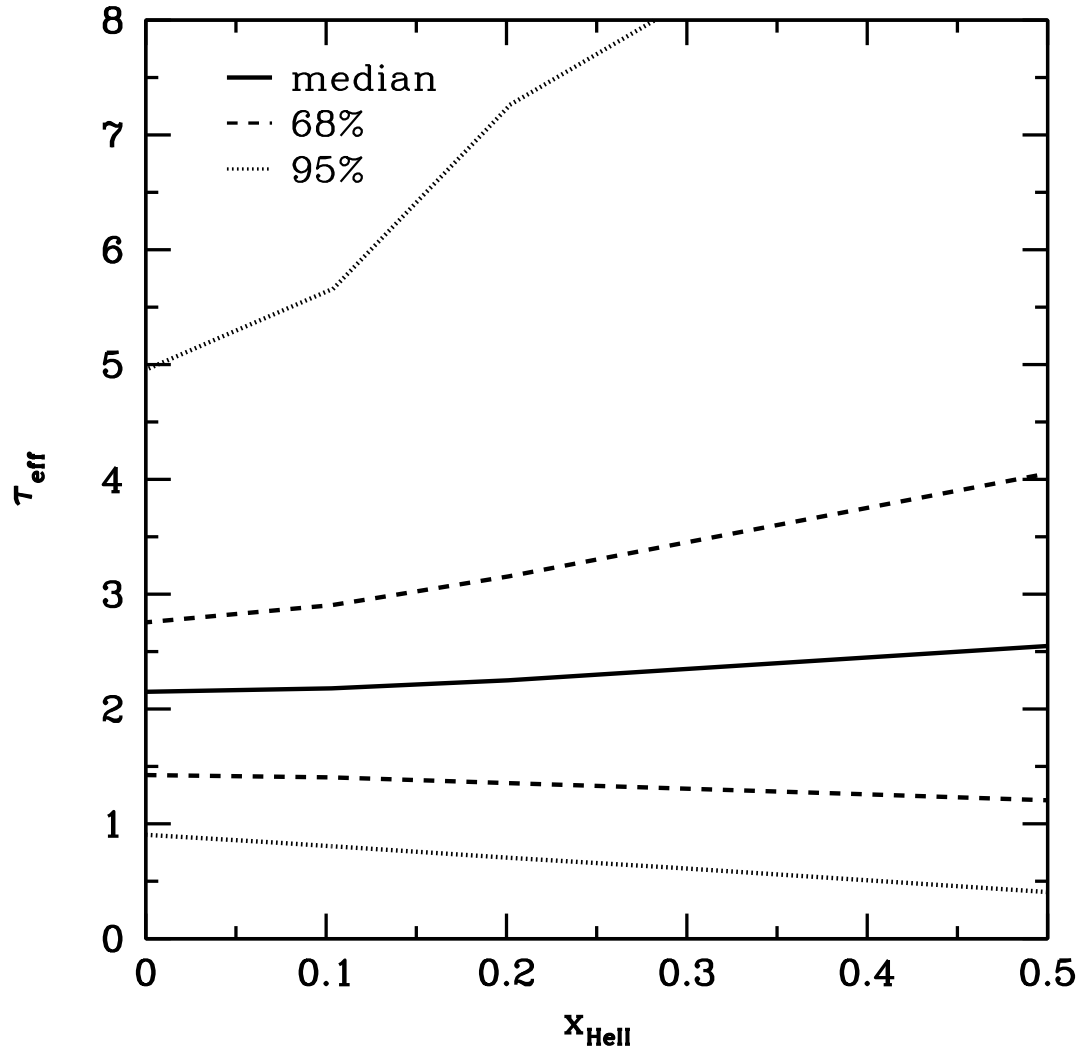
Figure 5.5 Optical depth as a function of ionized fraction. The solid line is the median τ_{eff}. The dashed and dotted curves show the range of τ_{eff} that encompasses 68% and 95%, respectively, of possible values. Here $\langle \tau_{\mathrm{eff}} \rangle = 2$. The opacity fluctuations increase as x_{HeIII} decreases, where large τ_{eff} are more probable than very low values.

compiled by Worseck et al. (2011). The solid pentagons are the averaged (binned over $\Delta z = 0.12$) data found in Worseck et al. (2011), which includes the reanalysis of HST/STIS spectra of Q0302-003 (Heap et al. 2000) and HS 1157+3143 (Reimers et al. 2005), the HST/COS data for HE 2347-4342 (Shull et al. 2010), and analysis of two new COS sightlines SDSS J0942+4852 and SDSSJ1101+1053 (Worseck & Prochaska 2011).

The solid line is the prediction for the evolution of τ_{eff} assuming that helium reionization occurred at $z > 3.2$ from Chapter 2. Note that the inputs are the Hopkins et al. (2007) QLF and $\lambda_{\mathrm{mfp}} = 30(1 + z)^{-3}$ Mpc at $z = 3$. Recent studies have cast doubt on the shallow evolution of τ_{eff} even in the post-reionization regime (Davies & Furlanetto 2012; Khaire & Srianand 2012). Although a steeper evolution changes the precise conclusions below, the general conclusions will remain due to the strong fluctuations present in the data.

The right panel of Figure 5.6 is Figure 3 from Worseck et al. (2011), showing the He II effective optical depth as a function of redshift in redshift bins of $\Delta z = 0.04$ (≈ 10 proper Mpc at $z \sim 3$). The solid and dotted lines are based on a semi-analytic model similar to that of Chapter 2, and the red and green lines are based on two McQuinn et al. (2009) simulations. Importantly, from $z = 2.36 - 2.6$, the Worseck et al. (2011) points only include HE 2347-4342, which exhibit a higher opacity than the previous measurements shown in the left panel. Generically, the newer data and analysis give higher opacities for the same lines of sight, which has a nontrivial impact on the conclusions of any study based on older data as in Chapter 2 and Furlanetto & Dixon (2010). Therefore, the reference curve in the left panel in not ideal for higher redshift, so we also use the $\eta = 80$ solid line in the right panel or comparisons. For anything below $z = 2.36$, we must rely on the older data.
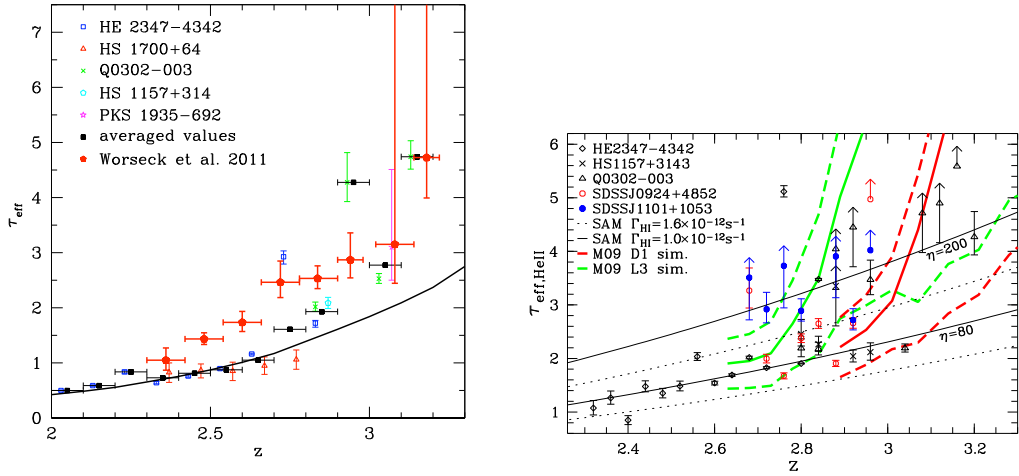
Figure 5.6 *Left panel:* Evolution of the He II effective optical depth, including averaged Worseck et al. (2011) data. See Chapter 2 for the older data, explanation of averaged values, and the fiducial model that produced the solid curve. *Right panel:* He II effective optical depth as a function of redshift in redshift bins of $\Delta z = 0.04$ (≈ 10 proper Mpc at $z \sim 3$), Figure 3 from Worseck et al. (2011). The solid and dotted lines are based on a semi-analytic model similar to that of Chapter 2, and the red and green lines are based on two McQuinn et al. (2009) simulations.

Deviations from our (or nearly any) smooth model occur in several regimes, which we examine below. First, at $z \lesssim 2.25$, the data from HE 2347-4342 imply that Γ is ~ 2 times smaller than our simple extrapolation from higher redshifts as found in Chapter 2. Second, at $z \sim 2.7$–2.9, all lines of sight exhibit substantial fluctuations between large and small transmissions on the binning scale of the right panel, or ~ 10 Mpc (proper). Finally, at $z > 3$, the $\tau_{\rm eff}$ are mainly lower limits that are difficult to accommodate in any smooth model, but there are two exceptions where significant transmission is still present, implying very large variations. Our primary goal is to determine whether the data can be explained by including cosmic variance around the smoothly evolving models. No matter the exact optical depth evolution sufficiently strong variations most likely He II reionization.

5.3.1 Fluctuations at $z \lesssim 2.7$

We first wish to assess the significance of deviations from the "smooth" Γ evolution models at low redshift. Here, we only consider HE 2347-4342, since it is the only line of sight available for $z < 2.3$, where we use Zheng et al. (2004b) data. For this regime, we use the model from Chapter 2 for our average opacity reference values, since it is based on the older generation data. Above this redshift, we compare the Worseck et al. (2011) results to the $\eta = 80$ model presented therein.

We list the measured optical depths from HE 2347-4342 and the predictions from the models describe above in Table 5.1. The first three columns in the table give the central redshift of the skewers, the observed mean transmission (and 1σ statistical errors), and the predicted effective optical depth, from left to right.

Before evaluating the likelihood of these measurements, we do note two po-

tential systematic problems with the data, which are not included in the error estimates. One, this low-z regime corresponds to small wavelengths, so the continuum correction is most uncertain here. Two, the $z < 2.3$ regime has been corrected for Lyβ and higher-order line contamination using the corresponding Lyα forest, but that correction may not be perfect given the noisy He II data. And given that this region relies solely on older data, any conclusions are extremely tentative.

We report the probability of τ_{eff} greater than or equal to the observed values in the fourth column of Table 5.1 using the cumulative distribution functions of §5.1.2. Note that since these measurements are averaged over $134 - 146$ Mpc, we use the $\Delta r = 100$ Mpc results. None of these measurements are surprising, even given our (probably) low $\langle \tau_{\mathrm{eff}} \rangle$ estimate. Although the point at $z = 2.25$ is somewhat unlikely, only one line of sight has data at this low redshift. This result differs from Furlanetto & Dixon (2010), where this same point was considered only 3% likely. Since the Γ fluctuations are fairly similar between the two methods in the post-reionization regime, this difference is likely due to the more realistic density treatment and the frequency-dependent λ_{mfp}.

Next, we examine the rest of the HE 2347-4342 data, where the fifth and sixth columns of Table 5.1 show the likelihood of measuring a τ_{eff} greater than or equal to the observed for $x_{\mathrm{HeIII}} = 0.8$ and 0.5, respectively. Note that we are using the Worseck et al. (2011) data and the $\eta = 80$ opacity predictions for all subsequent calculations, and, therefore, we also assume $\Delta r = 40$ Mpc. A value at or lower than $\tau_{\mathrm{eff}} = 0.85$ at $z = 2.40$ is fairly unlikely at $\sim 15\%$. Comparing the observed optical depth at $z = 2.25$ and $z = 2.40$ emphasizes the large variations along this one line of sight. The most striking point is at $z = 2.76$, where it is vanishingly unlikely to measure $\tau_{\mathrm{eff}} > 5.12$ in the post-reionization epoch.

Table 5.1. Probability Estimates for HE 2347-4342

$\langle z \rangle$	τ_{eff} (obs)	$\langle \tau_{\text{eff}} \rangle$ (model)	$P(x_{\text{HeIII}} = 1.0)$	$P(x_{\text{HeIII}} = 0.8)$	$P(x_{\text{HeIII}} = 0.5)$
2.05	$0.499^{+0.011}_{-0.012}$[a]	0.46[b]	36%	_[c]	_[c]
2.15	$0.589^{+0.013}_{-0.013}$[a]	0.52[b]	30%	_[c]	_[c]
2.25	$0.837^{+0.031}_{-0.034}$[a]	0.61[b]	14%	_[c]	_[c]
2.40	$0.85^{+0.09}_{-0.08}$[d]	1.3[e]	85%	81%	76%
2.56	$2.04^{+0.07}_{-0.07}$[d]	1.5[e]	24%	35%	42%
2.76	$5.12^{+0.11}_{-0.10}$[d]	1.8[e]	< 1%	5%	12%

[a]From HE 2347-4342 (Zheng et al. 2004b) with $\Delta r \sim 100$ Mpc

[b]Model of Chapter 2

[c]We assume that helium reionization is complete by $z = 2.3$ and so do not report these values.

[d]From HE 2347-4342 (Worseck et al. 2011) with $\Delta r \sim 40$ Mpc

[e]$\eta = 80$ model from Worseck et al. (2011)

Decreasing x_{HeIII} improves this situation somewhat, but such low transmission is generally uncommon.

5.3.2   Fluctuations at $z \gtrsim 2.7$

As seen at lower redshift, τ_{eff} varies along a line of sight, but these fluctuations are amplified around $z \sim 2.7$. Furthermore, the difference between lines of sight increases. We look in detail at one of the new sightlines SDSS J0924+4852 (Worseck et al. 2011). Table 5.2 displays the redshift, the observed optical depth at that redshift, the reference $\langle \tau_{\text{eff}} \rangle$, and the probability of measuring the observed value or higher for $x_{\text{HeIII}} = 1.0$, 0.8, and 0.5, from left to right. As the second column demonstrates, the observed opacities vary significantly. This region also includes several points that are $< 10\%$ likely post-reionization. These fluctuations and a trend toward higher τ_{eff} are indicative of helium reionization. Looking at the fifth column, an 80% ionized universe can easily accommodate the optical

Table 5.2.   Probability Estimates for SDSS J0924+4852

$\langle z \rangle$	$\tau_{\rm eff}$ (obs)[a]	$\langle \tau_{\rm eff} \rangle$ (model)[b]	$P(x_{\rm HeIII} = 1.0)$	$P(x_{\rm HeIII} = 0.8)$	$P(x_{\rm HeIII} = 0.5)$
2.68	$3.27^{+0.42}_{-0.33}$	1.7	6%	14%	25%
2.76	$1.68^{+0.06}_{-0.06}$	1.8	60%	62%	65%
2.84	$2.65^{+0.09}_{-0.09}$	2.0	28%	37%	48%
2.92	$2.66^{+0.10}_{-0.10}$	2.1	4%	42%	52%
2.96	$4.97^{+\infty}_{-0.00}$	2.2[c]	4%	12%	24%

[a]From SDSS J0924+4852 (Worseck et al. 2011) with $\Delta r \sim 40$ Mpc

[b]$\eta = 80$ model from Worseck et al. (2011)

[c]This measurement is a lower limit

depth range present in this line of sight.

One possibility that can explain the high opacities as compared to our model is that $\langle \tau_{\rm eff} \rangle$ evolves more steeply at high redshifts, so that the mean value is actually closer to the measured value. Figure 5.6 shows that the measured average $\tau_{\rm eff}$ is also somewhat higher than our model (though this difference is less true for the simple Worseck et al. (2011) model that is calibrated to the more recent data). An underestimate in the mean from our model would provide a plausible scenario. Although there are plausible reasons for a steeper evolution (see Davies & Furlanetto 2012; Khaire & Srianand 2012), the large variations about any mean would be difficult to explain.

One indication that we are observing regions of the Universe with different ionization states is the contrast between SDSSJ1101+1053 and HS1157+3143 seen in the right panel of Figure 5.6. The former line of sight consistently exhibits $\tau_{\rm eff} \approx 3$ and higher from $z = 2.7 - 3.0$. The latter line of sight hovers around $\tau_{\rm eff} \approx 2$ or below for most of the range $z = 2.8 - 3.0$ with one uncertain exception at $z = 2.88$. This fact and the general trend toward higher opacities $z > 2.8$

indicate that we are likely observing the end of helium reionization.

5.4 Discussion

We have computed the fluctuations expected in measurements of the average transmission of the He II Lyα forest due to large-scale variations in the radiation field and an inhomogeneous IGM. We employed an empirical, active quasar distribution to simulate the radiation field and relied on the ionization maps and density fields resultant from the methods in Chapter 3. We then measured the transmission averaged over long segments along random lines of sight and computed the probability distribution for $\tau_{\rm eff}$. For a fully ionized universe, the radiation field typically produces a FWHM for the $\tau_{\rm eff}$ distribution of order its mean value (Fardal et al. 1998; Furlanetto & Dixon 2010).

During reionization, long stretches (with sizes $\gtrsim 100$ Mpc) of low transmission appear in the empty voids between quasars. These troughs remain even late in reionization. The $\tau_{\rm eff}$ distributions are broadened in this regime by producing a large tail toward very high optical depths (and, to compensate, shifting the median transmission to smaller values).

We have shown how Γ, density variations, and ionization state induce fluctuations in the transmission. However, the He II Lyα forest is also sensitive to the IGM temperature field (which affects the recombination rate and, hence, the He II fraction within each absorber). Temperature fluctuations are substantial at the end of He II reionization (Gleser et al. 2005; Furlanetto & Oh 2008b; McQuinn et al. 2009), and they will also affect the forest. However, we expect their effects to be significantly smaller even than those due to density fluctuations. We have $x_{\rm HeII} \propto \Delta^2 \alpha(T)/\Gamma \propto \Delta^2 T^{-0.7}/\Gamma$. The variance in T is significantly less than

an order of magnitude (and hence, smaller than or comparable to that in Δ and Γ), even at the height of He II reionization, and is further damped by the smaller exponent.

Additionally, our methods ignore the fluctuations sourced by the intricacies of radiative transfer through the IGM (for example, shadowing and spectral filtering by dense regions), as well as fluctuations in the absorber population not captured by our density field. Radiative transfer effects are best described with more sophisticated numerical simulations (e.g., Maselli & Ferrara 2005; Tittley & Meiksin 2007; Paschos et al. 2007, M09, Meiksin & Tittley 2012). Since radiative transfer induces large variations on small scales and we average over large segments, we do not expect these effects to change our conclusions. By not properly accounting for absorbers, we ignore spatial variation in the mean free path, which *may* be important in the post-reionization limit. In practice, the radiation field is low far from the active quasars, leading to higher absorption in the He II Lyα forest. In turn, this absorption leads to an even smaller radiation field, creating an iterative process.

Note that we have little to say about the evolution of the average opacity. Using a 1D cosmological radiative transfer model, Davies & Furlanetto 2012 find that both Γ and λ_{mfp} evolve significantly over $z \sim 2-3$, implying a rapid evolution in τ_{eff}. Khaire & Srianand 2012 show that H I-ionizing photons escaping high-z galaxies can cause a similarly rapid evolution in Γ under the right circumstances. The exact evolution is quite uncertain in these studies, and we do not endeavor include the complex effects that produce this trend. We merely wish to address the size of fluctuations, which is dominated the varying Γ and Δ fields,

Generically, we have improved upon the methods of Furlanetto & Dixon (2010) in several ways. (1) Our mean free path prescription includes frequency

dependence, allowing hard photons to travel further. (2) Since our active quasar model relies on a realistic dark matter halo distribution, we include the effects of clustering. (3) We also use a density field that not only induces fluctuations due the inhomogeneity, but improves our calculation of the optical depth. (4) Our ionization fields are also an improvement on the simple dark pixel approached outlined at the beginning of this chapter.

Worseck et al. (2011) employ the more realistic He II simulations of McQuinn et al. (2009). These results are shown in Figure 5.6 as the red and green curves, where the timing of the end of reionization is varied. Neither of their models exactly mimics the data, but their fit is reasonable, meaning the observations are consistent with the end of helium reionization. There are advantages to our approach, in addition to the relative speed of our approach. One, we can vary many parameters without rerunning a computationally intensive simulation, giving the opportunity to determine exactly which assumptions, say the mean free path, will most affect the results. Two, we are not tied to a specific ionization history, i.e. $x_{\mathrm{HeIII}}(z)$, so we can gauge the likelihood of a measurement just based the average observed trend.

In coming years, the quality and amount of data will improve greatly. Syphers et al. (2012) present 13 new sightlines that are promising candidates for detailed study with COS (see also Syphers et al. 2009; Syphers et al. 2009). The promising prospects include bright quasars and minimal intervening absorption, which is essential for He II Lyα forest studies. Furthermore, these quasars probe exactly the interesting era of $z = 3 - 4$, the heart of reionization.

CHAPTER 6

Summary and Conclusions

6.1 Summary of Dissertation

This dissertation comprehensively addressed the epoch of He II reionization, which has important consequences for the intergalactic medium, can provide clues to the ionizing source properties, and may serve as an analog to hydrogen reionization. The main goals of this work were to develop approximate models that not only make generally predictions about the morphology and progress of inhomogeneous helium reionization but also provide tools for interpreting observations of this era. These studies are especially timely given the recent and ongoing progress made in the understanding of the $z \sim 3$ Universe. In particular, the substantial increase in available lines of sight suitable for He II Lyα forest analysis from the Cosmic Origins Spectrograph provide a great probe of the (likely) end of helium reionization (Shull et al. 2010; Worseck et al. 2011; Syphers et al. 2012).

In Chapter 2, we presented a semi-analytic model for the He II optical depth that included for the first time *both* a fluctuating UV background and an inhomogeneous density field. Based on the sparse data available at that time, we found that the observations implied a sharp downturn in the He II photoionization rate (or, similarly, the attenuation length of He-ionizing photons). We interpreted this perceived discontinuity as a signal of the end of the helium reionization era. By including the increased radiation background fluctuations expected during

reionization (Furlanetto 2009a), we constructed a simple model that was most consistent with reionization completing $z \approx 2.7$.

We increased the sophistication in our models in Chapter 3. We presented a novel, semi-numeric approach to the epoch of helium reionization, by adapting an existing hydrogen reionization code DExM (Mesinger & Furlanetto 2007). DExM efficiently generates dark matter halos at high redshift, which we translated to $z = 3$. From this distribution, we created two-phase ionization maps based on a photon-counting method (originally developed for hydrogen reionization by Furlanetto et al. 2004). Given the uncertainties of quasar properties and their spatial distribution, we developed and implemented two ionizing-source models. Furthermore, due to the rarity and the variable intrinsic properties of quasars, these sources differ from the original hydrogen source models. We also used an empirically derived quasar luminosity function (Hopkins et al. 2007) to generate the *instantaneous* ionizing flux. Given the speed and flexibility of our model, we enjoyed several advantages. We accommodated boxes hundreds of Mpc big – only M09 and semi-analytic models include such range – allowing us to incorporate many ionizing sources and many mean free path lengths. We also maintained spatial information (quasar clustering, local density field, etc.) that is unavailable to more analytic approaches. Furthermore, we applied a wider range of quasar models than is possible with more computationally expensive methods.

In Chapter 4, we applied this method to a systematic study of the fluctuations in the He-ionizing background both during and after helium reionization. We found substantial variation in the ionizing flux even post-reionization, in agreement with earlier studies (Furlanetto 2009a). At earlier stages of reionization, a widening, bimodal distribution developed that has not been described previously. We improved on analytic models (e.g., Furlanetto 2009a) by including a

frequency-varying mean free path, a realistic source geometry and associated density field, and a range of physically motivated ionization maps. Our results are insensitive to the exact parameters of the underlying model outlined in Chapter 3, an indication of the robustness of our predictions.

We revisited the He II Lyα forest in Chapter 5. With the ionization maps, density field, and active quasar models, we are uniquely suited to study fluctuations in the measured He II optical depth. In particular, we maintain spatial information that is important for considering correlations along a line of sight. We found that even with 20% He II, large segments many tens of Mpc in length exhibited low transmission. We quantified the expected distribution in the measured He II optical depth both during and post-reionization. In the post-reionization limit, we found the FWHM of the optical depth distribution (scaled to its mean) to be order unity, which is significant but unlikely to explain the large fluctuations present in the data $z \gtrsim 2.7$. During reionization, we detailed the widening of the probability distribution and the development of a high-τ tail, making measurements of both high and low opacity (as compared to the mean) more likely. By varying our range of parameters, we found these conclusions to be insensitive to underlying assumptions about quasar properties and Lyman-limit systems (via the mean free path). To conclude, the end of reionization appears to have occurred at $z \lesssim 2.9$, though upcoming data should strengthen this conclusion.

6.2 Future Work

There are many ways to improve upon our methods with varying degrees of difficulty. As shown throughout this work, the mean free path of photons is one of the quantities to which our results are the most sensitive. Combining the radiative transfer methods of Davies & Furlanetto (2012) with the 3D spatial information

of our models would be ideal, giving a more realistic mean free path that includes spatial variations. Along these lines, we do not explicitly include Lyman-limit systems, which are only currently accounted for in the mean free path. Adding a dense absorber population would enhance the fluctuations we found. We do not track expected heating of the IGM throughout helium reionization or include any fluctuations in temperature. The majority of these further complexities would not greatly impact our conclusions, but the additional fluctuations may be important in aggregate and the temperature of the IGM impacts galaxy formation, among other processes.

As noted previously, these methods are well-suited for studying the fluctuations in the He II Lyα forest, but there are more absorption lines present in quasar spectra. First and foremost, the increase in lines of sight from the Cosmic Origins Spectrograph (e.g., Syphers et al. 2012) will greatly increase the statistical significance of the measurements. This improvement will tighten our constraints and may lead to a concrete differentiation between helium reionization models, ideally leading to a better understanding of the IGM and quasar properties. Beyond Lyα, the He II Ly-β opacity already exhibits substantial fluctuations (Syphers et al. 2011), which our models could quantify with minimal additions.

The spatial inhomogeneities of the UV radiation background should also affect the ionization balance of the metals in the IGM. As an example, there may be a break in the ratio of C IV to Si IV at $z \sim 3$ indicating helium reionization (Songaila 1998, 2005, though see Aguirre et al. 2004). The fluctuations we find in our He-ionizing background could have important consequences for these measurements.

The transverse proximity effect has also been measured in the He II Lyα forest (Jakobsen et al. 2003; Worseck & Wisotzki 2006; Worseck et al. 2007), whereby

a quasar near another line of sight enhances the ionizing background. The size and nature of the apparent influence of the Lyα spectra may give important clues about the intrinsic properties of quasars (e.g., Furlanetto & Lidz 2011). We plan to address this and other effects in ongoing and future projects.

Bibliography

Agafonova, I. I., Centurión, M., Levshakov, S. A., & Molaro, P. 2005, A&A, 441, 9

Agafonova, I. I., Levshakov, S. A., Reimers, D., Fechner, C., Tytler, D., Simcoe, R. A., & Songaila, A. 2007, A&A, 461, 893

Aguirre, A., Schaye, J., Kim, T.-S., Theuns, T., Rauch, M., & Sargent, W. L. W. 2004, ApJ, 602, 38

Anderson, S. F., Hogan, C. J., Williams, B. F., , & Carswell, R. F. 1999, AJ, 117, 56

Bajtlik, S., Duncan, R. C., & Ostriker, J. P. 1988, ApJ, 327, 570

Becker, G. D., Bolton, J. S., Haehnelt, M. G., & Sargent, W. L. W. 2011, MNRAS, 410, 1096

Bolton, J. S., & Becker, G. D. 2009, MNRAS, 398, L26

Bolton, J. S., & Haehnelt, M. G. 2007, MNRAS, 382, 325

Bolton, J. S., Haehnelt, M. G., Viel, M., & Carswell, R. F. 2006, MNRAS, 366, 1378

Bolton, J. S., Oh, S. P., & Furlanetto, S. R. 2009, MNRAS, 395, 736

Bolton, J. S., Oh, S. P., & Furlanetto, S. R. 2009, MNRAS, 396, 2405

Bolton, J. S., & Viel, M. 2011, MNRAS, 414, 241

Bond, J. R., & Myers, S. T. 1996, ApJS, 103, 1

Calura, F., Tescari, E., D'Odorico, V., Viel, M., Cristiani, S., Kim, T.-S., & Bolton, J. S. 2012, MNRAS, 422, 3019

Conroy, C., & White, M. 2012, ArXiv e-prints

Cooray, A., & Sheth, R. 2002, Physics Reports, 372, 1

Davidsen, A. F., Kriss, G. A., & Zheng, W. 1996, Nature, 380, 47

Davies, F., & Furlanetto, S. R. 2012, in prep

Dixon, K. L., & Furlanetto, S. R. 2009, ApJ, 706, 970

Fan, X., Narayanan, V. K., Strauss, M. A., White, R. L., Becker, R. H., Pentericci, L., & Rix, H.-W. 2002, AJ, 123, 1247

Fan, X., et al. 2006, AJ, 132, 117

Fardal, M. A., Giroux, M. L., & Shull, J. M. 1998, AJ, 115, 2206

Faucher-Giguère, C.-A., Lidz, A., Zaldarriaga, M., & Hernquist, L. 2009, ApJ, 703, 1416

Fechner, C., & Reimers, D. 2007, A&A, 461, 847

Fechner, C., et al. 2006, A&A, 455, 91

Furlanetto, S. R. 2009a, ApJ, 703, 702

—. 2009b, ApJ, 700, 1666

Furlanetto, S. R., & Dixon, K. L. 2010, ApJ, 714, 355

Furlanetto, S. R., Haiman, Z., & Oh, S. P. 2008, ApJ, 686, 25

Furlanetto, S. R., & Lidz, A. 2011, ApJ, 735, 117

Furlanetto, S. R., & Mesinger, A. 2009, MNRAS, 394, 1667

Furlanetto, S. R., & Oh, S. P. 2005, MNRAS, 363, 1031

Furlanetto, S. R., & Oh, S. P. 2008a, ApJ, 681, 1

—. 2008b, ApJ, 682, 14

—. 2009, ApJ, 701, 94

Furlanetto, S. R., Zaldarriaga, M., & Hernquist, L. 2004, ApJ, 613, 1

Garzilli, A., Bolton, J. S., Kim, T.-S., Leach, S., & Viel, M. 2012, MNRAS, 424, 1723

Giroux, M. L., Fardal, M. A., & Shull, J. M. 1995, ApJ, 451, 477

Gleser, L., Nusser, A., Benson, A. J., Ohno, H., & Sugiyama, N. 2005, MNRAS, 361, 1399

Gültekin, K., et al. 2009, ApJ, 698, 198

Gunn, J. E., & Peterson, B. A. 1965, ApJ, 142, 1633

Heap, S. R., Williger, G. M., Smette, A., Hubeny, I., Sahu, M. S., Jenkins, E. B., Tripp, T. M., & Winkler, J. N. 2000, ApJ, 534, 69

Hogan, C. J., Anderson, S. F., & Rugers, M. H. 1997, AJ, 113, 1495

Hopkins, P. F., Hernquist, L., Cox, T. J., Di Matteo, T., Robertson, B., & Springel, V. 2005, ApJ, 630, 716

—. 2006, ApJS, 163, 1

Hopkins, P. F., Hernquist, L., Martini, P., Cox, T. J., Robertson, B., Di Matteo, T., & Springel, V. 2005, ApJ, 625, L71

Hopkins, P. F., Richards, G. T., & Hernquist, L. 2007, ApJ, 654, 731

Hui, L., & Gnedin, N. Y. 1997, MNRAS, 292, 27

Jakobsen, P., Boksenberg, A., Deharveng, J. M., Greenfield, P., Jedrzejewski, R., & Paresce, F. 1994, Nature, 370, 35

Jakobsen, P., Jansen, R. A., Wagner, S., & Reimers, D. 2003, A&A, 397, 891

Jenkins, A., Frenk, C. S., White, S. D. M., Colberg, J. M., Cole, S., Evrard, A. E., Couchman, H. M. P., & Yoshida, N. 2001, MNRAS, 321, 372

Kelly, B. C., Vestergaard, M., Fan, X., Hopkins, P., Hernquist, L., & Siemiginowska, A. 2010, ApJ, 719, 1315

Khaire, V., & Srianand, R. 2012, ArXiv e-prints

Kim, T.-S., Cristiani, S., & D'Odorico, S. 2002, A&A, 383, 747

Kirkman, D., & Tytler, D. 2008, MNRAS, 391, 1457

Kriss, G. A., et al. 2001, Science, 293, 1112

Lidz, A., Faucher-Giguère, C.-A., Dall'Aglio, A., McQuinn, M., Fechner, C., Zaldarriaga, M., Hernquist, L., & Dutta, S. 2010, ApJ, 718, 199

Loeb, A., & Barkana, R. 2001, Annual Review of Astronomy and Astrophysics, 39, 19

Madau, P., Haardt, F., & Rees, M. J. 1999, ApJ, 514, 648

Maselli, A., & Ferrara, A. 2005, MNRAS, 364, 1429

McQuinn, M., Lidz, A., Zaldarriaga, M., Hernquist, L., Hopkins, P. F., Dutta, S., & Faucher-Giguère, C.-A. 2009, ApJ, 694, 842

Meiksin, A., & Tittley, E. R. 2012, MNRAS, 3000

Meiksin, A., & White, M. 2003, MNRAS, 342, 1205

Meiksin, A. A. 2009, Reviews of Modern Physics, 81, 1405

Mesinger, A., & Furlanetto, S. 2007, ApJ, 669, 663

—. 2009, MNRAS, 400, 1461

Miralda-Escudé, J., Haehnelt, M., & Rees, M. J. 2000, ApJ, 530, 1

Muzahid, S., Srianand, R., & Petitjean, P. 2011, MNRAS, 410, 2193

O'Meara, J. M., Prochaska, J. X., Worseck, G., Chen, H.-W., & Madau, P. 2012,
    ArXiv e-prints

Paschos, P., Norman, M. L., Bordner, J. O., & Harkness, R. 2007, ArXiv e-prints

Pawlik, A. H., Schaye, J., & van Scherpenzeel, E. 2009, MNRAS, 394, 1812

Petitjean, P., Webb, J. K., Rauch, M., Carswell, R. F., & Lanzetta, K. 1993,
    MNRAS, 262, 499

Press, W. H., & Schechter, P. 1974, ApJ, 187, 425

Prochaska, J. X., O'Meara, J. M., & Worseck, G. 2010, ApJ, 718, 392

Reimers, D., Fechner, C., Hagen, H.-J., Jakobsen, P., Tytler, D., & Kirkman, D.
    2005, A&A, 442, 63

Reimers, D., Kohler, S., Wisotzki, L., Groote, D., Rodriguez-Pascual, P., &
    Wamsteker, W. 1997, A&A, 327, 890

Ricotti, M., Gnedin, N. Y., & Shull, J. M. 2000, ApJ, 534, 41

Rudie, G. C., Steidel, C. C., & Pettini, M. 2012, ArXiv e-prints

Schaye, J., Theuns, T., Rauch, M., Efstathiou, G., & Sargent, W. L. W. 2000, MNRAS, 318, 817

Scott, J. E., Kriss, G. A., Brotherton, M., Green, R. F., Hutchings, J., Shull, J. M., & Zheng, W. 2004, ApJ, 615, 135

Sheth, R. K., & Tormen, G. 1999, MNRAS, 308, 119

Shull, J. M., France, K., Danforth, C. W., Smith, B., & Tumlinson, J. 2010, ApJ, 722, 1312

Shull, J. M., Stevans, M., & Danforth, C. W. 2012, ApJ, 752, 162

Shull, J. M., Tumlinson, J., Giroux, M. L., Kriss, G. A., & Reimers, D. 2004, ApJ, 600, 570

Smette, A., Heap, S. R., Williger, G. M., Tripp, T. M., Jenkins, E. B., & Songaila, A. 2002, ApJ, 564, 542

Sokasian, A., Abel, T., & Hernquist, L. 2002, MNRAS, 332, 601

Songaila, A. 1998, AJ, 115, 2184

—. 2005, AJ, 130, 1996

Storey, P. J., & Hummer, D. G. 1995, MNRAS, 272, 41

Storrie-Lombardi, L. J., McMahon, R. G., Irwin, M. J., & Hazard, C. 1994, ApJL, 427, L13

Syphers, D., et al. 2009, ApJ, 690, 1181

Syphers, D., Anderson, S. F., Zheng, W., Haggard, D., Meiksin, A., Schneider, D. P., & York, D. G. 2009, ApJS, 185, 20

Syphers, D., Anderson, S. F., Zheng, W., Meiksin, A., Schneider, D. P., & York, D. G. 2012, AJ, 143, 100

Syphers, D., et al. 2011, ApJ, 742, 99

Telfer, R. C., Zheng, W., Kriss, G. A., & Davidsen, A. F. 2002, ApJ, 565, 773

Tittley, E. R., & Meiksin, A. 2007, MNRAS, 380, 1369

Tytler, D., Fan, X.-M., Burles, S., Cottrell, L., Davis, C., Kirkman, D., & Zuo, L. 1995, in QSO Absorption Lines, ed. G. Meylan, 289–+

Vladilo, G., Centurión, M., D'Odorico, V., & Péroux, C. 2003, A&A, 402, 487

Weinberg, D. e. a. 1999, in Evolution of Large Scale Structure : From Recombination to Garching, ed. A. J. Banday, R. K. Sheth, & L. N. da Costa, 346–+

Worseck, G., Fechner, C., Wisotzki, L., & Dall'Aglio, A. 2007, A&A, 471, 805

Worseck, G., & Prochaska, J. X. 2011, ApJ, 728, 23

Worseck, G., et al. 2011, ApJL, 733, L24+

Worseck, G., & Wisotzki, L. 2006, A&A, 450, 495

Wyithe, J. S. B., & Loeb, A. 2002, ApJ, 581, 886

—. 2007, MNRAS, 382, 921

Zahn, O., Lidz, A., McQuinn, M., Dutta, S., Hernquist, L., Zaldarriaga, M., & Furlanetto, S. R. 2007, ApJ, 654, 12

Zahn, O., Mesinger, A., McQuinn, M., Trac, H., Cen, R., & Hernquist, L. E. 2011, MNRAS, 414, 727

Zel'Dovich, Y. B. 1970, A&A, 5, 84

Zheng, W., Chiu, K., Anderson, S. F., Schneider, D. P., Hogan, C. J., York, D. G., Burles, S., & Brinkmann, J. 2004a, AJ, 127, 656

Zheng, W., & Davidsen, A. 1995, ApJL, 440, L53

Zheng, W., et al. 2004b, ApJ, 605, 631

Zheng, W., Kriss, G. A., Telfer, R. C., Grimes, J. P., & Davidsen, A. F. 1997, ApJ, 475, 469

Zheng, W., et al. 2008, ApJ, 686, 195

Zuo, L. 1992, MNRAS, 258, 36